Numerical simulation of non-linear phenomena in geotechnical engineering

Sørensen, Emil Smed

DOI (link to publication from Publisher):
10.5278/vbn.phd.engsci.00108

Publication date:
2016

Document Version
Publisher's PDF, also known as Version of record

NUMERICAL SIMULATION OF NON-LINEAR PHENOMENA IN GEOTECHNICAL ENGINEERING

BY
EMIL SMED SØRENSEN

DISSERTATION SUBMITTED 2016

AALBORG UNIVERSITY
DENMARK

Numerical simulation of non-linear phenomena in geotechnical engineering

Ph.D. Dissertation

Emil Smed Sørensen

Dissertation submitted May 7, 2016

Dissertation submitted: May 7, 2016

PhD supervisor: Prof. Lars Damkilde
Aalborg University

Assistant PhD supervisor: Assoc. Prof. Johan Clausen
Aalborg University

PhD committee: Associate Prof. Lars Vabbersgaard Andersen (chair.)
Aalborg University

Professor Martin Achmus
Leibniz University Hannover

Technical Director Ole Hededal
COWI A/S

PhD Series: Faculty of Engineering and Science, Aalborg University

ISSN (online): 2246-1248
ISBN (online): 978-87-7112-701-0

Published by:
Aalborg University Press
Skjernvej 4A, 2nd floor
DK – 9220 Aalborg Ø
Phone: +45 99407140
aauf@forlag.aau.dk
forlag.aau.dk

Printed in Denmark by Rosendahls, 2016

Curriculum Vitae

Emil Smed Sørensen

Higher Education

2012 - 2015 **Ph.D. fellow**
Aalborg University, Aalborg, Denmark.

2010 - 2012 **MSc. in Structural and Civil Engineering**
Aalborg University, Aalborg, Denmark.

2007 - 2010 **BSc. in Structural and Civil Engineering**
Aalborg University, Aalborg, Denmark.

Teaching Experience

Master level **Advanced Soil Mechanics**
Upper & lower bound methods.

Supervision of 1st semester MSc. student groups
Analysis & design of load-bearing structures.

Geotechnical supervision of 1st semester Cand. Scient. Techn. student groups
Design and construction of buildings.

Bachelor level **Foundation & Earth Pressure**
Brinch-Hansen earth pressure theory and design of sheet pile walls.

Supervision of 2nd semester BSc. student groups
Reality of Models.

Publications

2015 **Implementation of the modified Hoek-Brown model into the finite element method**
E.S. Sørensen, J. Clausen, R.S. Merifield, L. Damkilde
28th Nordic Seminar on Computational Mechanics 22-23 October Tallinn, 2015, Proceedings of the NSCM28, Pages 163-166.

2015 **Finite element implementation of the Hoek–Brown material model with general strain softening behavior**
E.S. Sørensen, J. Clausen, L. Damkilde
International Journal of Rock Mechanics and Mining Sciences, Volume 78, Pages 163-174.

2013 **Numerical implementation of the Hoek-Brown material model with strain hardening**
E.S. Sørensen, J. Clausen, L. Damkilde
Research and Applications in Structural Engineering, Mechanics and Computation - Proceedings of the 5th International Conference on Structural Engineering, Mechanics and Computation, SEMC 2013, Pages 375-380.
Rewarded with a Young Researcher Fellowship Award at the SEMC 2013 conference.

Abstract

Numerical simulations are becoming an everyday tool for practicing geotechnical engineers. A driving factor in this development is that numerical simulations allow for a detailed treatment of the non-linear effects that often govern geotechnical problems and hence provide a realistic basis for the design of efficient and safe solutions. This thesis deals with the development and implementation of such numerical simulations using the Finite Element Method.

Part of this thesis is concerned with the numerical treatment of dynamic soil-fluid interaction, which is of importance for problems involving e.g. offshore structures where the two-phase composition of saturated soils can have significant impact on the response of the structure during dynamic loading. The governing equations of such problems are described by poroelasticity and take into account the inertia of both solid and fluid phases. However, the full incorporation of these equations is generally not available through the common commercial finite element codes, which rely on a simplified set of equations that neglect the inertia of the fluid phase. For this reason, this thesis is concerned with the development of a custom-made finite element code, which incorporates the full set of equations. The developed code is used to study the effects of fluid inertia on the dynamic tensile resistance of a suction bucket.

Further, this thesis is concerned with the development and implementation of more elaborate constitutive models for use in rock modeling based on the rock specific, non-linear Hoek-Brown strength criterion. Often it is observed that rock masses exhibit a brittle or softening behavior once the initial strength has been exceeded. In this regard, a constitutive model is developed and implemented into the finite element method, which is capable of incorporating an arbitrary strain softening behavior. Further, it is believed that the Hoek-Brown criterion, in some cases, can overestimate the tensile strength of the rock mass. Based on this, an elastic-perfectly-plastic numerical implementation of the Hoek-Brown material model is developed which incorporates a tension-cutoff. Both models rely on return mapping in principal stress space.

Resumé

Numeriske simuleringer er blevet et dagligdagsværktøj for praktiserende geoteknikere. En af hovedårsagerne til denne udvikling skyldes, at numeriske simuleringer tillader en detaljeret behandling af de ikke-lineære effekter som ofte er afgørende i geotekniske problemstillinger og derfor bidrager til et realistisk grundlag for dimensionering af effektive og sikre løsninger. Denne afhandling beskæftiger sig med udvikling og implementering af sådanne numeriske simuleringer ved brug af elementmetoden.

En del af denne afhandling omhandler den numeriske behandling af dynamisk jord-fluid interaktion, som er af betydning for problemer vedrørende f.eks. offshore konstruktioner, hvor den vandmættede jords tofase-struktur kan have betydelig indvirkning på konstruktionens virkemåde under dynamisk belastning. De styrende ligninger for sådanne problemer er beskrevet ved hjælp af poroelasticitet og tager både inerti af solid og fluid i betragtning. Imidlertid er den fulde implementering af disse ligninger generelt ikke tilgængelig gennem de gængse kommercielle elementmetodeprogrammer, som baserer sig på et simplificeret sæt af ligninger, der negligerer fluidfasens inerti. Af denne årsag, beskæftiger denne afhandling sig med udviklingen af en specialfremstillet elementmetode-kode, der inkluderer det fulde sæt af ligninger. Denne kode er blevet brugt til at studere effekten af fluidets inerti på et bøttefundaments dynamiske trækkapacitet.

Endvidere beskæftiger denne afhandling sig med udvikling og implementering af mere detaljerede konstitutive modeller til brug i klippemasser baseret på det ikke-lineære Hoek-Brown styrkekriterium udviklet specielt hertil. Ofte er det observeret, at klippemasser udviser en sprød eller afhærdende opførsel når den initiale styrke er blevet overskredet. I den forbindelse er en materialemodel blevet udviklet og implementeret i elementmetoden, der er i stand til at medtage et vilkårligt hærdeforløb. Endvidere er det sandsynligt, at Hoek-Brown-kriteriet i nogle tilfælde kan overestimere klippematerialets trækstyrke. Ud fra denne betragtning er der blevet udviklet en elastisk-perfekt-plastisk implementering af Hoek-Brown materialemodellen, der begrænser den tilladelige trækspænding. Begge modeller baserer sig på spændingsopdateringer i hovedspændingsrummet.

Contents

Thesis Details

Thesis Title:	Numerical simulation of non-linear phenomena in geotechnical engineering
Ph.D. Student:	Emil Smed Sørensen
Supervisors:	Prof. Lars Damkilde, Aalborg University Assoc. Prof. Johan Clausen, Aalborg University

Part of this thesis consists of the following papers.

[A] E. S. Sørensen, J. Clausen, L. Damkilde, "Numerical implementation of the Hoek-Brown material model with strain hardening", *Research and Applications in Structural Engineering, Mechanics and Computation - Proceedings of the 5th International Conference on Structural Engineering, Mechanics and Computation, SEMC 2013*, pp. 375–380, 2013.
Rewarded with a Young Researcher Fellowship Award at the SEMC 2013 conference.

[B] E. S. Sørensen, J. Clausen, L. Damkilde, "Finite element implementation of the Hoek–Brown material model with general strain softening behavior", *International Journal of Rock Mechanics and Mining Sciences*, vol. 78, pp. 163–174, 2015, doi:10.1016/j.ijrmms.2015.05.005.

[C] E. S. Sørensen, J. Clausen, R. S. Merifield, L. Damkilde, "Implementation of the modified Hoek-Brown model into the finite element method", *28th Nordic Seminar on Computational Mechanics 22-23 October Tallinn, 2015, Proceedings of the NSCM28*, pp. 163–166, 2015.

[D] E. S. Sørensen, J. Clausen, L. Damkilde, "Comparison of numerical formulations for the modeling of the dynamic tensile resistance of suction buckets", submitted to *Computers and Geotechnics*.

This thesis has been submitted for assessment in partial fulfillment of the PhD degree. The thesis is based on the submitted or published scientific papers, which are listed above. Parts of the papers are used directly or indirectly in the extended summary of the thesis. As part of the assessment, co-author

statements have been made available to the assessment committee and are also available at the Faculty. The thesis is not in its present form acceptable for open publication but only in limited and closed circulation as copyright may not be ensured.

Preface

The present thesis "Numerical simulation of non-linear phenomena in geotechnical engineering" has been prepared in connection with a Ph.D. study carried out at the Department of Civil Engineering, Aalborg University, Aalborg, Denmark, in the period from September 2012 to May 2016.

In this regard, I wish to thank my supervisor, Professor Lars Damkilde, for giving me the opportunity to conduct this Ph.D. study and allowing me to dig into the complex nature of numerical simulations. His experience within the field and the scientific community in general is highly appreciated.

I also wish to thank my co-supervisor, Associate Professor Johan Clausen, for his constant faith in me and for always taking the time to discuss, help out and share his immense knowledge on the finite element method with me.

Further, I would like to thank Dr. Richard S. Merifield for his co-operation on the work concerning the modified Hoek-Brown criterion.

Additionally, I would like to thank all my colleagues at the Department of Civil Engineering for countless interesting discussions concerning both related and unrelated topics.

Moreover, I wish to express my sincere gratitude to my parents for all the support they have provided throughout the entirety of my studies. It will never be forgotten.

Finally, a very special thanks to my wife Katrine and our daughter Laura for their constant moral support, patience and love.

Emil Smed Sørensen
Aalborg University, May 7, 2016

Chapter 1

Introduction

Advances within hardware and software have made computational methods a crucial tool in the progress of geotechnical engineering. The ability to carry out large-scale calculations within a reasonable time frame makes it feasible to go into greater detail than what is typically possible through the more traditional hand calculations that usually impose rather strong constraints on some of the fundamental characteristics of geotechnical problems such as geometry, stratigraphy, fluid flow, material behavior, and time scale.

Many different computational methods have emerged, but the Finite Element Method(FEM) in particular has gained a strong foothold within not only geotechnical engineering but other engineering branches and industries as well. FEM is a very general and versatile numerical framework for solving differential equations, which can be applied to the governing differential equations that arise when the classical approach of treating geotechnical materials as continua is employed.

With FEM, many of the traditional limitations can be circumvented, making it possible to model geotechnical problems of arbitrary geometry in full 3D using very elaborate material models while simultaneously taking any time effects into account. However, such analysis requires stable and robust numerical algorithms, and there are still many challenges to overcome.

1.1 Scope of thesis

This thesis deals with the development, implementation and usage of FEM within the field of geotechnical engineering, with focus on the non-linear phenomena of dynamic soil-fluid interaction as well as rock modeling as explained in the following.

Figure 1.1: Wave hitting the Oseberg A oil platform located in the North Sea during a hurricane in January 2007 (oilrig-photos.com, 2015).

1.1.1 Dynamic soil-fluid interaction

Dynamic geotechnical problems can be highly influenced by the presence of pore water within the soil skeleton. A case in point is that the impact resistance is significantly higher than the static resistance for dense saturated sands (Hansen and Gislason, 2007; Hansen, 2003). The effects of the fluid are thus beneficial in situations such as ice, wave or ship impacts on offshore structures, such as that depicted in Figure 1.1. On the contrary, loose sands can become liquefied during impact, rendering the sand incapable of transmitting any shear (Kramer, 1996; Holtz et al., 2010). Any structure founded on top of such liquefied soil is in immediate risk of sinking, see Figure 1.2a, whereas structures embedded in the soil, such as pipelines or tunnels, could rise to the surface due to buoyancy, see Figure 1.2b. Such a liquefied state is not only possible during impact, but can also be triggered by earthquakes or repeated shifts in loading, such as those experienced by e.g. offshore structures from wind, waves, current and the like.

These phenomena can be explained by the unique two-phase composition of saturated sands, which is characterized by a porous granular solid skeleton saturated with water. The granular structure is kept in place through intergranular contact forces and seldom allows for any tension. Further, the porous nature allows for the transport of fluids through the solid skeleton under any excess pressure. A process known as seepage. This flow exerts drag forces on the granular structure of the solid skeleton and thus affects the intergranular contact forces. In some cases, these forces are completely diminished and the granular structure loses all its integrity, effectively acting as a liquid. In other cases, the flow increases the contact between the grains,

(a) (b)

Figure 1.2: Effects of liquefaction. (a) Buildings fallen over due to liquefaction during the Niigata earthquake in Japan, 1964. (b) Sewer lifted due to liquefaction during the Chūetsu earthquake in Japan, 2004.

which in turn increase the shear resistance of the structure.

Another contributing factor is that when the granular structure deforms it can exhibit volume changes, which in turn affect the pores and hence effectively squeeze out or suck in water. Due to the granular structure, volume changes are especially prone during plastic straining of the skeleton, due to the relative sliding of the solid grains. Dense sands tend to dilate during shearing; however, such expansion is impeded by the ability of the fluid to fill the additional pore volume. The result is an increase in shear resistance. Conversely, loose sands tend to contract, which increase the pore pressure and reduce the intergranular contact forces, resulting in reduced shear resistance.

These dynamic properties hence require special attention in order to secure the safety of geotechnical structures, such as e.g. offshore foundations, but they also pose opportunities to optimize the design by utilizing the possible increase in impact resistance. This is e.g. the case for the suction bucket jacket shown in Figure 1.3 where each individual foundation consists of a so-called suction bucket. When the structure is exposed to an overturning moment, each suction bucket thus work in either compression or tension.

The tensile strength of the suction bucket is highly dependent on the load rate as indicated in Figure 1.4. For slow loading, the majority of the resistance stems from friction along the bucket skirts and self-weight, while faster loading causes a negative pressure difference between the inside and outside of the bucket, effectively sucking the bucket to the seabed.

The governing equations behind such dynamic coupled soil-fluid prob-

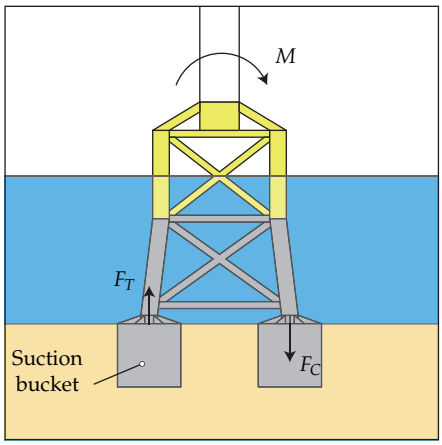

Figure 1.3: Suction bucket jacket exposed to an overturning moment, M, causing tensile, F_t, and compressive, F_c, loads on the suction buckets.

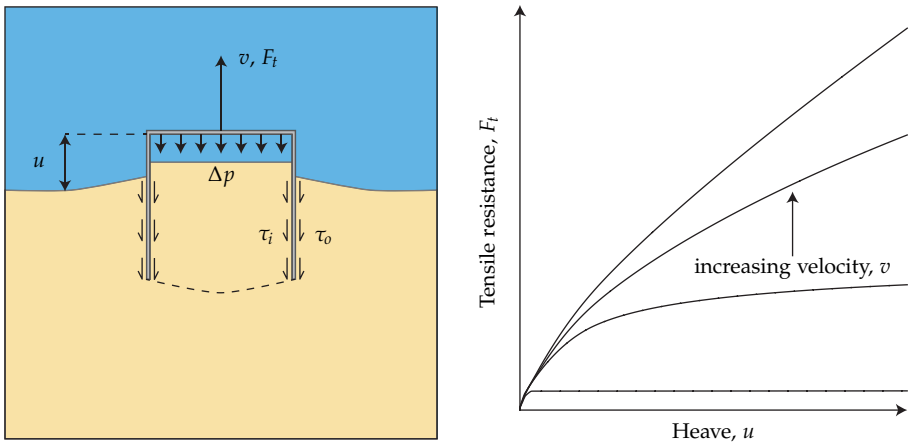

Figure 1.4: Suction bucket in tension. (a) As the bucket is pulled upwards, a negative pressure develops beneath the bucket lid, which increases the tensile resistance. (b) The tensile resistance is highly dependent upon the upwards velocity of the bucket.

lems are given by poromechanics through the very general theory of dynamic poroelasticity developed in the first half of the 20th century, also known as Biot theory after Maurice Anthony Biot, see e.g. Biot (1941, 1955); Biot and Willis (1957). In conjunction with the theory of elasto-plasticity, the rather complex Biot theory accounts for the dynamic deformation of the solid skeleton, movement of the pore fluid, and associated pore pressure and it takes inertia of both phases into consideration.

However, the full solution to the Biot equations is not available through commercial finite element codes such as Abaqus (Dassault Systèmes Simulia Corp, 2014) or Plaxis (Plaxis, 2015), which rely on a simplified set of governing equations that do not account for the inertial effects of the fluid phase. Such effects could be of importance in problems of high load rate as the one illustrated in Figure 1.4 and other high-frequency scenarios.

This thesis deals in part with the implementation and development of a code capable of solving the full Biot theory within the framework of Finite Element Modeling using elasto-plastic material models. The developed code is used to investigate the dynamic tensile strength of a suction bucket.

1.1.2 Rock modeling

Rock masses are often encountered within the fields of civil and mining engineering. One example is the excavation of a tunnel as shown in Figure 1.5. During excavation, the surrounding rock mass is affected and the tunnel wall will displace inwards to a smaller or greater extent with the possibility of a cave-in. A key task in the design of such a tunnel is thus to account for this movement and to establish whether any support structures are needed, and, if so, how big they need to be in order to counteract this movement and ensure the safety of the tunnel, see e.g. Brown et al. (1983).

Intact and jointed rock masses can be modeled in the same manner as soils using elasto-plastic continuum mechanics and extensive empirical research has led to the formulation of the Hoek-Brown strength criterion, shown in Figure 1.6a (Hoek and Brown, 1980; Hoek, 1983; Hoek et al., 2002). This criterion sets the limits of the possible stress states that can be obtained within rock masses and is very similar in nature to that of the classical Mohr-Coulomb criterion shown in Figure 1.6b. Both are isotropic pressure-dependent discontinuous criteria, but the Hoek-Brown criterion has the added complexity of being non-linear with respect to mean confining pressure.

The post-failure behavior of rock masses is dependent upon its quality, and Hoek and Brown (1997) suggest that hard rock materials exhibit a brittle behavior, see Figure 1.7a, in which the strength drops instantaneously once it fails, whereas average quality rock materials show a gradual deterioration of the strength as shown in Figure 1.7b. For poor quality rock masses, the strength remains relatively constant as shown in Figure 1.7c.

Figure 1.5: Construction of Qingdao Jiaozhou Bay tunnel in Shandong Province, China.

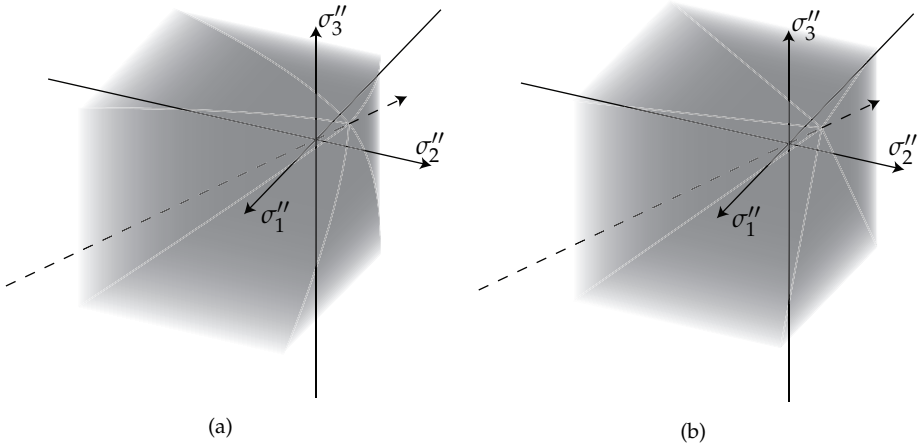

Figure 1.6: Similarity between the non-linear Hoek-Brown criterion and the linear Mohr-Coulomb criterion in principal stress space (tension positive). σ_1'', σ_2'' and σ_3'' are the effective principal stresses and the dashed line is the hydrostatic axis given by $\sigma_1'' = \sigma_2'' = \sigma_3''$. (a) The Hoek-Brown criterion. (b) The Mohr-Coulomb criterion

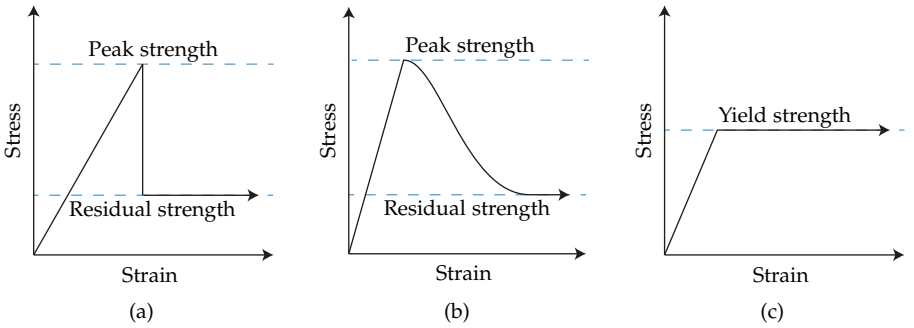

Figure 1.7: Different post-failure characteristics of rock masses. (a) Brittle. (b) Softening. (c) Perfect plasticity

Analytical and semi-analytical solutions utilizing the Hoek-Brown criterion with different post-failure behavior are available for some of the classical problems within rock engineering, such as e.g. the excavation of a circular tunnel. However, numerical simulation is needed for more complex geometry.

Currently only an elastic-perfectly-plastic version of the Hoek-Brown criterion is available (Clausen and Damkilde, 2008), and thus the expected strength and post-failure behaviors can not be properly included in the analysis. This shortcoming is usually circumvented by one of the following two methods.

One method is to utilize the elastic-perfectly-plastic version of the Hoek-Brown criterion with a parameter set which is believed to be representative of the entire rock mass domain both before and after plastic straining. One extreme of this method is the conservative method of choosing the weakened strength, resulting in a safe but most likely oversized structure. The other extreme is to choose the pre-failure strength, resulting in a possibly undersized and unsafe structure. These two choices thus set the limits for the true behavior, but its precise location can not be established.

The other method is to abandon the rock specific Hoek-Brown criterion completely in favor of the simpler Mohr-Coulomb criterion, which is available in both a modified form with a tension cut-off and a softening form (Ottosen and Ristinmaa, 2005; de Souza Neto et al., 2008). In doing so, a suitable Mohr Coulomb approximation of the Hoek-Brown criterion needs to be established for the pre- and post-failure evolution of the strength. The deficiency of this method is, that the Mohr Coulomb approximation allows for some stress states that would otherwise have been restricted by the Hoek-Brown criterion while, at the same time, restricting some stress states that would have been allowable.

Thus for both methods, only an approximate solution is found when soft-

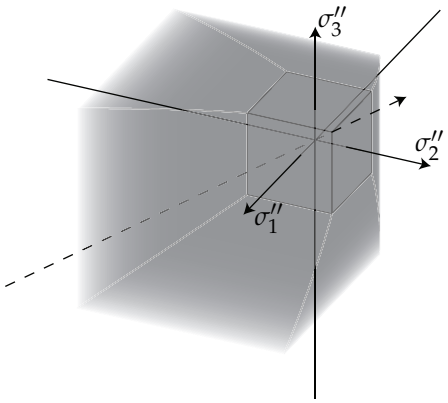

Figure 1.8: The Hoek-Brown criterion combined with a tension cut-off shown in principal stress space.

ening rock mass is modeled, and hence there is a need for further development of the Hoek-Brown criterion for use in Finite Element modeling.

Further, there is reason to assume that, in some scenarios, the Hoek-Brown criterion can overestimate the tensile strength of rock materials, and thus result in structures that are possibly unsafe (Iwanec, 2014). This suggests that the criterion should be modified by a tension-cut off as shown in Figure 1.8. A concept that is also known from the Mohr-Coulomb criterion.

This thesis presents two numerical implementations of the Hoek-Brown criterion. The first accounts for general strain softening behavior while the second constitutes an elastic-perfectly-plastic model with a tension cut-off.

1.2 Thesis outline

Chronologically speaking, the work concerning rock modeling was conducted prior to the work concerning dynamic soil-fluid interaction. However, it is the opinion of the author that the theoretical background of the topics is best explained in opposite order since constitutive modeling is an inherent part of the equations governing dynamic soil-fluid interaction and the finite element method in general. For this reason, the remainder of this thesis is structured as follows.

Chapter 2 gives a brief introduction to the porous nature of rock and soil materials. Firstly, their differences in terms of classification and composition are described. This is followed by an overall assessment of the deformation and strength characteristics of the porous skeleton and how it is affected by the presence of any fluid.

Chapter 3 introduces the theory behind dynamic soil-fluid interaction for saturated porous materials along with its numerical treatment. Initially, the concept of continuum mechanics is introduced along with kinematic, static, and overall constitutive relations. This is followed by an explanation of the governing differential equations of the problem. Lastly, these equations are implemented into the non-linear finite element method resulting in what is known as the u-p-U formulation.

Chapter 4 goes into detail with the constitutive modeling of geotechnical materials using multisurface elasto-plasticity. This is followed by an overview of the return mapping framework used to integrate the constitutive relationship.

Chapter 5 gives a short summary of each of the included papers in this thesis. The chapter is divided into papers concerning rock modeling and dynamic soil-fluid interaction.

Chapter 6 sums up the thesis and gives suggestions for further research in the area.

Chapter 2

Rock and soil behavior

This chapter briefly touches upon the characteristics of geomaterials in terms of classification and composition. Based on this, it is argued that on most scales applicable to geotechnical engineering, the deformation and failure of geomaterials can be ascribed to that of a porous solid skeleton influenced by fluid flow and loading.

2.1 Classification and composition

Geomaterials are typically divided into two distinct categories, namely that of rocks and soils as shown on Figure 2.1. Rock mass is composed of a consolidated, cemented or bonded solid made up of mineral grains such as quartz, calcite or feldspar whereas soils have a relatively loose granular structure consisting of individual solid grains packed together. However, the division is not sharply defined but is a gradual transition from one to the other (Norbury, 2010).

2.1.1 Rocks

In general, rock masses are divided into three groups according to their formation; Sedimentary rock mass is formed through a process known as lithification, in which a constant deposition of sediment results in a densification and fusing of the underlying sediments due to increased pressure. Igneous rock mass originates from minerals that have melted due to the high pressure and heat within the earth and afterwards cooled down. Metamorphic rock mass was initially of sedimentary or igneous nature, but the structure and composition has been significantly altered through heat, pressure, and chemical reactions (Holtz et al., 2010).

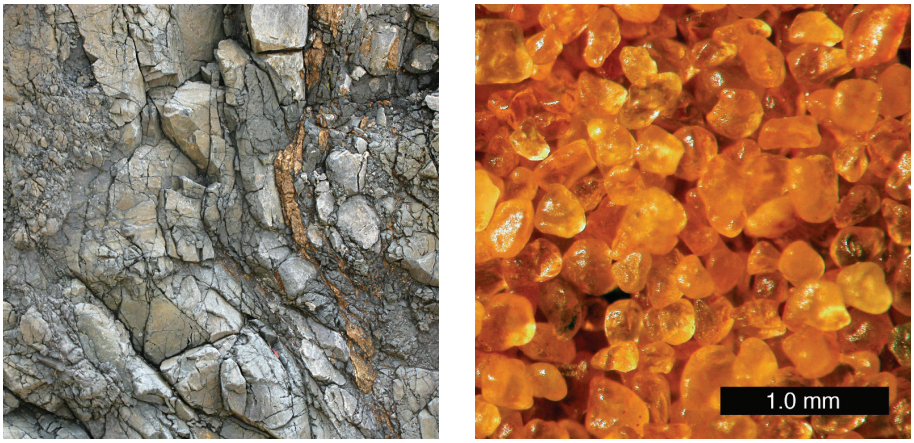

(a) (b)

Figure 2.1: The difference in structure of (a) rock and (b) soil.

Rock mass can be porous and also contain discontinuities such as joints or faults, which have formed due to shifts in loading conditions over time stemming from a number of geological processes. Thus, rock mass ranges from intact rock mass without any discontinuities through rock masses with a few dominating discontinuities to an almost granular mass of heavily jointed rock mass with an indistinct number of evenly distributed discontinuities of random orientation.

2.1.2 Soils

Contrary to rock mass, soils have a relatively loose granular structure consisting of individual solid grains of varying size, shape, and nature packed together. The grains usually consist of deteriorated rock materials, but can also be of organic kind.

Different classification systems exist for soil deposits, such as the Unified Soil Classification System (USCS), the American Association of State Highway and Transportation Officials (AASHTO) system, the U.S. Department of Agriculture (USDA) system, and the European soil classification system (ISO 14688). Common for all of these is the primary classification of soil deposits according to grain size, which is divided into categories such as boulders, gravel, sand, silt, and clay, cf. Table 2.1.

Through a sieve or sedimentation analysis, the grain size distribution of a specific soil deposit can be established, and the soil deposit is afterwards classified according to the relative content of each grain size. Figure 2.2 shows an example hereof. A soil that consists of a wide range of grain sizes is said

Soil fractions		Sub-fractions	Symbols	Size range (mm)
Very coarse soil		Large boulder	LBo	>630
		Boulder	Bo	200 - 630
		Cobble	Co	63 - 200
Coarse soil	Gravel	Coarse gravel	CGr	20 - 63
		Medium gravel	MGr	6.3 - 20
		Fine gravel	FGr	2.0 - 6.3
	Sand	Coarse sand	CSa	0.63 - 2.0
		Medium sand	MSa	0.2 - 0.63
		Fine sand	FSa	0.063 - 0.2
Fine soil	Silt	Coarse silt	CSi	0.02 - 0.063
		Medium silt	MSi	0.0063 - 0.02
		Fine silt	FSi	0.002 - 0.0063
	Clay		Cl	$\leq$0.002

Table 2.1: Several different grain size classification systems exist. This table shows the one specified in ISO 14688-1 (2002)

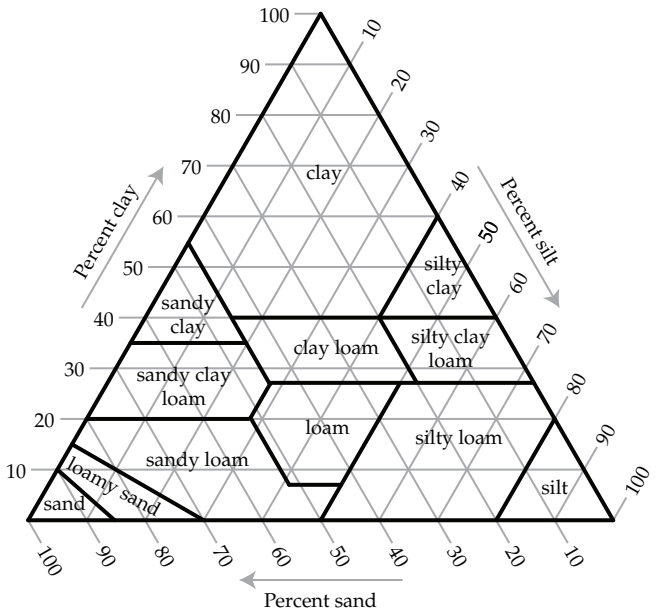

Figure 2.2: Chart used for soil classification according to USDA. After Soil Survey Division Staff (1993)

.

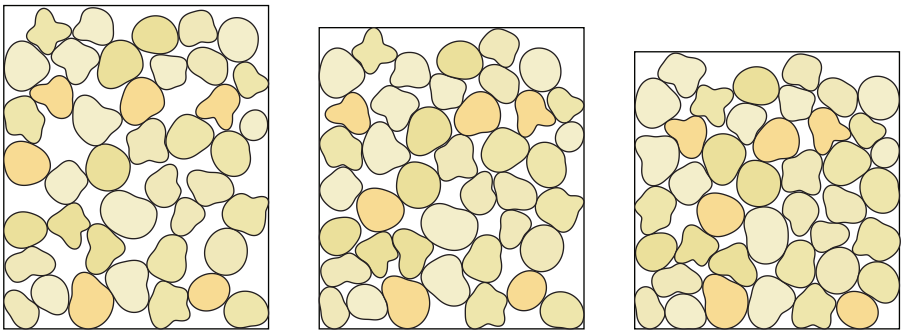

Figure 2.3: The grains of a soil deposit can be packed in different ways. (a) loose, (b) medium, and (c) dense state

to be well graded whereas a soil that primarily consists of grains of similar size is said to be poorly graded.

The shape of gravel, sand, and silt grains ranges from being rounded to angular and tend to have high sphericity, indicating that the grains are around the same size in every dimension. On the other hand, clay particles have low sphericity, meaning that they are relatively large in one or two dimensions (Norbury, 2010).

For fine grained soils, aspects such as water content, organic content and plasticity also weigh in during classification.

Further, depending on how well the grains are packed together, the soil can range from a loose to a dense state as shown in Figure 2.3, which influences the volume of the pores in between the grains.

2.2 Deformation and failure

Due to their differences in composition, geomechanics are ordinarily divided into that of rock mechanics and soil mechanics. However, there is a great deal of similarity between the two branches (Jaeger et al., 2007). Thus for many civil engineering purposes and within the scope of this thesis, they can be treated alike as a porous material consisting of a structural skeleton, cf. Figure 2.4, made up of a solid phase and one or more fluids, typically water or air, that fill the interconnected pores of the solid phase.

The intricate skeleton is capable of transferring loads throughout the material; however, its capabilities and mode of operation is dependent upon the scale as well as material.

In the case of jointed rock masses and coarse grained soils such as gravel or sand, the skeleton is comprised of blocks of rock or grains, which are

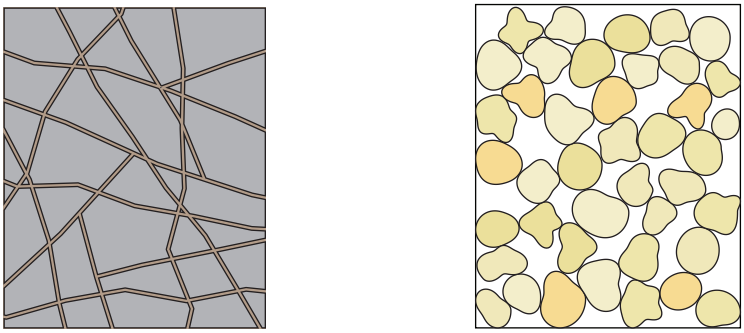

(a) (b)

Figure 2.4: Both rock mass and soils can be regarded as a porous material comprised of a structural skeleton, although the scale can be very different. (a) Sketch of skeleton in jointed rock mass. (b) Sketch of skeleton in sand.

held in place through contact. The deformation and integrity of the skeleton is governed by classical Newtonian mechanics. Even though the individual blocks or grains are able to handle tensile loads, they can not be transferred across the contact interfaces. As a consequence, the skeleton is practically unable to carry any tensile loads. However, compressive normal forces can be transferred in the contact points of the individual grains as well as a certain amount of shear according to Coulomb's law of friction. The blocks or grains can move relative to each other if this shear resistance is reached.

For fine grained soils such as silt or clay, the small size and shape of the grains cause electrochemical forces to play a vital role in the behavior of the skeleton. Owing to this, fine grained soils tend to have cohesive abilities and thus be capable of transferring tensile loads.

For intact rock masses, the skeleton structure is composed of the cemented mineral structure, which is able to transfer relatively large loads in both tension and compression owing to the bounding between them.

The exact way in which a force is transferred through the skeleton is very complex and forms a pattern known as a force chain as illustrated in Figure 2.5 in the case of sand. The loading causes deformation of the skeleton and alters the force chain. Therefore, soil and rock materials tend to show a non-linear relationship between loads and displacements.

For small loads, the deformations are reversible, meaning that the skeleton to a large extent reverts to its original position and shape if the load is removed. Contrary, for large loads, only some reversibility is maintained due to sliding of grains, fracturing or crushing, and the skeleton structure has been affected permanently, giving a non-unique relationship between the loads and displacements.

Further, owing to the restructuring of the skeleton, the volume needed to

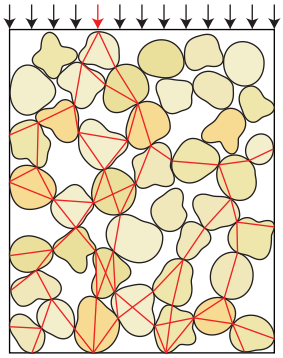

Figure 2.5: Load applied to soil skeleton. The lines in red show how part of the load is transferred through the skeleton through the contact points of the grains, resulting in so called force chains.

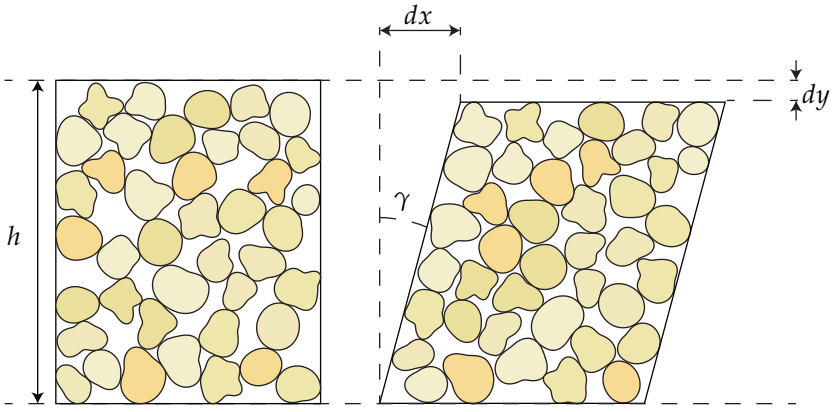

Figure 2.6: Volume change of skeleton during shearing. Loose soils, as shown here, tend to contract, while dense soils and rock material tend to dilate.

contain the skeleton can be severely altered. This is especially the case during shearing in sand deposits, cf. Figure 2.6. Loosely packed soil deposits tend to shrink in volume due to a more efficient packing of the grains whereas densely packed soil deposits and rock material tend to expand in volume because the grains or fractured surfaces need to slide above one another.

The reorganization of the skeleton can have substantial effects on its further ability to deform and carry loads. If e.g. the atomic bonds within the minerals of a rock deposit are broken, the ability to carry tensile stresses across this connection is lost. Another example is that the volume expansion of a dense deposit ceases after a certain amount of shearing.

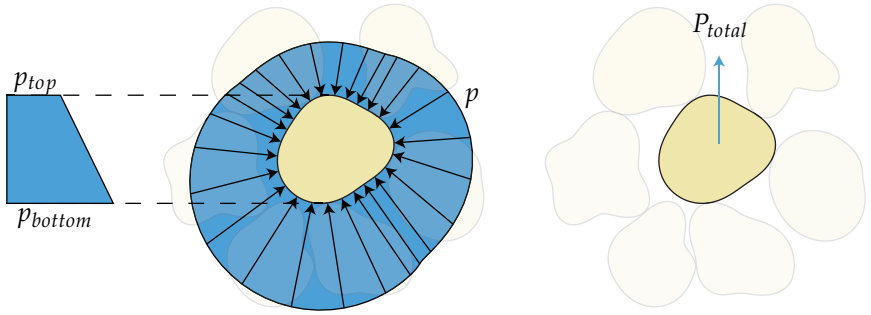

Figure 2.7: Hydrostatic pressure causes uplift on the particles of the skeleton.

2.3 Fluid interaction

As mentioned previously, fluid within the interconnected voids of the skeleton can have significant impact on the mechanics of the skeleton and vice versa. In this section, it is assumed that the fluid is in the form of water, as is most common within the field of geotechnical engineering, and that the material is completely saturated. Yet the principles apply to any fluid, be it gas or liquid, even though the effects are often negligible for fluids of low mass, low viscosity, and high compressibility such as air and are thus never applied to dry soils.

In a stagnant fluid, the pressure distribution, p, is hydrostatic owing to the fluid's density and gravity. The pressure acts on the skeleton and gives rise to and uplift force as shown in Figure 2.7 due to the difference in pressure from the top of the grain to the bottom of the grain. In addition to this, the solids of the skeleton respond to the pressure by compressing a small amount.

For fluids in motion through the skeleton, the exact pressure variation is dependent on the characteristics and velocity of the fluid as well as on the configuration of the skeleton. In addition to pressure variations, the skeleton is also affected by frictional drag owing to the viscosity of the fluid. However, in an average sense, the skeleton is subject to a net force in the direction of the flow, which is dependent on the permeability of the skeleton and proportional to the average velocity of the flow.

The forces from the fluid onto the skeleton effectively alter the contact pressure between the grains in soil deposits, which has a high impact on the integrity of the skeleton. In some situations, such as that of an upwards flow through an unloaded sand deposit, the contact forces stemming from the mass of the grains can be completely diminished by the flow, and the skeleton is thus no longer able to resist any shear, effectively acting as a liquid. In other situations, such as that of a downwards flow through an unloaded sand deposit, the contact forces are increased.

Another implication of the presence of fluid is that, during deformation of the skeleton, the volume of the pores is affected as shown in Figure 2.6. These volume changes result in fluid pressure changes in accordance with the compressibility of the fluid, which in turn drives a fluid flow. If a certain location in the skeleton experiences a decrease in pore volume, the pressure increases and drives a flow away from the location. Contrary, if the location experiences an increase in pore volume, the fluid expands and the pressure decreases and drives a flow towards the location. Further, the change in pressure can be so large that it affects the phase of the fluid. This is e.g. the case when the pressure in a liquid drops below that of its vapor pressure and the liquid starts to boil. Such phase transformations change the properties of the fluid and hence affect the drag forces on the skeleton.

Chapter 3

Dynamic soil-fluid interaction

In this chapter, the basics behind dynamic soil-fluid interaction will be described using the concept of continuum mechanics. Strains and stresses are introduced for the skeleton; however, detailed description of the constitutive relation between them is postponed to the ensuing chapter. The governing equations of soil-fluid interaction will be established along with relevant boundary conditions using index notation. Afterwards, the discretization in space and time is established in a manner suitable for numerical implementation in a standard finite element framework. The chapter is based on Zienkiewicz and Shiomi (1984), Zienkiewicz et al. (1999) and Jeremić et al. (2008).

3.1 Continuum approach

Ideally, the complex behavior of rocks and soils should be modeled at the molecular level in order to truly simulate e.g. the cohesion of clay particles or the breaking of atomic bonds within the crystal structure of minerals. The next best thing would be to model geomaterials at the grain level where the deformation and displacement of the individual solid grains and fluids are computed using classical Newtonian mechanics. However, since each particle of the skeleton is unique and typically very small compared to the size of the structure, these approaches are generally not practically feasible even with today's computer technology.

For this reason, most geotechnical engineering relies on continuum mechanics instead, meaning that the material is treated as a continuous mass that on average behaves as a large – compared to the characteristics of the

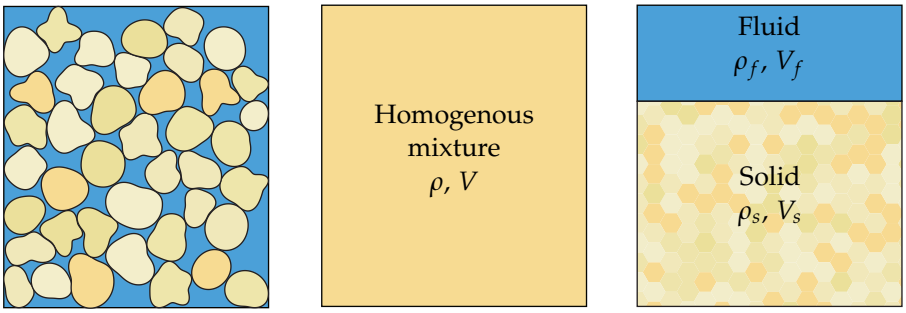

Figure 3.1: Continuum representation of solid skeleton and fluid. (a) Particles and fluid in a sample of saturated sand. (b) Homogenous mixture. (c) Volume fractions of homogenous mixture.

skeleton – volume of material. In combination with any fluids present in the skeleton, their combined behavior can be perceived as a homogeneous mixture of a solid phase and one or more fluid phases, which each takes up a fraction of the volume, cf. Figure 3.1. The volume fraction V_f constitutes the volume in the interconnected pores capable of transporting fluids through the skeleton while V_s is the volume of all solids as well as any pores sealed off from the rest.

Thus, the porosity of the continuum, n, can be defined as the volume fraction of the pores compared to the entire volume

$$n = \frac{V_f}{V_f + V_s} = \frac{V_f}{V} \tag{3.1}$$

using this definition, the density of the mixture, ρ, is given by

$$\rho = (1 - n)\,\rho_s + n\rho_f \tag{3.2}$$

where ρ_s and ρ_f are the average densities of the solid material and fluid respectively.

3.1.1 Kinematics

Due to the ability of the fluid to move relative to the skeleton, it is necessary to keep track of the displacements of both of them. The displacements of an arbitrary point within the skeleton follows the usual continuum approach, so that the displacement along direction $i = \{x,\ y,\ z\}$ is denoted u_i, where x, y and z denote the directions of the orthogonal basis for the three dimensional space of the problem. The velocity, $\dot{u}_i$, and acceleration, $\ddot{u}_i$, of a point within

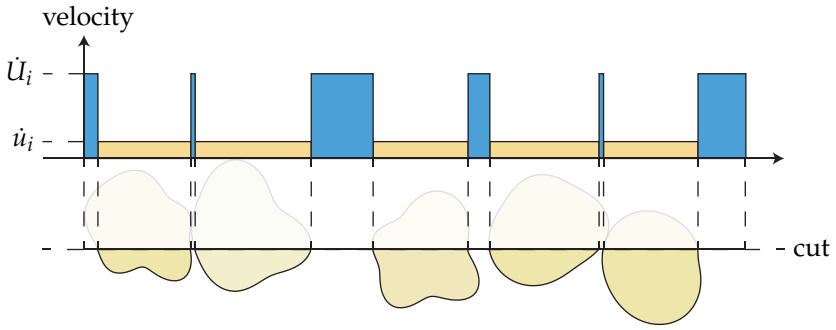

Figure 3.2: Velocity distribution of solid and fluid phases in a porous material.

the skeleton is further given by

$$\dot{u}_i = \frac{\partial u_i}{\partial t} \qquad \text{and} \qquad \ddot{u}_i = \frac{\partial \dot{u}_i}{\partial t} = \frac{\partial^2 u_i}{\partial t^2} \tag{3.3}$$

where t denotes time.

The appertaining small strain tensor, ε_{ij}, accounts for the deformation of the skeleton and is given by

$$\varepsilon_{ij} = \frac{1}{2}\left(u_{i,j} + u_{j,i}\right) \qquad \text{where} \qquad u_{i,j} = \frac{\partial u_i}{\partial j} \tag{3.4}$$

where $j = \{x,\ y,\ z\}$ respectively. In a similar fashion, the displacement, velocity, and acceleration of the fluid is denoted U_i, $\dot{U}_i$, and $\ddot{U}_i$. Figure 3.2 shows the velocity difference between the fluid and the skeleton at an arbitrary section through the porous material. Since fluid flow only occurs in the pores, it can be convenient later on to define an average fluid velocity across the cross section relative to the skeleton, which is given by

$$\dot{w}_i = n\left(\dot{U}_i - \dot{u}_i\right) \tag{3.5}$$

since the relative area of the pores in the cross section is given by the porosity n. This velocity is known as the seepage velocity.

3.1.2 Statics

Further, the stresses within the material need to be split into two parts. One part constitutes the pressure, p, within the fluid, which is taken as positive in compression. The second part relates to the stresses carried by the skeleton, known as effective stresses, taken as positive in tension as is customary in most finite element contexts.

Figure 3.3 shows an arbitrary cut through a porous material. The cross sectional area of the cut is denoted A. Part of the area, nA, consists of pores

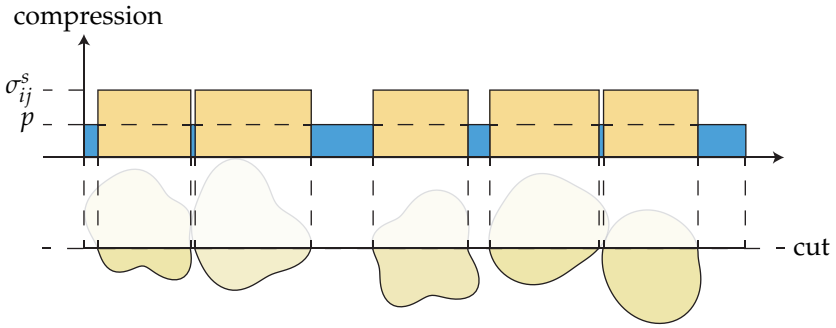

Figure 3.3: Stress distribution across a cut in a porous material.

and only transfers the pore pressure p across the boundary of the cut, while the remaining area $(1-n)\,A$ consists of the skeleton and transfers a stress, σ^s_{ij}, across the boundary. However, part of this stress is stemming from the pore pressure acting on the skeleton while the remainder, $\sigma^{s\prime}_{ij}$, is related to loading of the skeleton. In the continuum approach, the stresses are averaged across the entire cross section, resulting in a total stress, $\boldsymbol{\sigma}$, given by

$$\sigma_{ij} = (1-n)\left(\sigma^{s\prime}_{ij} - \delta_{ij}p\right) - n\delta_{ij}p = \sigma'_{ij} - \delta_{ij}p \tag{3.6}$$

where

$$\sigma'_{ij} = (1-n)\,\sigma^{s\prime}_{ij} \tag{3.7}$$

denotes the classical effective stresses of the skeleton as proposed by Terzaghi. The negative sign originates from the fact that p and σ differ in sign convention.

3.1.3 Constitutive relation

In classical non-linear soil mechanics, the relationship between the Terzaghi effective stresses and the strains of the skeleton are governed by the incremental relation

$$\dot{\sigma}'_{ij} = \dot{\sigma}_{ij} + \delta_{ij}\dot{p} = D^{ep}_{ijkl}\dot{\varepsilon}_{kl} \tag{3.8}$$

where D^{ep}_{ijkl} is the fourth order elasto-plastic infinitesimal constitutive tensor, which will be described in more detail in section 4.1.

However, in poro-elasto-plasticity, this relation brings along some inconsistencies with regards to the strain definition, as illustrated in the following example.

Consider a porous skeleton being submerged into a basin of fluid. The increase in pressure, $\dot{p}$, due to the density of the fluid causes a simultaneous

increment $\dot{\sigma}_{ij} = -\delta_{ij}\dot{p}$ in total stresses. The resulting increment in the effective Terzaghi stresses is thus given as

$$\dot{\sigma}'_{ij} = -\delta_{ij}\dot{p} + \delta_{ij}\dot{p} = 0 \tag{3.9}$$

according to (3.6). Further, the ubiquitous pore pressure increment results in a volumetric compression of the entire skeleton given by the strain increment

$$\dot{\varepsilon}_{ij} = -\delta_{ij}\frac{1}{3K_s}\dot{p} \tag{3.10}$$

where K_s is the average bulk modulus of the solid material of which the skeleton is composed. The net result is a volumetric strain of

$$\dot{\varepsilon}_v = \dot{\varepsilon}_{ii} = \dot{\varepsilon}_{xx} + \dot{\varepsilon}_{yy} + \dot{\varepsilon}_{zz} = -\frac{1}{K_s}\dot{p} \tag{3.11}$$

Thus, the relation stated in (3.8) can not be fulfilled for a linear-elastic material. In order to rectify this it would need correction according to

$$\dot{\sigma}'_{ij} - \delta_{ij}D^{ep}_{ijkl}\delta_{kl}\frac{1}{3K_s}\dot{p} = D^{ep}_{ijkl}\dot{\varepsilon}_{kl} \tag{3.12}$$

For isotropic materials, it can be found that

$$\delta_{ij}D^{ep}_{ijkl}\delta_{kl}\frac{1}{3K_s} = \frac{K^{ep}}{K_s} \tag{3.13}$$

where K^{ep} is the tangential bulk modulus of the skeleton. On account of this, a new effective stress is defined, given as

$$\dot{\sigma}''_{ij} = \dot{\sigma}'_{ij} - \delta_{ij}\frac{K^{ep}}{K_s}\dot{p} = \dot{\sigma}_{ij} + \alpha\delta_{ij}\dot{p} \tag{3.14}$$

where

$$\alpha = 1 - \frac{K^{ep}}{K_s} \tag{3.15}$$

This definition of effective stresses is known as the effective Biot stresses and α is known as the Biot coefficient. As shown above, this set of effective stresses fulfill the relationship

$$\dot{\sigma}''_{ij} = D^{ep}_{ijkl}\dot{\varepsilon}_{kl} \tag{3.16}$$

As can be seen from (3.15), the Biot coefficient depends on the bulk modulus of the skeleton, as well as the bulk modulus of the solid of which the skeleton is made up. For most soils where the skeleton is relatively compressible compared to the skeleton solid, $K^{ep} \ll K_s$, the Biot coefficient approaches 1 and the effective Biot stresses approach the Terzaghi effective stresses. However, in concrete and rock mass where the skeleton bulk modulus is on the same order of magnitude as the solid, α can reach a magnitude of around 0.5 in some cases, cf. Table 3.1.

Material	K^{ep} [MPa]	K_s [MPa]	α
Quartzitic sandstone	$17{\cdot}10^3$	$37{\cdot}10^3$	0.54
Quincy granite (30 m deep)	$13{\cdot}10^3$	$52{\cdot}10^3$	0.75
Vermont marble	$5.6{\cdot}10^3$	$71{\cdot}10^3$	0.92
Concrete (approximately)	$5{\cdot}10^3$	$40{\cdot}10^3$	0.88
Dense sand	56	$36{\cdot}10^3$	0.9985
Loose sand	11	$36{\cdot}10^3$	0.9997
London clay (over consolidated)	13	$50{\cdot}10^3$	0.99975
Gosport clay (normally consolidated)	1.7	$50{\cdot}10^3$	0.99997

Table 3.1: The Biot coefficient of different materials. After Andersen (2007).

3.2 The governing equations

Besides the constitutive relationship given by (3.16), the governing equations behind poro-elasto-plasticity consist of three physical necessities. Firstly, the equilibrium equations must be fulfilled for the entirety of the solid-fluid mixture. Secondly, the equilibrium equations must be fulfilled for the pore fluid. Finally, the mass balance of the fluid flow through the skeleton must be accounted for.

3.2.1 Equilibrium of mixture

Using a Lagrangian formulation of the solid skeleton, the equations governing equilibrium of the mixture can be derived from Figure 3.4 as

$$\sigma_{ij,j} + \rho b_i = \rho \ddot{u}_i + \rho_f \left(\ddot{w}_i + \dot{w}_j \dot{w}_{i,j} \right) \tag{3.17}$$

The left-hand side corresponds to the forces acting on the mixture while the right-hand side accounts for the change of momentum of the system.

The first term on the left-hand side accounts for the divergence of the total stresses acting on the sides of the infinitesimal continuum while the second term accounts for the inclusion of any body forces, typically gravity, given by ρb_i.

The first term on the right-hand side accounts for the change of momentum of the solid-fluid mixture as a whole while the second term on the right-hand side accounts for the additional change of momentum of the fluid due acceleration relative to the skeleton. Since the motion of the fluid is relative to the skeleton, it is written using an Eulerian formulation. $\ddot{w}_i$ denotes the change in the velocity field within the continuum in the time increment dt, while the convective term $\dot{w}_j \dot{w}_{i,j}$ denotes acceleration of the fluid in the time interval dt, due to a movement of the fluid to a location of different velocity.

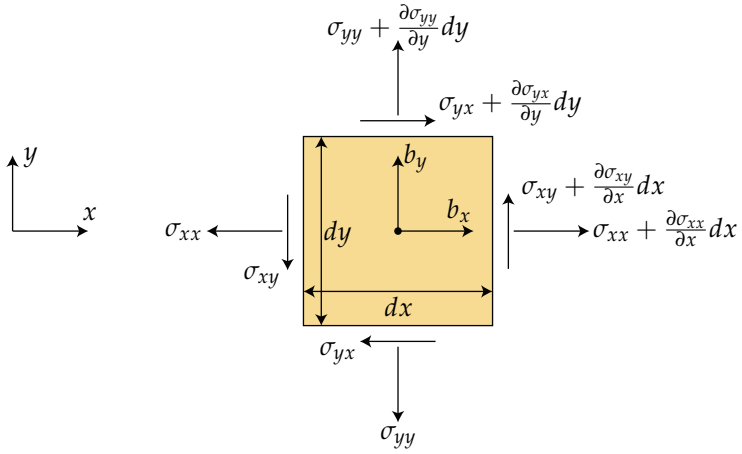

Figure 3.4: Equilibrium of infinitesimal volume of solid-fluid mixture in two dimensions.

3.2.2 Equilibrium of fluid flow

Using the same Eulerian formulation for the fluid within the control volume of the solid skeleton, as shown on Figure 3.5, the equilibrium of the fluid flow is given by

$$-p_{,i} - R_i + \rho_f b_i = \rho_f \ddot{u}_i + \rho_f \frac{\ddot{w}_i + \dot{w}_j \dot{w}_{i,j}}{n} \tag{3.18}$$

Again, the left-hand side corresponds to the forces acting on the fluid while the right-hand side accounts for the change of momentum of the system.

The first term on the left-hand side accounts for the gradient of the pressure acting on the fluid. The second term accounts for the viscous drag forces experienced by the fluid, as it moves through the skeleton. The last term on the left hand side represents any body forces applied to the fluid.

The first term on the right-hand side accounts for the change of momentum of the fluid due to simultaneous acceleration of both skeleton and fluid while the second term accounts for the relative acceleration of the fluid with regards to the skeleton, just as for the solid-fluid mixture equilibrium above. However, since we are only considering the fluid mass and the fluid flow is confined to the pores of the skeleton, the actual velocity is $1/n$ times higher.

The viscous drag forces on the skeleton from the fluid, R_i, are related to the seepage velocity through Darcy's seepage law as

$$R_i = k_{ij}^{-1} \dot{w}_j \tag{3.19}$$

where k_{ij} is a second order tensor representing the ability of the particular fluid to flow through the skeleton. The negative sign in (3.18) originates from the fact that the drag forces on the fluid from the skeleton are opposite the flow direction. For isotropic materials, the permeability is uniform

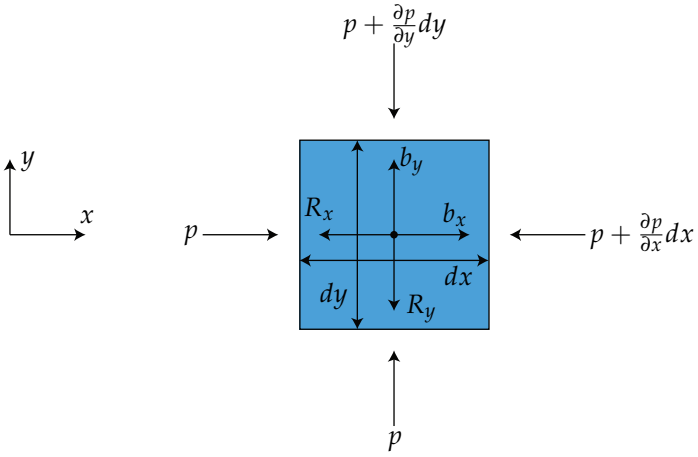

Figure 3.5: Equilibrium of infinitesimal volume of fluid in two dimensions.

in all directions, and a single variable, k, suffice. k_{ij} has the dimension of [length]^3 [time] / [mass] and is related to the more common measures of hydraulic conductivity, k'_{ij} of dimension [length] / [time], and permeability, K'_{ij} of dimension [length]^2 through

$$k_{ij} = \frac{k'_{ij}}{\rho'_f g'} = \frac{K'_{ij}}{\mu} \tag{3.20}$$

where ρ'_f is the density of the fluid, g' the gravity acceleration at which k'_{ij} is measured and μ is the dynamic viscosity of the fluid. Only the permeability K'_{ij} is independent of the fluid properties.

3.2.3 Mass balance of fluid flow

The last equation concerns the mass balance of the fluid flow. Again, based on the previous control volume, the mass balance can be found to be

$$\dot{w}_{i,i} = -\dot{\varepsilon}_{ii} - \frac{n\dot{p}}{K_f} - \frac{(1-n)\,\dot{p}}{K_s} + \frac{K^{ep}}{K_s}\left(\dot{\varepsilon}_{ii} - \frac{\dot{p}}{K_s}\right) - n\frac{\dot{\rho}_f}{\rho_f} - \dot{s}_0 \tag{3.21}$$

The left-hand side accounts for the net fluid flow out of the control volume. This should be balanced by the decrease in storage capabilities of the skeleton due to changes in pore volume and expansion of the fluid.

The first term on the right-hand side accounts for the general decrease in pore volume due to volumetric compaction of the solid skeleton as a whole. The second term accounts for expansion of the fluid owing to pressure changes where K_f is the bulk modulus of the fluid.

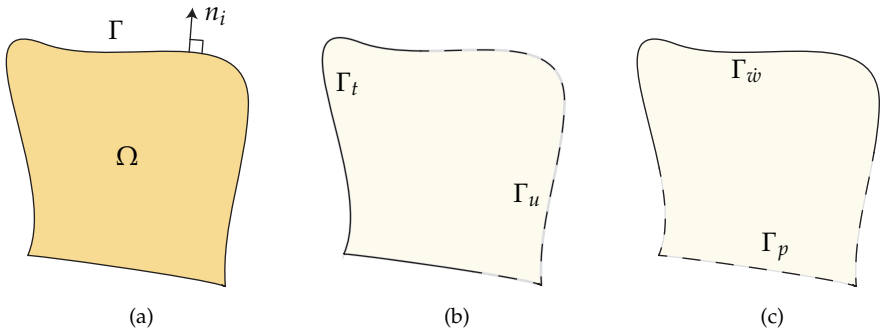

Figure 3.6: Boundary conditions of the domain. (a) Domain, Ω, and associated boundary, Γ, with the outwards normal n_i. (b) The boundary can be split into Γ_t, where the traction is known, and Γ_u, where the solid displacement is known. (c) Further, the boundary can be split into Γ_p, where the pressure is known, and $\Gamma_{\dot{w}}$, where the outwards flow is known.

The third and fourth terms account for the decrease in volume of the solid material of which the skeleton is composed. Partly because of a change in fluid pressure, partly because of a change in effective Terzaghi stresses, σ'_{ij}.

The fifth term accounts for a change in density of the fluid owing to e.g. thermal expansion. Finally, the last term accounts for a possible source or sink of fluid, like e.g. a well.

The governing equation of (3.21) can be written as

$$\bar{w}_{i,i} + \alpha\dot{\varepsilon}_{ii} + \frac{\dot{p}}{Q} + n\frac{\dot{\rho}_f}{\rho_f} + \dot{s}_0 = 0 \tag{3.22}$$

where

$$\frac{1}{Q} = \frac{n}{K_f} + \frac{\alpha - n}{K_s} \tag{3.23}$$

quantifies the combined compressibility of the fluid and the skeleton material.

3.2.4 Boundary conditions

In order to apply the governing equations to a specific problem, a problem geometry has to be defined by a domain, Ω, bounded by a boundary, Γ, as shown on Figure 3.6a. Further, the boundaries need to be fitted with appropriate boundary conditions that reflect the problem.

In typical scenarios, for a part of the boundary, Γ_u, knowledge of the movement of the solid skeleton is available, $\tilde{u}_i$, while the total traction, $\sigma_{ij}n_i$, on the boundary is unavailable. In this context, n_i designates the outward normal to the boundary. Contrary, for the remaining part of the boundary, Γ_t, the total traction, $\tilde{t}_i$, is known while the skeleton movement is unknown, cf. Figure 3.6b.

Further, for a part of the boundary, Γ_p, the pore pressure, $\tilde{p}$, is known while the flow across the boundary, $\dot{w}_i n_i$, is unknown. Similarly, for the remaining part of the boundary, $\Gamma_{\dot{w}}$, the flow across the boundary, $\dot{\tilde{w}}_n$, is known, while the pressure is unknown, cf. Figure 3.6c.

Based on these considerations, the following boundary conditions can be formulated

$$\sigma_{ij} n_j - \tilde{t}_i = 0 \quad \text{on} \quad \Gamma_t \quad \text{and} \quad u_i - \tilde{u}_i = 0 \quad \text{on} \quad \Gamma_u \tag{3.24}$$

$$p - \tilde{p} = 0 \quad \text{on} \quad \Gamma_p \quad \text{and} \quad n_i \dot{w}_i - \dot{\tilde{w}}_n = 0 \quad \text{on} \quad \Gamma_{\dot{w}} \tag{3.25}$$

where the different parts of the boundary encompass the entire boundary in the following way

$$\Gamma_t \cap \Gamma_u = \Gamma_p \cap \Gamma_{\dot{w}} = \emptyset \qquad \Gamma_t \cup \Gamma_u = \Gamma_p \cup \Gamma_{\dot{w}} = \Gamma \tag{3.26}$$

3.3 Implementation into the non-linear finite element method, the $u - p - U$ formulation

The above governing equations need to be described in a format suitable for computational arithmetic. In order to do so, a vectorial notation is employed as described in the following.

The skeleton and fluid displacements are expressed as column vectors according to

$$u_i = \boldsymbol{u} = \begin{bmatrix} u_x & u_y & u_z \end{bmatrix}^T \qquad \text{and} \qquad U_i = \boldsymbol{U} = \begin{bmatrix} U_x & U_y & U_z \end{bmatrix}^T \tag{3.27}$$

where ^{T} denotes the transpose. Similar notation is used for $\dot{u}_i$, $\ddot{u}_i$, $\dot{U}_i$ and $\ddot{U}_i$.

With the adaption of engineering strains, the second order tensors of strains and stresses can be written in vectorial form as

$$\boldsymbol{\varepsilon} = \begin{bmatrix} \varepsilon_{xx} & \varepsilon_{yy} & \varepsilon_{zz} & \gamma_{xy} & \gamma_{xz} & \gamma_{yz} \end{bmatrix}^T \tag{3.28}$$

$$\sigma_{ij} = \boldsymbol{\sigma} = \begin{bmatrix} \sigma_{xx} & \sigma_{yy} & \sigma_{zz} & \sigma_{xy} & \sigma_{xz} & \sigma_{yz} \end{bmatrix}^T \tag{3.29}$$

where the symmetry of the tensors have been exploited. Similar notation for σ'_{ij} and σ''_{ij} is used. The relation between displacements and strains can be written as

$$\boldsymbol{\varepsilon} = \tilde{\boldsymbol{\nabla}} \boldsymbol{u} \tag{3.30}$$

where

$$\tilde{\boldsymbol{\nabla}} = \begin{bmatrix} \frac{\partial}{\partial x} & 0 & 0 \\ 0 & \frac{\partial}{\partial y} & 0 \\ 0 & 0 & \frac{\partial}{\partial z} \\ \frac{\partial}{\partial y} & \frac{\partial}{\partial x} & 0 \\ \frac{\partial}{\partial z} & 0 & \frac{\partial}{\partial x} \\ 0 & \frac{\partial}{\partial z} & \frac{\partial}{\partial y} \end{bmatrix} \tag{3.31}$$

Further, fourth order tensors, such as D_{ijkl} can be written in matrix notation, $\boldsymbol{D}$, as a 6×6 matrix.

3.3.1 Rewritten equation sets

Using the vectorial notation and substituting the terms concerning the fluid displacement relative to the skeleton, w_i, with their absolute counterparts, U_i, the governing equations can be cast in a form more suitable for numerical manipulations. In doing so, the convective terms of the fluid, $\dot{w}_j \dot{w}_{i,j}$, are dropped since they are of minor importance compared to the inaccuracies associated with the measurement of the permeability and can lead to numerical complications. Insertion of the identity of (3.5) into (3.18) and multiplication by n results in the equilibrium conditions for the fluid stated as

$$-n\boldsymbol{\nabla} p + n\rho_f \boldsymbol{b} - n\rho_f \ddot{\boldsymbol{U}} - n\boldsymbol{R} = 0 \tag{3.32}$$

where $\boldsymbol{\nabla}$ is the gradient operator given by

$$\boldsymbol{\nabla} = \begin{bmatrix} \frac{\partial}{\partial x} \\ \frac{\partial}{\partial y} \\ \frac{\partial}{\partial z} \end{bmatrix} \tag{3.33}$$

and the viscous drag forces are given by

$$\boldsymbol{R} = \boldsymbol{k}^{-1}\boldsymbol{w} = n\boldsymbol{k}^{-1}\left(\dot{\boldsymbol{U}} - \dot{\boldsymbol{u}}\right) \tag{3.34}$$

Further, by subtracting (3.32) from (3.17) and using the effective Biot stresses, the equilibrium conditions for the skeleton can be written as

$$\tilde{\boldsymbol{\nabla}}^T \boldsymbol{\sigma}'' - (\alpha - n)\,\boldsymbol{\nabla} p + (1-n)\,\rho_s \boldsymbol{b} - (1-n)\,\rho_s \ddot{\boldsymbol{u}} + n\boldsymbol{R} = 0 \tag{3.35}$$

If the term accounting for changes in the fluid density as well as the source term is omitted from the equation concerning conservation of mass, it can be stated as

$$-n\boldsymbol{\nabla}^T \dot{\boldsymbol{U}} - (\alpha - n)\,\boldsymbol{m}\dot{\varepsilon} - \frac{1}{Q}\dot{p} = 0 \tag{3.36}$$

where

$$\boldsymbol{m} = [1\ 1\ 1\ 0\ 0\ 0]^T \tag{3.37}$$

Since all terms are related to the first derivative with respect to time, the equation can be integrated in time, giving

$$-n\boldsymbol{\nabla}^T\boldsymbol{U} - (\alpha - n)\,\boldsymbol{m}\boldsymbol{\varepsilon} - \frac{1}{Q}p - f_{p0} = 0 \tag{3.38}$$

where f_{p0} is an integration constant, that can be found by fulfillment of (3.38) at the initial configuration, denoted by subscript t_0, where often $\boldsymbol{U}_{t_0} = \boldsymbol{\varepsilon}_{t_0} = \boldsymbol{0}$ but $p_{t_0} \neq 0$ due to hydrostatic water pressure. (3.32), (3.35) and (3.38) form the basis for the numerical implementation into the finite element method. The independent unknowns amount to the solid and fluid displacements, u and U, as well as their first and second derivatives with respect to time together with the fluid pressure p. Owing to this, it is known as the $u - p - U$-formulation.

3.3.2 Discretization in space

So far, the governing equations and the associated boundary conditions have been established in their strong form. Thus the governing equations represents an infinitesimal part, $d\Omega$, of the entire domain, Ω, while the boundary conditions apply for an infinitesimal part, $d\Gamma$, of the entire boundary Γ. At every single point within the domain and on the boundary, the equations have to be fulfilled. Exploiting this fact, premultiplying the equations with an arbitrary weighting function and integrating over the domain including boundaries should hence amount to zero. Using integration by parts, it is often possible to obtain an equation with lower order derivatives of the unknowns in exchange for derivatives of the weighting function. Such an operation hence decreases the requirements of the continuity of the unknowns in exchange for increased continuity of the weighting function. Owing to this, such formulations are known as weak formulations. For further details see e.g. Zienkiewicz and Taylor (2000) and Bathe (1996).

The weak formulation is used in conjunction with an approximation of the unknown fields, which are described by a set of discrete points within the domain and on the boundary, known as nodes, along with an appropriate, but approximate, interpolation between these points. Thus, the skeleton displacement field can be expressed by

$$\boldsymbol{u} \approx \boldsymbol{N}^u\bar{\boldsymbol{u}} \tag{3.39}$$

where $\boldsymbol{N}^u$ is the interpolation matrix, which depend upon the spatial coordi-

nates, and is typically given by

$$\boldsymbol{N}^u = \begin{bmatrix} N^u_{x_1} & 0 & 0 & \cdots & N^u_{x_k} & 0 & 0 \\ 0 & N^u_{y_1} & 0 & \cdots & 0 & N^u_{y_k} & 0 \\ 0 & 0 & N^u_{z_1} & \cdots & 0 & 0 & N^u_{z_k} \end{bmatrix} \tag{3.40}$$

in which k in this context denotes the number of nodes. $\bar{\boldsymbol{u}}$ is a vector containing values of the dependent displacement field at the discrete points in the domain and their variation with time

$$\bar{\boldsymbol{u}} = \begin{bmatrix} u_{x_1} \\ u_{y_1} \\ u_{z_1} \\ \cdots \\ u_{x_k} \\ u_{y_k} \\ u_{z_k} \end{bmatrix} \tag{3.41}$$

In a similar manner, the pore pressure field and fluid displacement can be approximated by

$$\boldsymbol{U} \approx \boldsymbol{N}^U \bar{\boldsymbol{U}} \qquad \text{and} \qquad \boldsymbol{p} \approx \boldsymbol{N}^p \bar{\boldsymbol{p}} \tag{3.42}$$

Using the weighted residual Galerkin approach, a similar description is used for the arbitrary weighting functions, utilizing the same interpolation functions, but assuming the discrete weights to be arbitrary.

Based on these considerations, the discretized version of the skeleton equilibrium equations, (3.35), can be written as

$$\boldsymbol{M}_s \ddot{\bar{\boldsymbol{u}}} + \boldsymbol{C}_1 \dot{\bar{\boldsymbol{u}}} - \boldsymbol{C}_2 \dot{\bar{\boldsymbol{U}}} - \boldsymbol{G}_1 \bar{\boldsymbol{p}} + \int_\Omega \boldsymbol{B} \boldsymbol{\sigma}'' d\Omega = \bar{\boldsymbol{f}}_s \tag{3.43}$$

The discretized version of the mass balance of the fluid flow, (3.38), can be stated as

$$-\boldsymbol{G}_1^T \bar{\boldsymbol{u}} - \boldsymbol{P} \bar{\boldsymbol{p}} - \boldsymbol{G}_2^T \bar{\boldsymbol{U}} = \bar{\boldsymbol{f}}_{p0} \tag{3.44}$$

And finally, the discretized version of the fluid equilibrium equations, (3.32), becomes

$$-\boldsymbol{G}_2 \bar{\boldsymbol{p}} - \boldsymbol{C}_2^T \dot{\bar{\boldsymbol{u}}} + \boldsymbol{C}_3 \dot{\bar{\boldsymbol{U}}} + \boldsymbol{M}_f \ddot{\bar{\boldsymbol{U}}} = \bar{\boldsymbol{f}}_f \tag{3.45}$$

where

$$\boldsymbol{M}_s = \int_\Omega (1-n)\, \rho_s \left(\boldsymbol{N}^u\right)^T \boldsymbol{N}^u d\Omega \tag{3.46}$$

$$\boldsymbol{M}_f = \int_\Omega n \rho_f \left(\boldsymbol{N}^U\right)^T \boldsymbol{N}^U d\Omega \tag{3.47}$$

$$\boldsymbol{C}_1 = \int_\Omega n^2 \left(\boldsymbol{N}^u\right)^T \boldsymbol{k}^{-1} \boldsymbol{N}^u d\Omega \tag{3.48}$$

$$\boldsymbol{C}_2 = \int_\Omega n^2 \left(\boldsymbol{N}^u\right)^T \boldsymbol{k}^{-1} \boldsymbol{N}^U d\Omega \tag{3.49}$$

$$\boldsymbol{C}_3 = \int_\Omega n^2 \left(\boldsymbol{N}^U\right)^T \boldsymbol{k}^{-1} \boldsymbol{N}^U d\Omega \tag{3.50}$$

$$\boldsymbol{G}_1 = \int_\Omega (\alpha - n) \boldsymbol{B}^T \boldsymbol{m} \boldsymbol{N}^p d\Omega \tag{3.51}$$

$$\boldsymbol{G}_2 = \int_\Omega n \left(\tilde{\boldsymbol{\nabla}} \boldsymbol{N}^U\right)^T \boldsymbol{m} \boldsymbol{N}^p d\Omega \tag{3.52}$$

$$\boldsymbol{P} = \int_\Omega \frac{1}{Q} \left(\boldsymbol{N}^p\right)^T \boldsymbol{N}^p d\Omega \tag{3.53}$$

$$\boldsymbol{B} = \tilde{\boldsymbol{\nabla}} \boldsymbol{N}^u \tag{3.54}$$

$$\bar{\boldsymbol{f}}_s = \int_\Omega (1-n) \rho_s \left(\boldsymbol{N}^u\right)^T \boldsymbol{b} d\Omega - \int_{\Gamma_p} (\alpha - n) \tilde{p} \left(\boldsymbol{N}^u\right)^T \boldsymbol{n} d\Gamma_p + \int_{\Gamma_t} \left(\boldsymbol{N}^u\right)^T \tilde{\boldsymbol{t}}'' d\Gamma_t \tag{3.55}$$

$$\bar{\boldsymbol{f}}_{p0} = -\boldsymbol{G}_1^T \bar{\boldsymbol{u}}_{t_0} - \boldsymbol{P} \bar{\boldsymbol{p}}_{t_0} - \boldsymbol{G}_2^T \bar{\boldsymbol{U}}_{t_0} \tag{3.56}$$

$$\bar{\boldsymbol{f}}_f = \int_\Omega n \rho_f \left(\boldsymbol{N}^u\right)^T \boldsymbol{b} d\Omega - \int_{\Gamma_p} n \tilde{p} \left(\boldsymbol{N}^u\right)^T \boldsymbol{n} d\Gamma_p \tag{3.57}$$

The vector $\boldsymbol{n}$ in the terms involving the boundary with prescribed pressure is the outwards normal vector of the boundary. Further in this formulation, the traction boundary condition is expressed in terms of effective Biot stresses $\tilde{\boldsymbol{t}}''$.

A more condensed form of the three equations can be written as

$$\boldsymbol{M} \ddot{\bar{\boldsymbol{\Phi}}} + \boldsymbol{C} \dot{\bar{\boldsymbol{\Phi}}} + \boldsymbol{K} \bar{\boldsymbol{\Phi}} + \boldsymbol{L}\left(\bar{\boldsymbol{\Phi}}\right) = \boldsymbol{F} \tag{3.58}$$

where

$$\boldsymbol{M} = \begin{bmatrix} \boldsymbol{M_s} & \boldsymbol{0} & \boldsymbol{0} \\ \boldsymbol{0} & \boldsymbol{0} & \boldsymbol{0} \\ \boldsymbol{0} & \boldsymbol{0} & \boldsymbol{M_f} \end{bmatrix} \quad \boldsymbol{C} = \begin{bmatrix} \boldsymbol{C}_1 & \boldsymbol{0} & -\boldsymbol{C}_2 \\ \boldsymbol{0} & \boldsymbol{0} & \boldsymbol{0} \\ -\boldsymbol{C}_2^T & \boldsymbol{0} & \boldsymbol{C}_3 \end{bmatrix} \quad \boldsymbol{K} = \begin{bmatrix} \boldsymbol{0} & -\boldsymbol{G}_1 & \boldsymbol{0} \\ -\boldsymbol{G}_1^T & -\boldsymbol{P} & -\boldsymbol{G}_2^T \\ \boldsymbol{0} & -\boldsymbol{G}_2 & \boldsymbol{0} \end{bmatrix}$$

$$\bar{\boldsymbol{\Phi}} = \begin{bmatrix} \bar{\boldsymbol{u}} \\ \bar{\boldsymbol{p}} \\ \bar{\boldsymbol{U}} \end{bmatrix} \qquad \boldsymbol{L}\left(\bar{\boldsymbol{\Phi}}\right) = \begin{bmatrix} \int_\Omega \boldsymbol{B}^T \boldsymbol{\sigma}'' d\Omega \\ \boldsymbol{0} \\ \boldsymbol{0} \end{bmatrix} \qquad \boldsymbol{F} = \begin{bmatrix} \bar{\boldsymbol{f}}_s \\ \bar{\boldsymbol{f}}_{p0} \\ \bar{\boldsymbol{f}}_f \end{bmatrix} \tag{3.59}$$

which have to be fulfilled at all times. In this regard, $\boldsymbol{M}$, $\boldsymbol{C}$ and $\boldsymbol{K}$ are assumed constant throughout the simulation.

(3.58) and (3.59) reveal a couple of interesting things of the $u - p - U$ formulation. First of all, in the case where the fluid is left out of the equation system, it simply reduces to the one governing solid mechanics. Further, damping is naturally occurring in the model due to the permeability of the material and does not need to be included using e.g. Rayleigh damping.

In order to simplify the interpolation of (3.39) and (3.42) and the spatial integration of (3.46)-(3.57), the domain is subdivided, or meshed, into elements, which each account for part of the domain according to their connection to the domain nodes. Countless different element formulations exist, which differ in connectivity, shape, interpolation, and integration procedures. Commonly encountered elements in 2D analysis include triangular and quadrilateral elements, while tetrahedral and brick elements are common in 3D analysis. The field approximation is typically polynomial of first or second order, and the domain integration of (3.46)-(3.57) is carried out using gauss quadrature or similar approximations to minimize computational effort. By decreasing the element size, the approximate interpolation becomes more and more accurate, and the obtained solution should hence approach the exact one.

3.3.3 Discretization in time

In order to account for the dynamics of the system, a time integration scheme has to be utilized. Many different schemes are available, see e.g. Crisfield (2000) and Cook et al. (2002). Here focus will be on the classical Newmark scheme, which is a specific case of the more general beta-*m* method (Katona and Zienkiewicz, 1985).

At some initial time, t_0, all the quantities of $\bar{\boldsymbol{\Phi}}$, denoted $\bar{\boldsymbol{\Phi}}_{t_0}$, and their time derivatives together with $\boldsymbol{\sigma}''_{t_0}$ and $\boldsymbol{F}_{t_0}$, denoting the effective stresses and load vector at time t_0, are known and fulfill the relationship of (3.58). In order to find the solution at a later time $t_1 = t_0 + \Delta t$, a Taylor series expansion of the time derivatives of $\bar{\boldsymbol{\Phi}}$ around t_0 is carried out, which is exact to the term involving the acceleration. Any remaining terms are approximated by a scalar multiplication of an incremental change in $\ddot{\bar{\boldsymbol{\Phi}}}$. The result is

$$\begin{aligned}
\ddot{\bar{\boldsymbol{\Phi}}}_{t_1} &= \ddot{\bar{\boldsymbol{\Phi}}}_{t_0} + \Delta\ddot{\bar{\boldsymbol{\Phi}}} = \boldsymbol{q}_2 + \Delta\ddot{\bar{\boldsymbol{\Phi}}} \\
\dot{\bar{\boldsymbol{\Phi}}}_{t_1} &= \dot{\bar{\boldsymbol{\Phi}}}_{t_0} + \ddot{\bar{\boldsymbol{\Phi}}}_{t_0}\Delta t + \beta_1\Delta t\Delta\ddot{\bar{\boldsymbol{\Phi}}} = \boldsymbol{q}_1 + \beta_1\Delta t\Delta\ddot{\bar{\boldsymbol{\Phi}}} \\
\bar{\boldsymbol{\Phi}}_{t_1} &= \bar{\boldsymbol{\Phi}}_{t_0} + \Delta t\dot{\bar{\boldsymbol{\Phi}}}_{t_0} + \frac{\Delta t^2}{2}\ddot{\bar{\boldsymbol{\Phi}}}_{t_0} + \beta_0\frac{\Delta t^2}{2}\Delta\ddot{\bar{\boldsymbol{\Phi}}} = \boldsymbol{q}_0 + \beta_0\frac{\Delta t^2}{2}\Delta\ddot{\bar{\boldsymbol{\Phi}}}
\end{aligned} \tag{3.60}$$

where $\boldsymbol{q}_0$, $\boldsymbol{q}_1$, and $\boldsymbol{q}_2$ have been introduced for readability and can be calculated based on the known values at time t_0. In this regard, the subscript refers to the order of the time derivative.

Further, β_0 and β_1 are the parameters of the integration scheme and are related to the classical Newmark parameters β and γ by

$$\beta_0 = 2\beta \qquad \text{and} \qquad \beta_1 = \gamma \tag{3.61}$$

$\beta_0 = 0$ and $\beta_1 = 0$ implies a fully explicit integration scheme, while $\beta_0 = 1$ and $\beta_1 = 1$ implies a fully implicit integration scheme.

Since (3.58) is non-linear due to the material behavior, a residual, $\boldsymbol{R}$, is set up incorporating (3.60) giving

$$\boldsymbol{R} = \boldsymbol{M}\left(\boldsymbol{q}_2 + \Delta\ddot{\bar{\boldsymbol{\Phi}}}\right) + \boldsymbol{C}\left(\boldsymbol{q}_1 + \beta_1 \Delta t \Delta\ddot{\bar{\boldsymbol{\Phi}}}\right) + \boldsymbol{K}\left(\boldsymbol{q}_0 + \beta_0 \frac{\Delta t^2}{2}\Delta\ddot{\bar{\boldsymbol{\Phi}}}\right) + \boldsymbol{L}_{t_1} - \boldsymbol{F}_{t_1} = \boldsymbol{0} \quad (3.62)$$

where the non-zero term of $\boldsymbol{L}_{t_1}$ is given by

$$\int_\Omega \boldsymbol{B}^T \boldsymbol{\sigma}''_{t_1} d\Omega = \int_\Omega \boldsymbol{B}^T \boldsymbol{\sigma}''_{t_0} d\Omega + \int_\Omega \boldsymbol{B}^T \Delta\boldsymbol{\sigma}'' d\Omega \quad (3.63)$$

and $\Delta\boldsymbol{\sigma}''$ has been found through proper integration of

$$\Delta\boldsymbol{\sigma}'' = \int_{t_0}^{t_1} \boldsymbol{D}^{ep} d\boldsymbol{\varepsilon} \quad (3.64)$$

which is material dependent and will be described more thoroughly in the next chapter. Further, $\boldsymbol{F}_{t_1}$ is the known load vector at time t_1. (3.62) can be solved through a Newton-Raphson solution procedure where the i'th guess, $\Delta\ddot{\bar{\boldsymbol{\Phi}}}_i$, of $\Delta\ddot{\bar{\boldsymbol{\Phi}}}$ is affiliated with a residual $\boldsymbol{R}_i$. By applying a truncated Taylor series expansion of first order on the residual $\boldsymbol{R}$ around $\Delta\ddot{\bar{\boldsymbol{\Phi}}}_i$ and equating it to zero, an improved guess $\Delta\ddot{\bar{\boldsymbol{\Phi}}}_{i+1}$ can be found through

$$\Delta\ddot{\bar{\boldsymbol{\Phi}}}_{i+1} = \Delta\ddot{\bar{\boldsymbol{\Phi}}}_i + d\Delta\ddot{\bar{\boldsymbol{\Phi}}} \quad (3.65)$$

where

$$d\Delta\ddot{\bar{\boldsymbol{\Phi}}} = \left(\frac{\partial \boldsymbol{R}}{\partial \Delta\ddot{\bar{\boldsymbol{\Phi}}}}\right)^{-1} (-\boldsymbol{R}_i) \quad (3.66)$$

The gradient matrix of $\boldsymbol{R}$ can be found to be

$$\frac{\partial \boldsymbol{R}}{\partial \Delta\ddot{\bar{\boldsymbol{\Phi}}}} = \boldsymbol{M} + \beta_1 \Delta t \boldsymbol{C} + \beta_0 \frac{\Delta t^2}{2}\left(\boldsymbol{K} + \begin{bmatrix} \boldsymbol{K}_t & \boldsymbol{0} & \boldsymbol{0} \\ \boldsymbol{0} & \boldsymbol{0} & \boldsymbol{0} \\ \boldsymbol{0} & \boldsymbol{0} & \boldsymbol{0} \end{bmatrix}\right) \quad (3.67)$$

since the partial derivative of $\boldsymbol{L}$ is given by

$$\frac{\partial \boldsymbol{L}}{\partial \Delta\ddot{\bar{\boldsymbol{\Phi}}}} = \begin{bmatrix} \frac{\partial \int_\Omega \boldsymbol{B}^T \boldsymbol{\sigma}'' d\Omega}{\partial \Delta\ddot{\bar{\boldsymbol{\Phi}}}} \\ \boldsymbol{0} \\ \boldsymbol{0} \end{bmatrix} \quad (3.68)$$

and usage of the chain rule yields

$$\frac{\partial \int_\Omega \boldsymbol{B}^T \boldsymbol{\sigma}'' d\Omega}{\partial \Delta\ddot{\bar{\boldsymbol{\Phi}}}} = \int_\Omega \boldsymbol{B}^T \frac{\partial \Delta\boldsymbol{\sigma}''}{\partial \Delta\boldsymbol{\varepsilon}} \frac{\partial \Delta\boldsymbol{\varepsilon}}{\partial \Delta\bar{\boldsymbol{\Phi}}} \frac{\partial \Delta\bar{\boldsymbol{\Phi}}}{\partial \Delta\ddot{\bar{\boldsymbol{\Phi}}}} d\Omega =$$
$$\int_\Omega \boldsymbol{B}^T \boldsymbol{D}^{epc} \begin{bmatrix} \boldsymbol{B} & \boldsymbol{0} & \boldsymbol{0} \end{bmatrix} \beta_0 \frac{\Delta t^2}{2} \begin{bmatrix} \boldsymbol{I} & \boldsymbol{0} & \boldsymbol{0} \\ \boldsymbol{0} & \boldsymbol{I} & \boldsymbol{0} \\ \boldsymbol{0} & \boldsymbol{0} & \boldsymbol{I} \end{bmatrix} d\Omega = \beta_0 \frac{\Delta t^2}{2} \begin{bmatrix} \boldsymbol{K}_t & \boldsymbol{0} & \boldsymbol{0} \end{bmatrix} \quad (3.69)$$

where $\boldsymbol{K}_t$ and $\boldsymbol{D}^{epc}$ are defined by

$$\boldsymbol{K}_t = \int_\Omega \boldsymbol{B}^T \boldsymbol{D}^{epc} \boldsymbol{B} d\Omega \qquad \text{and} \qquad \boldsymbol{D}^{epc} = \frac{\partial \Delta \boldsymbol{\sigma}''}{\partial \Delta \boldsymbol{\varepsilon}} \tag{3.70}$$

The above Newton-Raphson scheme is then continued until

$$||\boldsymbol{R}_i|| < \epsilon \tag{3.71}$$

where $||\boldsymbol{R}_i||$ designates the Euclidean norm of $\boldsymbol{R}_i$ and ϵ is some predefined tolerance usually expressed by some fraction, ζ, of the Euclidean norm of the applied forces

$$\epsilon = \zeta ||\boldsymbol{F}_{t_1}|| \tag{3.72}$$

The derivations of this chapter account for the dynamic soil-fluid interaction. However as shown, the interaction is dependent upon the intricate constitutive behavior of the solid skeleton given by (3.16), which needs to be accounted for. This is explained in more detail in the following chapter.

Chapter 4

Constitutive modeling of solid skeleton

This chapter will describe the fundamentals of elasto-plastic constitutive modeling. Firstly, the general framework of multisurface elasto-plasticity will be introduced followed by the numerical treatment of the integration of the constitutive relationship.

4.1 Multisurface elasto-plasticity

The framework of multisurface elasto-plasticity is a general framework used to account for the intricate relationship between strains and stresses within a continuous material. Based on a couple of abstractions explained in the following, it is capable of modeling many materials on a scale relevant for engineering practices.

4.1.1 Strain definitions

As mentioned in section 2.2, the deformation, $\boldsymbol{\varepsilon}$, of the skeleton is primarily linked to the load carried by the skeleton given by the effective stresses, $\boldsymbol{\sigma}''$, and consists of both reversible and irreversible deformations, as shown on Figure 4.1a. Based on this, the strains are divided into an elastic and plastic part

$$\boldsymbol{\varepsilon} = \boldsymbol{\varepsilon}^e + \boldsymbol{\varepsilon}^p \tag{4.1}$$

The elastic part, $\boldsymbol{\varepsilon}^e$, constitutes the reversible strains while the plastic part, $\boldsymbol{\varepsilon}^p$, constitutes the permanent strains. Further, Figure 4.1b shows that when plastic strains have developed, the one-to-one relationship between strains

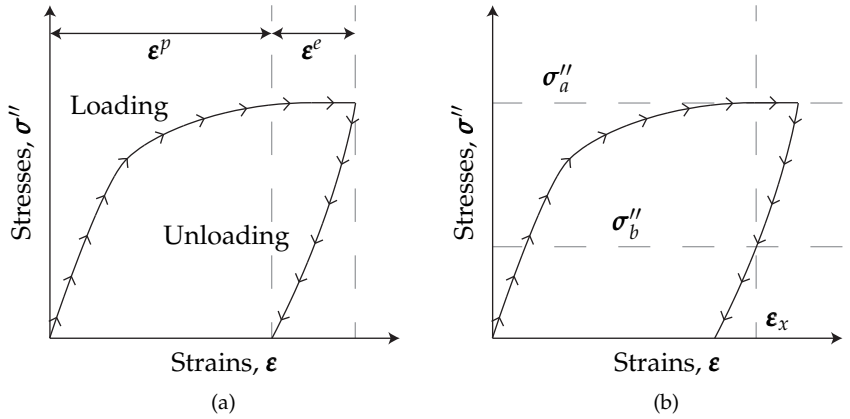

Figure 4.1: Loading and unloading of solid skeleton. (a) Definition of reversible and irreversible strains, $\boldsymbol{\varepsilon}^e$ and $\boldsymbol{\varepsilon}^p$. (b) One-to-one relationship between strains and stresses is lost once plastic strains develop.

and stresses is permanently lost, which calls for an incremental based approach.

By definition, the stresses within the skeleton are caused exclusively by elastic strains through the constitutive relation

$$\dot{\boldsymbol{\sigma}}'' = \boldsymbol{D}\dot{\boldsymbol{\varepsilon}}^e = \boldsymbol{D}\left(\dot{\boldsymbol{\varepsilon}} - \dot{\boldsymbol{\varepsilon}}^p\right) \tag{4.2}$$

where $\boldsymbol{D}$ denotes the constitutive matrix, which in the general non-linear case could be dependent upon e.g. the current strain state. However, in the linear-elastic case, which will be assumed here, it is constant. The constitutive matrix can further be subdivided into a part related to the normal components, $\bar{\boldsymbol{D}}$, and a part related to the shear components, $\tilde{\boldsymbol{G}}$ according to

$$\boldsymbol{D} = \begin{bmatrix} \bar{\boldsymbol{D}} & \boldsymbol{0} \\ \boldsymbol{0} & \tilde{\boldsymbol{G}} \end{bmatrix} \tag{4.3}$$

where

$$\bar{\boldsymbol{D}} = \frac{E}{(1+\nu)(1-2\nu)} \begin{bmatrix} 1-\nu & \nu & \nu \\ \nu & 1-\nu & \nu \\ \nu & \nu & 1-\nu \end{bmatrix}, \quad \tilde{\boldsymbol{G}} = \frac{E}{2(1+\nu)} \begin{bmatrix} 1 & 0 & 0 \\ 0 & 1 & 0 \\ 0 & 0 & 1 \end{bmatrix} \tag{4.4}$$

where E denotes Young's modulus and ν denotes Poisson's ratio.

4.1.2 Evolution law

As was also discussed in section 2.2, the characteristics of the skeleton, such as its strength or deformation behavior, can be altered due to plastic straining.

This alteration is tracked through a set of material dependent hardening parameters, $\boldsymbol{K}$, which are used in e.g. the yield functions and plastic potentials discussed in the following sections.

The hardening parameters are usually related to some state parameters, $\boldsymbol{\kappa}$,

$$\boldsymbol{K} = \boldsymbol{K}(\boldsymbol{\kappa}) \tag{4.5}$$

which express the internal state of the material. These state parameters need to be identified along with their time rate of change, which is usually dependent upon the current stress state and hardening parameters

$$\dot{\boldsymbol{\kappa}} = \dot{\boldsymbol{\kappa}}(\boldsymbol{\sigma}'', \boldsymbol{K}) \tag{4.6}$$

which is denoted the evolution law. Commonly used parameters for the state parameters include the accumulated plastic strain, denoted $\bar{\varepsilon}^p$, defined by

$$\kappa = \bar{\varepsilon}^p = \int_0^t \sqrt{\frac{2}{3}(\dot{\boldsymbol{\varepsilon}}^p)^T \dot{\boldsymbol{\varepsilon}}^p} dt \tag{4.7}$$

or the dissipated plastic work, W^p,

$$\kappa = W^p = \int_0^t \boldsymbol{\sigma}'' \dot{\boldsymbol{\varepsilon}}^p dt \tag{4.8}$$

Alternatively, the state parameters can also be defined by one or more potentials, j_i, which are functionals of stress and hardening parameters

$$j_i = j_i(\boldsymbol{\sigma}'', \boldsymbol{K}) \qquad \text{where} \qquad i = 1, \ldots, n \tag{4.9}$$

where n in this context denotes the number of potential functions. Using these potential functions, the evolution of the state parameters can be expressed as

$$\dot{\boldsymbol{\kappa}} = -\sum_{i=1}^{n} \dot{\lambda}_i \left(\frac{\partial j_i}{\partial \boldsymbol{K}} \right)^T \tag{4.10}$$

where $\dot{\lambda}_i$ are some non-zero scalar scaling quantities. In the case of perfect plasticity, the evolution law can simply be taken as $\dot{\kappa} = 0$, resulting in no change in $\boldsymbol{K}$, c.f. (4.5).

4.1.3 Yield criteria

The strength and onset of plastic straining is governed by one or more invariant yield functions, f_i, which are smooth continuous functionals of the stress state, $\boldsymbol{\sigma}''$, and the hardening parameters, $\boldsymbol{K}$,

$$f_i = f_i(\boldsymbol{\sigma}'', \boldsymbol{K}) \qquad \text{where} \qquad i = 1, \ldots, n \tag{4.11}$$

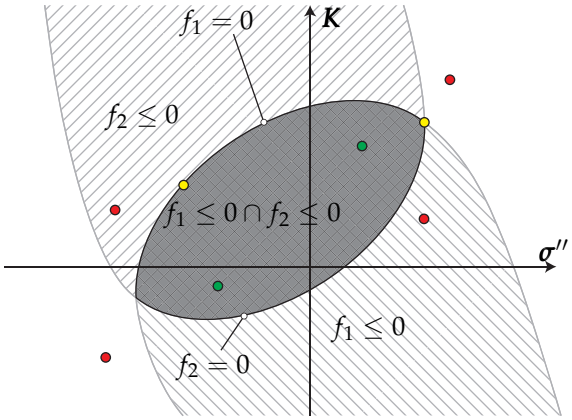

Figure 4.2: Sketch of two yield functions, f_1 and f_2, shown in $\boldsymbol{\sigma}'' - \boldsymbol{K}$ space. The hatched regions show the elastic states defined by (4.12) for f_1 and f_2 respectively. The gray region shows the combined elastic region, given by the intersection of (4.15). Any state outside the gray region is inadmissible cf. (4.14). The boundary shown in black defines the yield surface and is partly made up of (4.13) for f_1 and f_2. Green points indicate an elastic combination of $\boldsymbol{\sigma}''$ and $\boldsymbol{K}$, yellow points indicate a combination involving plastic strains while red points are inadmissible.

Each yield function imposes restrictions on the set of effective stresses, $\boldsymbol{\sigma}''$, and hardening parameters, $\boldsymbol{K}$, that can be obtained in the skeleton. Each function defines an elastic set of states defined by

$$f_i\left(\boldsymbol{\sigma}'', \boldsymbol{K}\right) < 0 \tag{4.12}$$

which does not warrant any additional plastic straining, along with a yield criterion

$$f_i\left(\boldsymbol{\sigma}'', \boldsymbol{K}\right) = 0 \tag{4.13}$$

which indicates the set of $\boldsymbol{\sigma}'' - \boldsymbol{K}$ that results in plastic straining. Finally, each yield function restricts the possible set of $\boldsymbol{\sigma}'' - \boldsymbol{K}$, by defining a set of states that can not be obtained within the skeleton defined by

$$f_i\left(\boldsymbol{\sigma}'', \boldsymbol{K}\right) > 0 \tag{4.14}$$

By consideration of all yield functions, see Figure 4.2, a region of elastic stress states can be defined by the intersection of (4.12)

$$\bigcap_{i=1}^{n} f_i\left(\boldsymbol{\sigma}'', \boldsymbol{K}\right) < 0 \tag{4.15}$$

along with a region of inadmissible states defined by the union of (4.14)

$$\bigcup_{i=1}^{n} f_i\left(\boldsymbol{\sigma}'', \boldsymbol{K}\right) > 0 \tag{4.16}$$

For a particular choice of $\boldsymbol{K}$, the boundary between these two regions is a piecewise smooth convex surface in stress space constructed from the relevant yield criteria, (4.13). This surface is known as the yield surface since stress states on this surface are responsible for plastic straining. As is implied by Figure 4.2, the yield surface can contain discontinuities associated with the intersection of two or more yield criteria. A state located on such a discontinuity thus fulfills more than one yield criterion. The yield criteria, which are fulfilled, are called active while the remaining yield criteria are called inactive.

Since plastic straining only occurs when one or more yield criteria are fulfilled, continuous plastic straining requires that $\dot{f}_i = 0$ is imposed on all active yield criteria. Based on (4.11) and the chain rule, this results in

$$\dot{f}_i = \frac{\partial f_i}{\partial \boldsymbol{\sigma}''} \dot{\boldsymbol{\sigma}}'' + \frac{\partial f_i}{\partial \boldsymbol{K}} \dot{\boldsymbol{K}} = 0 \tag{4.17}$$

which is known as the consistency condition.

4.1.4 Plastic potentials

In order to evaluate (4.2), it is not only necessary to establish whether plastic strains evolve or not. Knowledge about the direction and magnitude of the plastic strains is also needed. In order to account for this, the plastic strains are defined through one or more potentials

$$g_i = g_i\left(\boldsymbol{\sigma}'', \boldsymbol{K}\right) \qquad \text{where} \qquad i = 1, \ \ldots, \ n \tag{4.18}$$

known as plastic potentials. Based on these potentials, the plastic strains are by definition assumed to be given by

$$\dot{\boldsymbol{\varepsilon}}^p = \sum_{i=1}^{n} \dot{\lambda}_i \left(\frac{\partial g_i}{\partial \boldsymbol{\sigma}''} \right)^T \tag{4.19}$$

where the scalars $\dot{\lambda}_i$ are identical to those present in (4.10). Due to their role in determining the plastic strains, $\dot{\lambda}_i$ have been dubbed plastic multipliers.

(4.19) effectively gives the plastic strains as a linear combination of the directions given by the derivatives of the plastic potentials with regards to effective stresses and was first proposed by Koiter (1953). Two restrictions apply however. It is assumed that only the active yield criteria contribute to the plastic strains, resulting in the fact that $\dot{\lambda}_i = 0$ for any inactive criteria, where $f_i < 0$. The other restriction is that $\dot{\lambda}_i$ must be non-negative for all yield criteria. Combined with (4.13), these restrictions can be states as

$$f_i \leq 0 \qquad \dot{\lambda}_i \geq 0 \qquad \dot{\lambda}_i f_i = 0 \tag{4.20}$$

for all i.

The plastic potentials need to be defined in such a way that they properly account for plastic volumetric and shear strains, such as those illustrated on Figure 2.6. If the plastic potentials are chosen such that $g_i = f_i$, it is referred to as associated plasticity, while for $g_i \neq f_i$, the term non-associated plasticity is used.

4.1.5 Elasto-plastic infinitesimal constitutive matrix

The infinitesimal constitutive matrix, $\boldsymbol{D}^{ep}$, introduced in (3.16) relates infinitesimal total strain increments with infinitesimal effective stress increments. In the case where none of the yield criteria are active, and thus no plastic straining occurs, $\boldsymbol{D}^{ep}$ simply amounts to $\boldsymbol{D}$ cf. (4.2).

However, when plastic straining does occur, it is necessary to find the appertaining rates of the plastic multipliers in order to assess $\boldsymbol{D}^{ep}$.

If for example the evolution law is given as (4.10), D^{ep} can be found as shown in the following. Substitution of (4.19) into (4.2) results in

$$\dot{\boldsymbol{\sigma}}'' = \boldsymbol{D}\dot{\boldsymbol{\varepsilon}} - \boldsymbol{D}\sum_{i=1}^{n} \dot{\lambda}_i \left(\frac{\partial g_i}{\partial \boldsymbol{\sigma}''}\right)^T \tag{4.21}$$

In the case where all yield criteria are active, the unknowns of $\dot{\lambda}_i$ can be established by invoking the consistency condition (4.17) on all yield criteria and substituting $\dot{\boldsymbol{\sigma}}''$ with the expression given by (4.21). This results in

$$\dot{f}_i = \frac{\partial f_i}{\partial \boldsymbol{\sigma}''}\boldsymbol{D}\dot{\boldsymbol{\varepsilon}} - \frac{\partial f_i}{\partial \boldsymbol{\sigma}''}\boldsymbol{D}\sum_{j=1}^{n} \dot{\lambda}_j \left(\frac{\partial g_j}{\partial \boldsymbol{\sigma}''}\right)^T + \frac{\partial f_i}{\partial \boldsymbol{K}}\frac{\partial \boldsymbol{K}}{\partial \boldsymbol{\kappa}}\sum_{j=1}^{n}\left(-\dot{\lambda}_j \left(\frac{\partial j_j}{\partial \boldsymbol{K}}\right)^T\right) = 0 \tag{4.22}$$

which can be written as

$$\begin{bmatrix} \frac{\partial f_1}{\partial \boldsymbol{\sigma}''}\boldsymbol{D}\dot{\boldsymbol{\varepsilon}} \\ \vdots \\ \frac{\partial f_n}{\partial \boldsymbol{\sigma}''}\boldsymbol{D}\dot{\boldsymbol{\varepsilon}} \end{bmatrix} - \boldsymbol{A}\begin{bmatrix} \dot{\lambda}_1 \\ \vdots \\ \dot{\lambda}_n \end{bmatrix} = 0 \tag{4.23}$$

where the entries in matrix $\boldsymbol{A}$ is given by

$$A_{ij} = \frac{\partial f_i}{\partial \boldsymbol{\sigma}''}\boldsymbol{D}\left(\frac{\partial g_j}{\partial \boldsymbol{\sigma}''}\right)^T + \frac{\partial f_i}{\boldsymbol{K}}\frac{\partial \boldsymbol{K}}{\partial \boldsymbol{\kappa}}\left(\frac{\partial j_j}{\partial \boldsymbol{K}}\right)^T \tag{4.24}$$

(4.23) can be solved for the unknown $\dot{\lambda}_i$ such that

$$\begin{bmatrix} \dot{\lambda}_1 \\ \vdots \\ \dot{\lambda}_n \end{bmatrix} = \boldsymbol{B} \begin{bmatrix} \frac{\partial f_1}{\partial \boldsymbol{\sigma}''} \boldsymbol{D}\dot{\boldsymbol{\varepsilon}} \\ \vdots \\ \frac{\partial f_n}{\partial \boldsymbol{\sigma}''} \boldsymbol{D}\dot{\boldsymbol{\varepsilon}} \end{bmatrix} \tag{4.25}$$

where

$$\boldsymbol{B} = \boldsymbol{A}^{-1} \tag{4.26}$$

Replacing the now known quantities back into (4.21) gives

$$\dot{\boldsymbol{\sigma}}'' = \boldsymbol{D}\dot{\boldsymbol{\varepsilon}} - \boldsymbol{D} \sum_{i=1}^{n} \sum_{j=1}^{n} B_{ij} \frac{\partial f_j}{\partial \boldsymbol{\sigma}''} \boldsymbol{D}\dot{\boldsymbol{\varepsilon}} \left(\frac{\partial g_i}{\partial \boldsymbol{\sigma}''} \right)^T \tag{4.27}$$

and finally $\boldsymbol{D}^{ep}$ can be identified as

$$\boldsymbol{D}^{ep} = \boldsymbol{D} - \boldsymbol{D} \sum_{i=1}^{n} \sum_{j=1}^{n} B_{ij} \left(\frac{\partial g_i}{\partial \boldsymbol{\sigma}''} \right)^T \frac{\partial f_j}{\partial \boldsymbol{\sigma}''} \boldsymbol{D} \tag{4.28}$$

In the general case where only some of the yield criteria are active, only the consistency conditions of the active criteria must hold. The equation system of (4.23) is modified by exchanging the consistency conditions with a trivial equation of $\dot{\lambda} = 0$ for the relevant criteria. This can be done by modifying $\boldsymbol{A}$ such that

$$A_{ij} = \alpha_i \alpha_j \left(\frac{\partial f_i}{\partial \boldsymbol{\sigma}''} \boldsymbol{D} \left(\frac{\partial g_j}{\partial \boldsymbol{\sigma}''} \right)^T + \frac{\partial f_i}{\boldsymbol{K}} \frac{\partial \boldsymbol{K}}{\partial \boldsymbol{\kappa}} \left(\frac{\partial j_j}{\partial \boldsymbol{K}} \right)^T \right) + (\alpha_i - 1)(\alpha_j - 1) \tag{4.29}$$

where α_i in this context is used to identify active yield criteria, i.e.

$$\alpha_i = \begin{cases} 0 & \text{if } f_i < 0 \\ 1 & \text{if } f_i = 0 \end{cases} \tag{4.30}$$

Finally, modifying (4.28) accordingly results in

$$\boldsymbol{D}^{ep} = \boldsymbol{D} - \boldsymbol{D} \sum_{i=1}^{n} \sum_{j=1}^{n} \alpha_i \alpha_j B_{ij} \left(\frac{\partial g_i}{\partial \boldsymbol{\sigma}''} \right)^T \frac{\partial f_j}{\partial \boldsymbol{\sigma}''} \boldsymbol{D} \tag{4.31}$$

which is applicable for all combinations of active yield criteria.

Since the choice of evolution law affected the above derivations, generally another form of the infinitesimal constitutive matrix would be obtained if another evolution law than (4.10) is chosen.

4.2 Return mapping

With the derivation of the infinitesimal constitutive matrix of (4.31), the time integration of the constitutive relation, (3.64), required by the finite element procedure can be carried out using any method applicable for initial value ordinary differential equations. Due to the complexity, analytical solutions are rarely available and numerical approximation must be used. Since the constitutive integration has to be carried out in all locations associated with the spatial integration of (3.58), the numerical procedure is often further approximated using the framework of return mapping, which will be discussed in the following.

4.2.1 Fundamentals

The basic concept of return mapping is to initially assume that the strain increment, $\Delta\boldsymbol{\varepsilon}$, established in the time integration from time t_0 to t_1 is entirely elastic. With the use of (4.2), the integration of (3.64) in the linear-elastic case leads to the effective stress increment

$$\Delta\boldsymbol{\sigma}''_{trial} = \int_{t_0}^{t_1} \boldsymbol{D}^{ep} d\boldsymbol{\varepsilon} = \boldsymbol{D}\Delta\boldsymbol{\varepsilon} \tag{4.32}$$

which is known as the elastic predictor stress increment. By adding this prediction to the initial stress state, $\boldsymbol{\sigma}''_{t_0}$, a trial stress state given by

$$\boldsymbol{\sigma}''_{trial} = \boldsymbol{\sigma}''_{t_0} + \Delta\boldsymbol{\sigma}''_{trial} \tag{4.33}$$

is obtained. Further, since the increment is assumed entirely elastic, no changes in the internal state of the material are expected

$$\boldsymbol{\kappa}_{trial} = \boldsymbol{\kappa}_{t_0} \tag{4.34}$$

and hence no change in the hardening parameters, resulting in

$$\boldsymbol{K}_{trial} = \boldsymbol{K}_{t_0} \tag{4.35}$$

c.f. (4.5). Based on this trial set of $\boldsymbol{\sigma}''$ and $\boldsymbol{K}$, the yield functions are evaluated. If all yield functions obey (4.12), then the assumption of an entirely elastic strain increment is deemed valid and it follows that

$$\Delta\boldsymbol{\sigma}'' = \Delta\boldsymbol{\sigma}''_{trial} \qquad \text{and} \qquad \boldsymbol{\kappa}_{t_1} = \boldsymbol{\kappa}_{trial} \tag{4.36}$$

However, if any of the yield functions result in a positive value, as shown in Figure 4.3, a part of the strain increment must originate from plastic strains. In that case, integration of (3.64) gives

$$\Delta\boldsymbol{\sigma}'' = \int_{t_0}^{t_1} \boldsymbol{D}^{ep} d\boldsymbol{\varepsilon} = \boldsymbol{D}\Delta\boldsymbol{\varepsilon} - \boldsymbol{D}\Delta\boldsymbol{\varepsilon}^p = \Delta\boldsymbol{\sigma}''_{trial} - \boldsymbol{D}\Delta\boldsymbol{\varepsilon}^p \tag{4.37}$$

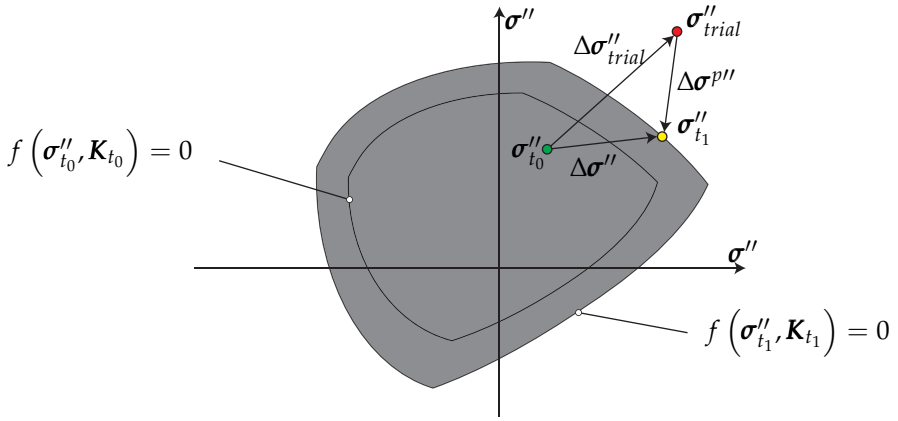

Figure 4.3: Sketch of return mapping for a predicted stress state, $\boldsymbol{\sigma}''_{trial}$, lying outside the yield surface shown in gray.

.

and as shown on Figure 4.3 the final stress state can be written as

$$\boldsymbol{\sigma}''_{t_1} = \boldsymbol{\sigma}''_{trial} - \Delta\boldsymbol{\sigma}^{p''} \tag{4.38}$$

where

$$\Delta\boldsymbol{\sigma}^{p''} = \boldsymbol{D}\Delta\boldsymbol{\varepsilon}^{p} \tag{4.39}$$

is known as the plastic corrector increment. However, since the integration of the plastic strains is the actual challenge of the problem, an approximation is applied based on the plastic strain definition of (4.19), giving

$$\Delta\boldsymbol{\varepsilon}^{p} = \sum_{i=1}^{n} \int_{t_0}^{t_1} \dot{\lambda}_i \left(\frac{\partial g_i}{\partial \boldsymbol{\sigma}''}\right)^T dt \approx \sum_{i=1}^{n} \Delta\lambda_i \left(\frac{\partial g_i}{\partial \boldsymbol{\sigma}''}\right)^T \Bigg|_{\tau} \tag{4.40}$$

where $t_0 \leq \tau \leq t_1$ is an intermediate time station, which is t_0 for an explicit scheme and t_1 for an implicit scheme. A similar approximation is applied to the internal state parameters, which is consistent with their chosen definitions. If e.g. the potential definition of (4.10) is used, the approximation would become

$$\Delta\boldsymbol{\kappa} = -\sum_{i=1}^{n} \int_{t_0}^{t_1} \dot{\lambda}_i \left(\frac{\partial j_i}{\partial \boldsymbol{K}}\right)^T dt \approx \sum_{i=1}^{n} \Delta\lambda i \left(\frac{\partial j_i}{\partial \boldsymbol{K}}\right)^T \Bigg|_{\tau} \tag{4.41}$$

whereas if the accumulated plastic strain, (4.7), is chosen as a state parameter, the approximation would be

$$\Delta\bar{\varepsilon}^{p} = \int_{t_0}^{t_1} \sqrt{\frac{2}{3}\left(\dot{\boldsymbol{\varepsilon}}^{p}\right)^T \dot{\boldsymbol{\varepsilon}}^{p}}\, dt \approx \sqrt{\frac{2}{3}\left(\Delta\boldsymbol{\varepsilon}^{p}\right)^T \Delta\boldsymbol{\varepsilon}^{p}} \tag{4.42}$$

where $\Delta\boldsymbol{\varepsilon}^p$ is the approximation given by (4.40). It then follows that

$$\boldsymbol{\kappa}_{t_1} = \boldsymbol{\kappa}_{t_0} + \Delta\boldsymbol{\kappa} \tag{4.43}$$

and thus, the updated hardening parameters can be established

$$\boldsymbol{K}_{t_1} = \boldsymbol{K}\left(\boldsymbol{\kappa}_{t_1}\right) \tag{4.44}$$

Based on these approximations, the task is to find a suitable set of $\boldsymbol{\sigma}''_{t_1}$, $\boldsymbol{\kappa}_{t_1}$ and $\Delta\lambda_i$ which fulfill the requirements of (4.38) and (4.43) under the constraints of

$$f_i\left(\boldsymbol{\sigma}''_{t_1}, \boldsymbol{K}_{t_1}\right) \leq 0 \qquad \Delta\lambda_i \geq 0 \qquad \Delta\lambda_i f_i\left(\boldsymbol{\sigma}''_{t_1}, \boldsymbol{K}_{t_1}\right) = 0 \tag{4.45}$$

for all i. Depending on the yield functions, plastic potentials and evolution laws, this equation system can be non-linear and is often solved through a Newton-Raphson solution procedure, which is specifically tailored to the characteristics of the problem in order to be computationally efficient.

4.2.2 Consistent constitutive matrix

As stated in (3.70), the global equilibrium iterations of the finite element model require the determination of

$$\boldsymbol{D}^{epc} = \frac{\partial\Delta\boldsymbol{\sigma}''}{\partial\Delta\boldsymbol{\varepsilon}} \tag{4.46}$$

which is dubbed the consistent constitutive matrix. This is due to the fact that it is tempting to use the infinitesimal constitutive matrix of section 4.1.5 instead; however, in doing so the quadratic convergence of the solution will be lost (Nagtegaal, 1982; Simo and Taylor, 1985). Thus, $\boldsymbol{D}^{epc}$ is an essential part of the material model. Since $\Delta\boldsymbol{\sigma}''$ is often defined implicit through a non-linear set of equations, the consistent constitutive matrix must be found by implicit differentiation of the underlying procedure. A change in $\Delta\boldsymbol{\varepsilon}$ also affects $\boldsymbol{\kappa}_{t_1}$ and $\Delta\lambda_i$, which in turn affects $\Delta\boldsymbol{\sigma}''$. Under these considerations, differentiation of (4.37) with respect to $\Delta\boldsymbol{\varepsilon}$ yields

$$\frac{\partial\Delta\boldsymbol{\sigma}''}{\partial\Delta\boldsymbol{\varepsilon}} = \boldsymbol{D}\left(\boldsymbol{I} - \frac{\partial\Delta\boldsymbol{\varepsilon}^p}{\partial\Delta\boldsymbol{\sigma}''}\frac{\partial\Delta\boldsymbol{\sigma}''}{\partial\Delta\boldsymbol{\varepsilon}} - \frac{\partial\Delta\boldsymbol{\varepsilon}^p}{\partial\Delta\boldsymbol{\kappa}}\frac{\partial\Delta\boldsymbol{\kappa}}{\partial\Delta\boldsymbol{\varepsilon}} - \sum_{i=1}^{n}\frac{\partial\Delta\boldsymbol{\varepsilon}^p}{\partial\Delta\lambda_i}\frac{\partial\Delta\lambda_i}{\partial\Delta\boldsymbol{\varepsilon}}\right) \tag{4.47}$$

isolating for the derivatives associated with $\Delta\boldsymbol{\sigma}''$ gives

$$\frac{\partial\Delta\boldsymbol{\sigma}''}{\partial\Delta\boldsymbol{\varepsilon}} = \boldsymbol{D}^{\boldsymbol{c}}\left(\boldsymbol{I} - \frac{\partial\Delta\boldsymbol{\varepsilon}^p}{\partial\Delta\boldsymbol{\kappa}}\frac{\partial\Delta\boldsymbol{\kappa}}{\partial\Delta\boldsymbol{\varepsilon}} - \sum_{i=1}^{n}\frac{\partial\Delta\boldsymbol{\varepsilon}^p}{\partial\Delta\lambda_i}\frac{\partial\Delta\lambda_i}{\partial\Delta\boldsymbol{\varepsilon}}\right) \tag{4.48}$$

where

$$\boldsymbol{D}^c = \boldsymbol{T}\boldsymbol{D} \qquad \text{and} \qquad \boldsymbol{T} = \left(\boldsymbol{I} + \boldsymbol{D} \frac{\partial \Delta \boldsymbol{\varepsilon}^p}{\partial \Delta \boldsymbol{\sigma}''} \right)^{-1} \tag{4.49}$$

The involved derivatives can become quite complicated and need to be established based on the specific choice of yield functions, plastic potentials, evolution laws and return mapping scheme.

4.2.3 Principal stress space

The different functions and derivatives of the previous sections can often be hard to establish in general stress space. However, for isotropic materials, where the yield functions, plastic potentials, and evolution laws can be cast in principal stress space, the expressions often simplify.

In order to utilize this advantage, the predicted stress state of (4.33) expressed in the coordinate system of the finite element model is transformed into principal stress space according to

$$\hat{\boldsymbol{\sigma}}''_{trial} = \boldsymbol{Z}\boldsymbol{\sigma}''_{trial} \tag{4.50}$$

where $\boldsymbol{Z}$ denotes the transformation matrix between the two coordinate systems. The hat symbol is used to denote that the stress is expressed in the orthogonal basis of the principal stress directions. Thus

$$\hat{\boldsymbol{\sigma}}''_{trial} = \left[\sigma''_{1,trial} \; \sigma''_{2,trial} \; \sigma''_{3,trial} \; 0 \; 0 \; 0 \right]^T \tag{4.51}$$

is a vector of six components containing the predicted principal stresses along with the redundant non-existing shear stresses. A further notation is introduced to isolate the normal components of such principal stress space quantities, which is denoted by a bar, thus

$$\bar{\boldsymbol{\sigma}}''_{trial} = \left[\sigma''_{1,trial} \; \sigma''_{2,trial} \; \sigma''_{3,trial} \right]^T \tag{4.52}$$

is a vector of only three components containing only the principal stresses.

Afterwards, the updated stress state, $\bar{\boldsymbol{\sigma}}''_{t_1}$ is established and then transformed back into $\boldsymbol{\sigma}''_{t_1}$, which is of relevance for the finite element procedure.

Further, the consistent constitutive matrix can also be established in principal stress space, denoted $\hat{\boldsymbol{D}}^{epc}$, and then transformed back into the original coordinate system according to

$$\boldsymbol{D}^{epc} = \boldsymbol{Z}^{-1} \hat{\boldsymbol{D}}^{epc} \boldsymbol{Z}^{-T} \tag{4.53}$$

where $^{-T}$ denotes the inverse of the transpose. For further details, see e.g. Clausen et al. (2006) and Clausen (2007).

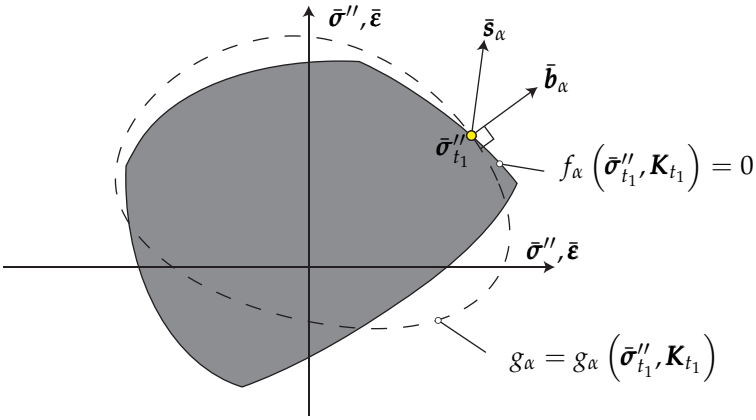

Figure 4.4: Sketch of plastic strain increment direction $\bar{\boldsymbol{b}}_\alpha$ in the case of only one active yield criterion, $f_\alpha = 0$, along with plastic corrector increment direction given by $\bar{\boldsymbol{s}}_\alpha$.

4.2.4 Return regions

Often, the solution procedure associated with the determination of $\boldsymbol{\sigma}''_{t_1}$, $\boldsymbol{\kappa}_{t_1}$ and $\Delta\lambda_i$ mentioned in section 4.2.1 rely on knowledge of which yield criteria are active for a given predicted stress state, $\boldsymbol{\sigma}''_{trial}$, and hence on which part of the yield surface, the updated stress state $\boldsymbol{\sigma}''_{t_1}$ resides. Such information can be hard to establish in general stress space. However, in the three dimensional principal stress space, this information can be estimated using geometrical arguments, as will be shown in the following.

Following the transformation and notation of section 4.2.3, the substitution of (4.40) into (4.39) gives

$$\Delta\bar{\boldsymbol{\sigma}}^{p\prime\prime} = \bar{\boldsymbol{D}} \sum_{i=1}^{n} \Delta\lambda_i \left(\frac{\partial g_i}{\partial \bar{\boldsymbol{\sigma}}''} \right)^T \Bigg|_\tau = \sum_{i=1}^{n} \Delta\lambda_i \bar{\boldsymbol{D}}\bar{\boldsymbol{b}}_i = \sum_{i=1}^{n} \Delta\lambda_i \bar{\boldsymbol{s}}_i \tag{4.54}$$

where

$$\bar{\boldsymbol{b}}_i = \left(\frac{\partial g_i}{\partial \bar{\boldsymbol{\sigma}}''} \right)^T \Bigg|_\tau \qquad \text{and} \qquad \bar{\boldsymbol{s}}_i = \bar{\boldsymbol{D}}\bar{\boldsymbol{b}}_i \tag{4.55}$$

have been introduced for readability. Thus, the plastic stress corrector increment is a linear combination of the directions given by $\bar{\boldsymbol{s}}_i$ of the active plastic potentials. For the case of only one active yield criterion, the direction of the plastic corrector increment is shown in Figure 4.4 while the case of two active yield criteria is shown in Figure 4.5.

Further, the intersection of two yield criteria forms a curve in principal stress space while the intersection of three or more yield criteria constitutes a point. By evaluating the relevant directions given by $\bar{\boldsymbol{s}}_i$ at these intersections

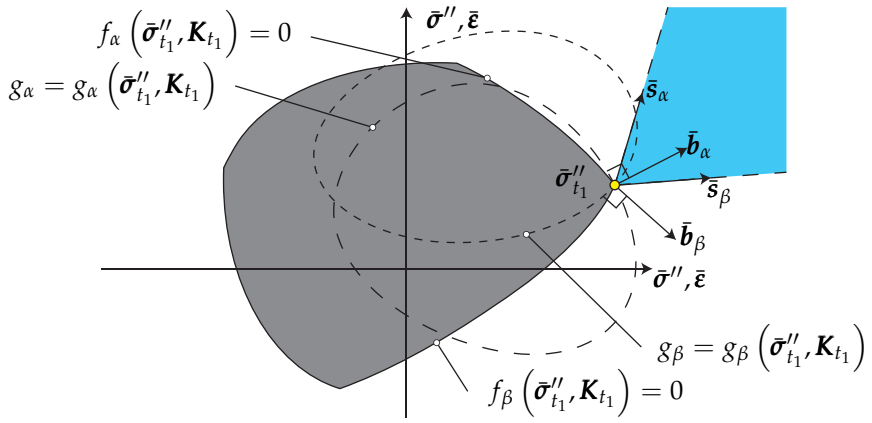

Figure 4.5: Sketch of the basis for the plastic strain increment given by the directions $\bar{\boldsymbol{b}}_\alpha$ and $\bar{\boldsymbol{b}}_\beta$ in the case of two active yield criteria, $f_\alpha = 0$ and $f_\beta = 0$, along with the basis for the plastic corrector increment given by the directions, $\bar{\boldsymbol{s}}_\alpha$ and $\bar{\boldsymbol{s}}_\beta$. The possible plastic corrector must thus lie within the blue zone.

.

and points, as shown on Figure 4.6, the inadmissible stress space is divided into regions. Each region is uniquely defined and contains the set of possible predictor stress states, which belong to the relevant part of the yield surface. Thus, by establishing which region $\bar{\boldsymbol{\sigma}}''_{trial}$ falls into, the correct location of the updated stress state, $\bar{\boldsymbol{\sigma}}''_{t_1}$, can be established.

The boundaries along the intersection of two yield criteria will, in general, be non-linear, and the location of $\bar{\boldsymbol{\sigma}}''_{trial}$ relative to these boundaries can be expensive to evaluate. However, in the case of yield criteria and plastic potentials, which are linear with respect to $\bar{\boldsymbol{\sigma}}''$, the boundaries are simply given by planes. Similarly, the boundaries surrounding a point will be given by planes for any yield criteria, non-linear or not, since the relevant directions, $\bar{\boldsymbol{s}}_i$, all pass through the same point. This is advantageous since the location of $\bar{\boldsymbol{\sigma}}''_{trial}$ relative to a plane can be easily determined.

In the general case, the shape of the yield surface as well as the derivatives of the plastic potentials are influenced by the hardening parameters, $\boldsymbol{K}$. Thus, the established boundaries are only correct for a correct $\boldsymbol{K}_{t_1}$. Since $\boldsymbol{K}_{t_1}$ is an unknown of the return mapping procedure, this is problematic. Owing to this deficiency, the location of the updated stress state can only be approximated for an incorrect value of $\boldsymbol{K}_{t_1}$. Despite of this deficiency, the approximated location can be valuable information in the prediction of a new estimate for $\bar{\boldsymbol{\sigma}}''$, $\boldsymbol{K}_{t_1}$ and $\Delta\lambda_i$. In the case of perfectly plastic models, this dependence of $\boldsymbol{K}$ is avoided, and the correct region can be precisely located.

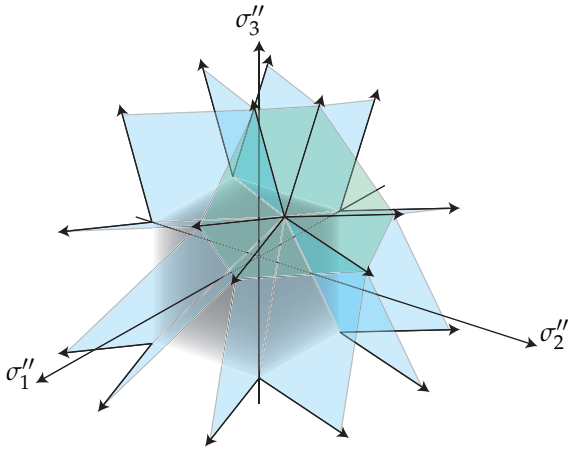

Figure 4.6: Return regions of the linear Mohr-Coulomb material model shown in Figure 1.6b outlined by the planes shown in green and blue spanned by the directions of $\tilde{\boldsymbol{s}}$ along the different parts of the yield surface shown in gray.

Chapter 5

Summary of included papers

This chapter presents a small summary for each of the included papers. The chapter has been divided into a section concerning rock modeling and a section concerning coupled soil-fluid interaction.

Since the summaries are presented in chronological order, the papers concerning rock modeling is presented first.

5.1 Rock modeling

This section gives a brief introduction to the rock-specific Hoek-Brown strength criterion followed by a short summary of the included papers A, B and C, which are all related to the numerical implementation of different constitutive models related to the Hoek-Brown criterion.

The Hoek-Brown strength criterion developed for prediction of rock mass strength is often stated as

$$\sigma''_{max} = \sigma''_{min} + \sigma_{ci}\left(m_b \frac{\sigma''_{min}}{\sigma_{ci}} + s\right)^a \tag{5.1}$$

where compression is taken as positive and σ''_{max} and σ''_{min} is the major and minor principal effective stress respectively. The strength parameters needed in the criterion encompass the uniaxial compressive strength of the intact rock material, σ_{ci}, along with three dimensionless parameters a, m_b and s (Hoek and Brown, 1980; Hoek, 1983; Hoek et al., 2002). The dimensionless parameters can be estimated through the use of the Geological Strength Index(GSI), which is a system for characterization of rock masses based on field observations (Marinos and Hoek, 2000; Hoek and Brown, 1997; Hoek et al., 2002; Hoek and Diederichs, 2006).

For use in finite element codes where tension is customarily taken as positive, the strength criterion can be treated as a yield criterion and cast

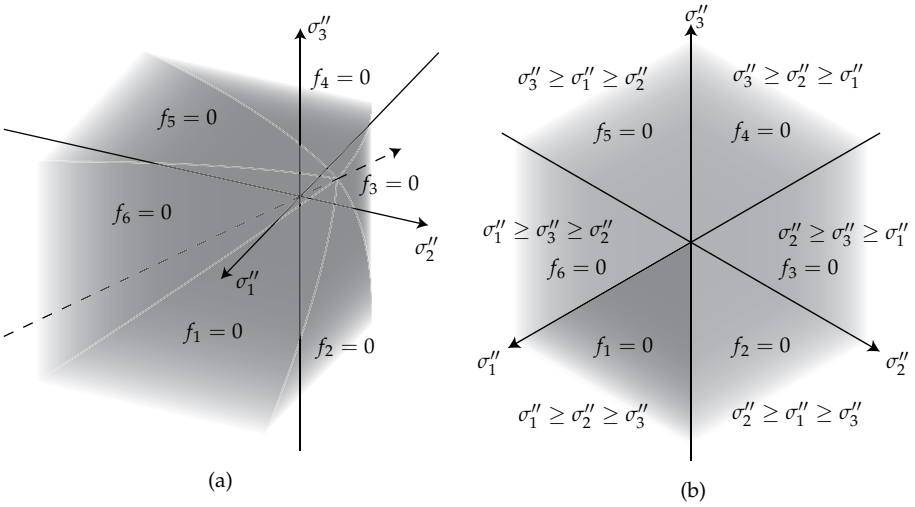

Figure 5.1: The Hoek-Brown criterion visualized in principal stress space. (a) The criterion forms a surface consisting of six individual surfaces, which are non-linear with respect to the largest principal stress σ''_{max}. (b) The Hoek-Brown criterion in principal stress space as seen from the hydrostatic axis. By proper transformation to and from principal stress space, focus can be limited to the lower left sixth of the yield surface.

as

$$f_{HB}\left(\boldsymbol{\sigma}'', \boldsymbol{K}\right) = f_{HB}\left(\sigma''_{max}, \sigma''_{min}, \boldsymbol{K}\right) = \sigma''_{max} - \sigma''_{min} - \sigma_{ci}\left(s - m_b \frac{\sigma''_{max}}{\sigma_{ci}}\right)^a = 0 \tag{5.2}$$

The visualization of the yield criterion in principal stress space for a specific set of hardening parameters reveals a six-sided pyramid with curved sides along the hydrostatic axis as shown on Figure 5.1a.

For an unordered set of principal stresses

$$\bar{\boldsymbol{\sigma}}'' = \left[\sigma_1'' \ \sigma_2'' \ \sigma_3''\right]^T \tag{5.3}$$

the yield criterion can equivalently be cast as six individual yield criteria given by

$$\begin{aligned}
f_1\left(\boldsymbol{\sigma}'', \boldsymbol{K}\right) &= f_{HB}\left(\sigma_1'', \sigma_3'', \boldsymbol{K}\right) = 0, \quad f_2\left(\boldsymbol{\sigma}'', \boldsymbol{K}\right) = f_{HB}\left(\sigma_2'', \sigma_3'', \boldsymbol{K}\right) = 0 \\
f_3\left(\boldsymbol{\sigma}'', \boldsymbol{K}\right) &= f_{HB}\left(\sigma_2'', \sigma_1'', \boldsymbol{K}\right) = 0, \quad f_4\left(\boldsymbol{\sigma}'', \boldsymbol{K}\right) = f_{HB}\left(\sigma_3'', \sigma_1'', \boldsymbol{K}\right) = 0 \\
f_5\left(\boldsymbol{\sigma}'', \boldsymbol{K}\right) &= f_{HB}\left(\sigma_3'', \sigma_2'', \boldsymbol{K}\right) = 0, \quad f_6\left(\boldsymbol{\sigma}'', \boldsymbol{K}\right) = f_{HB}\left(\sigma_1'', \sigma_2'', \boldsymbol{K}\right) = 0
\end{aligned} \tag{5.4}$$

in conjunction with the definitions given in section 4.1.3.

A similar expression is used for the plastic potential

$$g_{HB}\left(\boldsymbol{\sigma}'', \boldsymbol{K}\right) = g_{HB}\left(\sigma''_{max}, \sigma''_{min}, \boldsymbol{K}\right) = \sigma''_{max} - \sigma''_{min} - \sigma_{ci_g}\left(s_g - m_{b_g} \frac{\sigma''_{max}}{\sigma_{ci}}\right)^{a_g} \tag{5.5}$$

but with a different set of parameters, σ_{ci_g}, a_g, m_{b_g} and s_g. This definition allows for non-associated plasticity and can equivalently be split into six plastic potentials according to

$$\begin{aligned} g_1\left(\boldsymbol{\sigma}'', \boldsymbol{K}\right) &= g_{HB}\left(\sigma_1'', \sigma_3'', \boldsymbol{K}\right), \quad g_2\left(\boldsymbol{\sigma}'', \boldsymbol{K}\right) = g_{HB}\left(\sigma_2'', \sigma_3'', \boldsymbol{K}\right) \\ g_3\left(\boldsymbol{\sigma}'', \boldsymbol{K}\right) &= g_{HB}\left(\sigma_2'', \sigma_1'', \boldsymbol{K}\right), \quad g_4\left(\boldsymbol{\sigma}'', \boldsymbol{K}\right) = g_{HB}\left(\sigma_3'', \sigma_1'', \boldsymbol{K}\right) \\ g_5\left(\boldsymbol{\sigma}'', \boldsymbol{K}\right) &= g_{HB}\left(\sigma_3'', \sigma_2'', \boldsymbol{K}\right), \quad g_6\left(\boldsymbol{\sigma}'', \boldsymbol{K}\right) = g_{HB}\left(\sigma_1'', \sigma_2'', \boldsymbol{K}\right) \end{aligned} \tag{5.6}$$

When return mapping in principal stress space is applied, then transformation of the predicted stress state, $\boldsymbol{\sigma}''_{trial}$, into principal stress space is required as mentioned in section 4.2.3. If this transformation is carried out such that the obtained principal stresses fulfill $\sigma''_{max} = \sigma''_1 \geq \sigma''_2 \geq \sigma''_3 = \sigma''_{min}$, then focus can be restricted to only a sixth of the principal stress space as indicated on Figure 5.1b, where $f_1 = 0$ must be fulfilled for all stress states experiencing plastic straining. This reduces the location of the updated stress state significantly and thus simplifies the implementation.

These considerations constitute the backbone of the numerical implementations developed within this PhD study. Paper A and B concerns the development of a strain softening implementation of the Hoek-Brown material model while paper C concerns the development of a perfectly-plastic implementation of the Hoek-Brown material model with a tension cut off.

5.1.1 Paper A

In this paper, a softening Hoek-Brown material model is implemented for which the internal state variables amount to a single variable

$$\boldsymbol{\kappa} = \left\{\bar{\varepsilon}^p\right\} \tag{5.7}$$

which in this context is an approximate measure of the accumulated plastic strain given by the evolution law

$$\dot{\bar{\varepsilon}}^p = \sum_{i=1}^{6} \dot{\lambda}_i \tag{5.8}$$

and should thus not be confused with the more common definition of accumulated plastic strain given by (4.7).

The implementation is able to handle an arbitrary development of the hardening parameters defined by

$$\boldsymbol{K}\left(\bar{\varepsilon}^p\right) = \left\{\sigma_{ci},\ a,\ m_b,\ s,\ \sigma_{ci_g},\ a_g,\ m_{b_g},\ s_g\right\} \tag{5.9}$$

through a user-defined set of k individual points

$$\left(\bar{\varepsilon}^p_1, \boldsymbol{K}_1\right),\ \ldots,\ \left(\bar{\varepsilon}^p_k, \boldsymbol{K}_k\right) \tag{5.10}$$

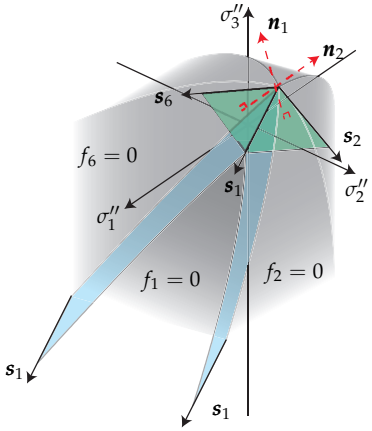

Figure 5.2: Subdivision of principal stress space into return regions as described in section 4.2.4 using a similar approach as Clausen and Damkilde (2008). Only the boundaries within $\sigma_1'' \geq \sigma_2'' \geq \sigma_3''$ are shown. As can be seen, the boundaries concerning the apex (shown in green) are given by planes, whereas the boundaries related to the intersection of $f_1 = f_2$ and $f_1 = f_6$ are slightly curved (shown in blue).

allowing for the modeling of perfectly-plastic, softening, and hardening material behavior.

The implementation uses a fully implicit return mapping procedure. The updated stress state can be situated solely on $f_1 = 0$, the intersection of $f_1 = f_2$, the intersection of $f_1 = f_6$ or at the apex given by the intersection of all six yield criteria. Consequently, four different return algorithms were developed utilizing a Newton-Raphson iteration scheme, using (4.38) as the point of departure along with the fulfillment of the yield criteria stated in (5.4). Based on the initial hardening parameters, $\boldsymbol{K}_{t_0}$, the stress space is divided into different return regions as described in 4.2.4 using a similar approach as stated in Clausen and Damkilde (2008) for an elastic-perfectly-plastic version of the Hoek-Brown model. A visualization is shown in Figure 5.2. Based on this, the appropriate return algorithm can be estimated. If the estimated return algorithm fails, the return regions are updated using the current guess of the hardening parameters and a new return algorithm is estimated.

The implementation is employed on a tunnel excavation simulation in a brittle rock mass exhibiting non-associated behavior. The results are found to be in good agreement with an analytical solution given in Sharan (2008).

5.1.2 Paper B

This paper presents a further development and verification of the model from paper A, which is capable of utilizing a broader set of evolution laws, includ-

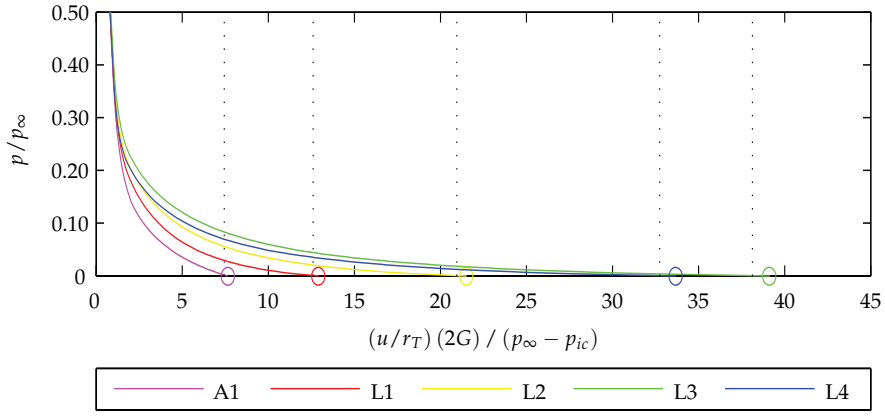

Figure 5.3: Prediction of tunnel wall displacement, u, as the pressure on the wall, p, is reduced from the in situ pressure, p_∞ to 0. The tunnel wall displacement has been scaled relative to the displacement at the onset of plastic straining. A1 and L1 - L4 represent different material parameters all assuming a strain softening behavior. The vertical dotted lines represent an analytical solution predicted by Wang et al. (2010).

ing the ones stated in (4.7) and (4.10), which are often used within the field of rock mechanics and makes it possible to compare the numerical implementation with a variety of analytical solutions for strain softening behavior.

The implementation uses slightly different return algorithms and also presents a slightly modified region detection scheme where the correct return region is estimated for each individual guess of the updated stress state. This is made possible by a simplified evaluation of the non-linear boundaries surrounding the intersection of two neighboring yield criteria, which is only correct for a correctly updated stress state, but can be used as an estimate for an approximately correct updated stress state.

The improved implementation is likewise verified through a series of tunnel excavation simulations, which also encompass strain softening behavior, for which analytical solutions are available (Lee and Pietruszczak, 2008; Wang et al., 2010), see Figure 5.3.

5.1.3 Paper C

This paper combines the Hoek-Brown criterion with a tension cut-off given by the yield criterion

$$f_{TC}\left(\boldsymbol{\sigma}'', \boldsymbol{K}\right) = f_{TC}\left(\sigma''_{max}, \boldsymbol{K}\right) = \sigma''_{max} - \sigma''_t = 0 \tag{5.11}$$

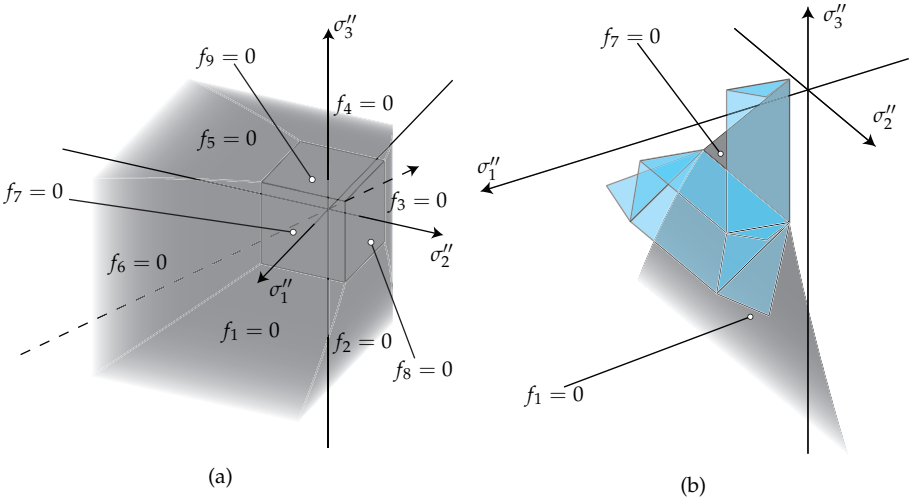

Figure 5.4: (a) The Hoek-Brown criterion combined with a tension cut-off shown in principal stress space. (b) Relevant part of yield surface along with the boundaries defining the different return regions for $\sigma_1'' \geq \sigma_2'' \geq \sigma_3''$.

which can equivalently be cast as three additional yield criteria

$$\begin{aligned} f_7\left(\boldsymbol{\sigma}'', \boldsymbol{K}\right) &= f_{TC}\left(\sigma_1'', \boldsymbol{K}\right) = 0 \\ f_8\left(\boldsymbol{\sigma}'', \boldsymbol{K}\right) &= f_{TC}\left(\sigma_2'', \boldsymbol{K}\right) = 0 \\ f_9\left(\boldsymbol{\sigma}'', \boldsymbol{K}\right) &= f_{TC}\left(\sigma_3'', \boldsymbol{K}\right) = 0 \end{aligned} \tag{5.12}$$

along with a set of plastic potentials

$$\begin{aligned} g_7\left(\boldsymbol{\sigma}'', \boldsymbol{K}\right) &= f_{TC}\left(\sigma_1'', \boldsymbol{K}\right) \\ g_8\left(\boldsymbol{\sigma}'', \boldsymbol{K}\right) &= f_{TC}\left(\sigma_2'', \boldsymbol{K}\right) \\ g_9\left(\boldsymbol{\sigma}'', \boldsymbol{K}\right) &= f_{TC}\left(\sigma_3'', \boldsymbol{K}\right) \end{aligned} \tag{5.13}$$

from which it follows that associated plasticity is assumed. Similar to the other implementations, this implementation also utilizes fully implicit return mapping in principal stress space. The combined yield surface in principal stress space is shown in Figure 5.4a.

In total, the updated stress state can reside on nine different locations, for which the accompanying return regions can be seen on Figure 5.4b.

The implementation is carried out assuming perfect plasticity, such that the material parameters are kept constant throughout the analysis, i.e.

$$\dot{\boldsymbol{K}} = 0 \tag{5.14}$$

Owing to this, the return algorithms presented in Clausen and Damkilde (2008) and Clausen and Damkilde (2006) can be readily combined.

The implementation is used to investigate the effects of the tension cut-off on the safety factor of an underground opening. For the example studied, it is found that the safety factor is greatly affected by the tension cut-off value.

5.2 Dynamic soil-fluid interaction

The *u-p-U* formulation given in section 3.3 is generally not available through the common commercial finite element codes such as Abaqus or Plaxis, which rely on a simplified set of equations known as the *u-p* formulation, where the acceleration of the fluid relative to the soil skeleton is neglected in the equilibrium conditions. This reduces the equation for the equilibrium of the mixture (3.17) to

$$\sigma_{ij,j} + \rho b_i = \rho \ddot{u}_i \tag{5.15}$$

and further, the fluid equilibrium condition (3.18) can be combined with the mass balance condition (3.22) to give

$$\left(k\left(-p_{,i} - \rho_f \ddot{u} + \ \rho_f b_i\right)\right)_{,i} + \alpha \dot{\varepsilon}_{ii} + \frac{1}{Q}\dot{p} = 0 \tag{5.16}$$

Now, only the skeleton displacement, u, and pore pressure, p, along with their time derivatives appear in the equations, which are discretized in a similar manor to the *u-p-U* formulation using the weighted residual Galerkin approach. For further details, see Zienkiewicz et al. (1999); Zienkiewicz and Shiomi (1984). The implementation is further simplified in Abaqus, which only incorporates the *u-p* formulation in a quasi-static form, neglecting all inertial terms.

In this PhD study, a custom-made finite element code has been developed in object-oriented Fortran, which incorporates the full *u-p-U* formulation. The code has been verified through numerous test problems of both quasi-static and dynamic nature, see Gajo et al. (1994); Jeremić et al. (2008); Tasiopoulou et al. (2015). Further, the simplified *u-p* formulation including inertial terms has also been implemented and verified.

This custom-made finite element code has been used in the included paper D, for which a summary is given below.

5.2.1 Paper D

This paper is concerned with the dynamic tensile resistance of suction buckets. As mentioned in section 1.1.1, the tensile resistance, F_t, of the suction bucket concept utilized in saturated soils is highly time-dependent. The primary source of this time dependence can be explained by first considering a very slow pullout velocity. In such a case, the failure is governed by frictional slip along the inside and outside skirt edges, and the soil only displaces

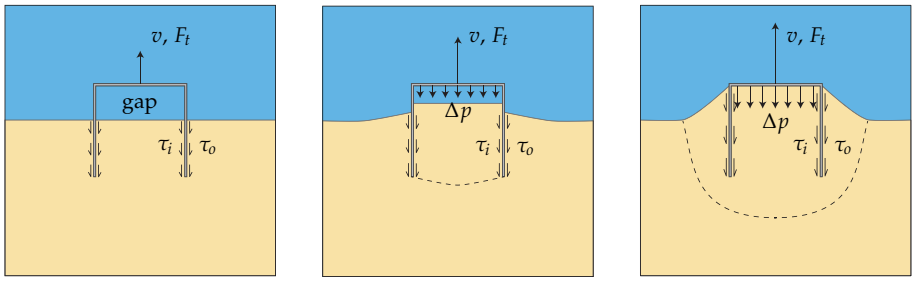

Figure 5.5: Different failure mechanisms of bucket foundation under tensile loading, F_t, depending on pullout velocity, v. (a) Drained behavior governed by friction along inside and outside skirt, τ_i and τ_o respectively. Development of gap between soil and bucket lid. (b) Partially drained behavior with friction along skirt and suction, Δp, beneath bucket lid. Reduced gap development. (c) Undrained behavior with friction along skirt and suction beneath bucket lid. No gap development.

slightly since it is kept in place through gravity. Owing to this, a gap develops between the bucket lid and the seabed as shown in Figure 5.5a, which can be thought of as a steady and slow increase in pore volume. In effect, a slight pressure drop arises, which drives a flow into the bucket and fills the gap in accordance with the continuity equation of (3.22).

A key point of the suction bucket concept is that, for larger pullout velocities, the gap expansion is sought established over such a short time duration that a significant suction develops beneath the bucket lid, which is beneficial for the tensile resistance. However, as the developed suction becomes significant, it also affects the failure mechanism of the bucket due to the complex coupled behavior between the fluid flow and the solid skeleton. One reason is that the soil inside the bucket can be sucked up along with the bucket, as shown in Figure 5.5b for a partially drained case, which causes failure in the soil beneath the bucket. In the undrained case, the gap is completely prevented from expanding as shown in Figure 5.5c. Further, the suction alters the mean effective stresses in the soil, which affect the capacity of the interface between the bucket and the soil. In addition to this, liquefaction might take place due to the upwards directed seepage inside the bucket and the pressure drop could be so severe that cavitation arises. For further details, see e.g. Iskander et al. (1993); Feld (2001); Kelly et al. (2006); Senders (2008); Vaitkunaite et al. (2014).

The problem has been treated numerically in e.g. Cao et al. (2002); Thieken et al. (2014); Achmus and Thieken (2014). Common for these approaches is that they are based on the quasi-static implementation available in Abaqus. In order to investigate the effects of inertial terms, the tensile resistance of a suction bucket is investigated using the *u-p-U* formulation, the *u-p* formula-

tion and the quasi-static *u-p* formulation.

The models are based on a similar approach as the one used in Thieken et al. (2014). As basis for comparison, a single suction bucket placed in dense sand is considered for various pullout velocities. An elastic-perfectly plastic Mohr-Coulomb material model is used. The dynamic *u-p-U* and *u-p* models are simulated using the aforementioned custom-made finite element code while Abaqus is used for the quasi-static models. This serves as a further verification of the custom-made finite element code since they should predict similar resistance in the drained case.

Generally, it is found that there are no significant differences between the formulations except for very rapid pullout velocities where the dynamic formulations predict the formation of a downwards directed wave of negative pore pressure originating at the bucket lid.

Chapter 6

Conclusion and future work

The main conclusions to be drawn from the work carried out during this PhD study can be summarized as follows:

- A numerical implementation of a non-associated strain softening Hoek-Brown material model has been developed. The implementation is capable of modeling the different post-peak behaviors observed in rock masses. Using return mapping in principal stress space, four different iterative algorithms were developed to account for the non-linear and discontinuous nature of the criterion. Further, different schemes to determine the correct location of the updated stress state have been developed based on the principle of boundary planes, which take into account that these boundaries are not static due to changes in hardening parameters. The model has been applied on axisymmetric simulations of tunnel excavations, for which it was found to be in good agreement with available analytical solutions.

- A numerical implementation of a non-associated elastic-perfectly plastic Hoek-Brown material model incorporating a tension cut-off has been developed. Since perfect plasticity is assumed, known and proved return algorithms are available for both the Hoek-Brown criterion and the tension cut-off. These algorithms have been combined using a suitable scheme to determine the correct location of the updated stress state. The implementation is utilized to investigate the influence of the tensile strength on the safety factor of an underground opening.

- A custom-made finite element program has been developed incorporating the *u-p-U* formulation used for simulation of dynamic soil-fluid interaction of fully saturated porous media. This formulation features the inclusion of inertia of the fluid and is generally not available through the commercial finite element codes. In addition to this, the simplified

u-p formulation neglecting fluid inertia has also been incorporated in the code. The developed code has been verified for a series of relevant test problems.

- The custom-made finite element program has been utilized to assess the importance of the inertial terms for the tensile resistance of the suction bucket concept. A single suction bucket has been simulated for various pullout velocities using the *u-p-U* and *u-p* formulations. The predicted solutions are compared to a quasi-static solution predicted by the commercial finite element code Abaqus. Generally, it is found that the inertial terms are insignificant for all realistic pullout velocities, and that the quasi-static *u-p* formulation suffice. Further, it is found that the differences between the *u-p-U* and *u-p* formulations are insignificant even for very rapid pull-out velocities for the specific problem considered.

6.1 Future work

Based on the work carried out in this thesis, a list of recommendations for future initiatives is given below.

- The developed constitutive models of the Hoek-Brown criterion could be combined into a model incorporating both strain softening behavior and a tension cut off. The return algorithms of the softening criterion can be used without modification; however, the region detection scheme of the modified Hoek-Brown criterion and the return algorithms concerning the tension cut-off should be updated to account for changes in the hardening parameters.

- The approach taken in the strain softening Hoek-Brown model can be applied to other discontinuous isotropic criteria as well. An obvious candidate would be the simpler linear Mohr-Coulomb criterion.

- The investigated suction bucket analysis relied on a simple displacement-based model with an almost constant pullout velocity. Such loading is probably not that realistic for real world scenarios. It could thus be interesting to undertake a load-based approach instead where a representative time varying load is applied to the bucket instead in order to see whether or not this would affect the results predicted by the different numerical formulations. Further, it should be compared to experimental results.

- The developed finite element code could be applied to other problems of dynamic nature, which are believed to be more influenced by the inertial terms.

- The developed finite element code could be extended to incorporate e.g. partially saturated porous materials, large deformations, time-varying permeability as well as cavitation.

References

Achmus, M. and Thieken, K. (2014). Numerical simulation of the tensile resistance of suction buckets in sand. *Journal of Ocean and Wind Energy*, 1(4):231–239.

Andersen, L. V. (2007). Effective stresses in soil and rock and consolidation in three dimensions. DCE Lecture Note 14, Aalborg University.

Bathe, K. J. (1996). *Finite Element Procedures*. Prentice-Hall.

Biot, M. A. (1941). General theory of three-dimensional consolidation. *Journal of Applied Physics*, 12(2):155–164.

Biot, M. A. (1955). Theory of elasticity and consolidation for a porous anisotropic solid. *Journal of Applied Physics*, 26(2):182–185.

Biot, M. A. and Willis, D. G. (1957). The elastic coefficients of the theory of consolidation. *Journal of Applied Mechanics*, 24:594–601.

Brown, E. T., Bray, J. W., Ladanyi, B., and Hoek, E. (1983). Ground response curves for rock tunnels. *Journal of Geotechnical Engineering*, 109:15–39.

Cao, J., Phillips, R., Popescu, R., Audibert, J. M. E., and Al-Khafaji, Z. (2002). Numerical analysis of the behavior of suction caissons in clay. In *Proceedings of The Twelfth (2002) International Offshore and Polar Engineering Conference*, Kitakyushu, Japan.

Clausen, J. (2007). *Efficient Non-Linear Finite Element Implementation of Elasto-Plasticity for Geotechnical Problems*. PhD thesis, Computational Mechanics, Esbjerg Institute of Technology, Aalborg University Esbjerg. http://vbn.aau.dk/files/14058639/JCthesis.pdf.

Clausen, J. and Damkilde, L. (2006). A simple and efficient FEM-implementation of the modified Mohr-Coulomb criterion. In *Proceedings of the 19th Nordic Seminar on Computational Mechanics*, pages 214–219, Lund, Sweden.

Clausen, J. and Damkilde, L. (2008). An exact implementation of the Hoek-Brown criterion for elasto-plastic finite element calculations. *International Journal of Rock Mechanics & Mining Sciences*, 45:831–847.

Clausen, J., Damkilde, L., and Andersen, L. (2006). Efficient return algorithms for associated plasticity with multiple yield planes. *International Journal for Numerical Methods in Engineering*, 66:1036–1059.

Cook, R. D., Malkus, D. S., Plesha, M. E., and Witt, R. J. (2002). *Concepts and Applications of Finite Element Analysis*. John Wiley & Sons, 4th edition.

Crisfield, M. A. (2000). *Non-linear finite element analysis of solids and structures Volume 2 Advanced Topics*. John Wiley & Sons.

Dassault Systèmes Simulia Corp (2014). *Abaqus 6.14*. http://www.3ds.com/products-services/simulia/products/abaqus/.

de Souza Neto, E. A., Perić, D., and Owen, D. R. J. (2008). *Computational Methods for Plasticity*. Wiley, London.

Feld, T. (2001). *Suction buckets, a new innovative foundation concept applied to offshore wind turbines*. PhD thesis, Geotechnical Engineering Group, Aalborg University.

Gajo, A., Saetta, A., and Vitaliani, R. (1994). Evaluation of three- and two-field finite element methods for the dynamic response of saturated soil. *International journal for numerical methods in engineering*, 37:1231–1247.

Hansen, N. E. O. (2003). Soil reactions in saturated sand to impulsive loads. In *Seminar on Dynamic Loads to Stone Bed Foundations - from Offshore Wind Turbines to Earthquake*.

Hansen, N. E. O. and Gislason, K. (2007). Soil reactions in saturated sand caused by impulsive loads. *Journal of Waterway, Port, Coastal and Ocean Engineering*, 133(1):39–49.

Hoek, E. (1983). Strength of jointed rock masses. *Géotechnique*, 23(3):187–223.

Hoek, E. and Brown, E. T. (1980). Empirical strength criterion for rock masses. *Journal of Geotechnical Engineering*, 106:1013–1035.

Hoek, E. and Brown, E. T. (1997). Practical estimates of rock mass strength. *International Journal of Rock Mechanics & Mining Sciences*, 34:1165–1186.

Hoek, E., Carranza-Torres, C., and Corkum, B. (2002). Hoek-Brown failure criterion - 2002 edition. *Proc. NARMS-TAC Conference, Toronto*, 1:267–273.

Hoek, E. and Diederichs, M. S. (2006). Empirical estimation of rock mass modulus. *International Journal of Rock Mechanics & Mining Sciences*, 43:203–215.

Holtz, R. D., Kovacs, W. D., and Sheahan, T. C. (2010). *An Introduction to Geotechnical Engineering*. Pearson.

Iskander, M. G., Olson, R. E., and Pavlicek, R. W. (1993). Behavior of suction piles in sand. In *Design and performance of deep foundations: Piles and piers in soil and soft rock*, pages 157–171, Dallas, Texas, United States.

ISO 14688-1 (2002). Geotechnical investigation and testing - identification and classification of soil - part 1: Identification and description. ISO 14688-1, European Committee for Standardization.

Iwanec, A. M. S. (2014). *The Geomechanics of Single-Seam and Multi-Seam Longwall Coal Mining*. PhD thesis, The University of Newcastle, Australia. http://hdl.handle.net/1959.13/1045347.

Jaeger, J. C., Cook, N., and Zimmerman, R. (2007). *Fundamentals of rock mechanics*. Blackwell Publishing, fourth edition.

Jeremić, B., Cheng, Z., Taiebat, M., and Dafalias, Y. (2008). Numerical simulation of fully saturated porous materials. *International journal for numerical and analytical methods in geomechanics*, 32:1635–1660.

Katona, M. G. and Zienkiewicz, O. C. (1985). A unified set of single step algorithms part 3: The beta-m method, a generalization of the newmark scheme. *International Journal for Numerical Methods in Engineering*, 21:1345–1359.

Kelly, R. B., Houlsby, G. T., and Byrne, B. W. (2006). Transient vertical loading of model suction caissons in a pressure chamber. *Géotechnique*, 56(10):665–675.

Koiter, W. T. (1953). Stress-strain relations, uniqueness and variational theorems for elasto-plastic materials with a singular yield surface. *Quarterly of Applied Mathematics*, 11:350–354.

Kramer, S. L. (1996). *Geotechnical Earthquake Engineering*. Prentice Hall.

Lee, Y.-K. and Pietruszczak, S. (2008). A new numerical procedure for elasto-plastic analysis of a circular opening excavated in a strain-softening rock mass. *Tunnelling and Underground Space Technology*, 23:588–599.

Marinos, P. and Hoek, E. (2000). GSI: A geologically friendly tool for rock mass strength estimation. In *Proceedings of the International Conference on Geotechnical and Geological Engineering*, pages 1422–1446, Melbourne, Australia.

Nagtegaal, J. C. (1982). On the implementation of inelastic constitutive equations with special reference to large deformation problems. *Computer Methods in Applied Mechanics and Engineering*, 33:469–484.

Norbury, D. (2010). *Soil and Rock Description in Engineering Practice*. Whittles Publising.

oilrig-photos.com (2015). Hurricane at Oseberg A, 19 Jan 2007. http://www.oilrig-photos.com/picture/number246.asp. Online; accessed 17 December 2015.

Ottosen, N. S. and Ristinmaa, M. (2005). *The Mechanics of Constitutive Modeling*. Elsevier, London.

Plaxis (2015). *PLAXIS 3D*. www.plaxis.nl.

Senders, M. (2008). *Suction caissons in sand as tripod foundations for offshore wind turbines*. PhD thesis, School of Civil and Resource Engineering, University of Western Australia.

Sharan, S. K. (2008). Analytical solutions for stress and displacements around a circular opening in a generalized Hoek-Brown rock. *International Journal of Rock Mechanics & Mining Sciences*, 45:78–85.

Simo, J. C. and Taylor, R. L. (1985). Consistent tangent operators for rate-independent elastoplasticity. *Computer Methods in Applied Mechanics and Engineering*, 48:101–118.

Soil Survey Division Staff (1993). *Soil Survey Manual*. United States Department of Agriculture.

Tasiopoulou, P., Taiebat, M., Tafazzoli, N., and Jeremić, B. (2015). Solution verification procedures for modeling and simulation of fully coupled porous media: static and dynamic behavior. *Coupled systems mechanics*, 4(1):67–98.

Thieken, K., Achmus, M., and Schröder, C. (2014). On the behavior of suction buckets in sand under tensile loads. *Computers and Geotechnics*, 60:88–100.

Vaitkunaite, E., Ibsen, L. B., and Nielsen, B. N. (2014). New medium-scale laboratory testing of a bucket foundation capacity in sand. In *Proceedings of the Twenty-fourth (2014) International Ocean and Polar Engineering Conference*, volume 2, pages 514–520, Busan, South Korea.

Wang, S., Yin, X., Tang, H., and Ge, X. (2010). A new approach for analyzing circular tunnel in strain-softening rock masses. *Internation Journal of Rock Mechanics & Mining Sciences*, 47:170–178.

Zienkiewicz, O. C., Chan, A. H. C., Pastor, M., Schrefler, B. A., and Shiomi, T. (1999). *Computational geomechanics with special reference to earthquake egnineering*. John Wiley & Sons.

Zienkiewicz, O. C. and Shiomi, T. (1984). Dynamic behavior of saturated porous media; the generalized biot formulation and its numerical solution. *International journal for numerical and analytical methods in geomechanics*, 8:71–96.

Zienkiewicz, O. C. and Taylor, R. L. (2000). *The Finite Element Method Volume 1 The Basis*. Butterworth-Heinemann, 5th edition.

Paper A

Numerical implementation of the Hoek-Brown material model with strain hardening

E. S. Sørensen, J. Clausen & L. Damkilde

The paper has been published in
Research and Applications in Structural Engineering, Mechanics and Computation - Proceedings of the 5th International Conference on Structural Engineering, Mechanics and Computation, SEMC 2013 pp. 375–380, 2013.

The paper was rewarded with a Young Researcher Fellowship Award at the SEMC 2013 conference.

Research and Applications in Structural Engineering, Mechanics and Computation – Zingoni (Ed.)

Numerical implementation of the Hoek-Brown material model with strain hardening

E.S. Sørensen, J. Clausen & L. Damkilde
Department of Civil Engineering, Aalborg University, Aalborg, Denmark

ABSTRACT: A numerical implementation of the Hoek-Brown criterion is presented, which is capable of modeling important aspects of the different post-failure behaviors observed in jointed rock mass. This is done by varying the material parameters based on the accumulated plastic strains. The implementation is for use in finite element calculations, and is based on the return mapping framework. The updated stress state is found in principal stress space based on the principles of boundary planes and a consistent constitutive matrix is found for better convergence of the global equilibrium iterations. The constitutive model is demonstrated on a simulation of a tunnel excavation and the results are compared with an analytical solution for a tunnel excavation in elastic-brittle rock material.

1 INTRODUCTION

Rock masses are often encountered within the fields of civil and mining engineering. Examples include tunnel excavations, foundations and slope stability problems. According to Hoek & Brown (1997), the post-failure behavior of rock masses falls into three categories. A very good quality hard rock mass tends to show an elastic-brittle behavior, where the strength drops rapidly once yielding occurs. Average quality rock mass is believed to show a strain-softening behavior, where the strength decrease with an increase in plastic strains. Rock mass of poor quality behaves in an elastic-perfectly-plastic fashion. The analytical solutions of a tunnel excavation provided by Sharan (2008) demonstrate the impact of an elastic-brittle behavior compared to a perfectly plastic behavior.

To model the strength of rock masses, the Hoek-Brown yield criterion is often applied (Hoek et al. 2002). This paper seeks to implement a Hoek-Brown material model able to incorporate all three post-failure behaviors for use in finite element calculations.

2 THE HOEK-BROWN CRITERION

The Hoek-Brown criterion has evolved from the original Hoek-Brown criterion used for hard rock masses into the more versatile generalized Hoek-Brown criterion, which states that plastic deformations develop once

$$\sigma_1' = \sigma_3' + \sigma_{ci}\left(m_b\frac{\sigma_3'}{\sigma_{ci}} + s\right)^a \tag{1}$$

where σ_1' is the largest effective principal stress, σ_3' is the smallest effective principal stress, σ_{ci} is the uniaxial compressive strength of the intact rock material and m_b, s and a are material parameters. Compression is taken as positive. Throughout the rest of this paper, effective stresses are implied and the primes will thus be left out for simplicity. The material parameters m_b, s and a and the Youngs modulus, E can be found based on the Geological Strength Index, GSI, the disturbance factor, D, and the intact rock parameter, m_i (Hoek et al. 2002), (Hoek & Diederichs 2006).

3 PLASTICITY FUNDAMENTALS

The basic theory behind plasticity relies on one or more yield functions, $f_1, \ldots, f_n$, which are scalar functions of the stress state, $\boldsymbol{\sigma}$, and some hardening parameters, $\boldsymbol{K}$. Plastic strains start to develop once the material reaches its yielding limit, which is defined by the yield criteria

$$f_i(\boldsymbol{\sigma}, \boldsymbol{K}) = 0, \quad i = 1, \ldots, n \tag{2}$$

Any combination of $\boldsymbol{\sigma}$ and $\boldsymbol{K}$ fulfilling one or more of the criteria leads to additional plastic straining. Any combination of $\boldsymbol{\sigma}$ and $\boldsymbol{K}$ resulting in negative values of all yield criteria does not result in additional plastic straining and any combination resulting in a positive value of any of the functions is inadmissible. The manner in which the plastic strains develop is governed by the plastic potential functions, $g_1, \ldots, g_n$, which are also functions of $\boldsymbol{\sigma}$ and $\boldsymbol{K}$, and the non-negative plastic multipliers $\lambda_1, \ldots, \lambda_n$, such that

$$d\boldsymbol{\varepsilon}^p = \sum_{i=1}^{n} \alpha_i \, d\lambda_i \frac{\partial g_i}{\partial \boldsymbol{\sigma}} \tag{3}$$

where α_i is 1 if yield criterion i is active, and 0 otherwise. The hardening parameters, $\boldsymbol{K}$, are functions of

the state variables, $\boldsymbol{\kappa}$, that define the internal state of the material

$$\boldsymbol{K} = \boldsymbol{K}(\boldsymbol{\kappa}) \tag{4}$$

The evolution of the state variables is defined by the evolution law

$$d\boldsymbol{\kappa} = \sum_{i=1}^{n} \alpha_i \, d\lambda_i \boldsymbol{k}_i(\boldsymbol{\sigma}, \boldsymbol{K}) \tag{5}$$

where $\boldsymbol{k}_1, \ldots, \boldsymbol{k}_n$ are some functions, that must be appropriately chosen.

Further details of the FE-method and plasticity can be found in Ottosen & Ristinmaa (2005), de Souza Neto, Perić, & O wen (2008) and Clausen (2007).

4 RETURN MAPPING

The numerical implementation relies on return mapping, which initially assumes that the strain increment, $\Delta\boldsymbol{\varepsilon}$, from the global equilibrium iterations, is entirely elastic, resulting in an elastic predictor stress increment

$$\Delta\boldsymbol{\sigma}^e = \boldsymbol{D}\Delta\boldsymbol{\varepsilon} \tag{6}$$

which combined with the initial stress state, $\boldsymbol{\sigma}^A$, results in a predicted elastic stress state

$$\boldsymbol{\sigma}^B = \boldsymbol{\sigma}^A + \Delta\boldsymbol{\sigma}^e \tag{7}$$

If the evaluation of one or more of the yield criteria with this stress state and the initial hardening parameters, $\boldsymbol{K}^A$, results in a positive value, the stress state is inadmissible, cf. figure 1.

To find the updated stress state, a plastic corrector, $\Delta\boldsymbol{\sigma}^p$, is introduced

$$\begin{aligned} \Delta\boldsymbol{\sigma}^p &= \boldsymbol{D}\Delta\boldsymbol{\varepsilon}^p = \boldsymbol{D}\sum_{i=1}^{n} \alpha_i \int_{\lambda_i^A}^{\lambda_i^C} \frac{\partial g_i}{\partial \boldsymbol{\sigma}} d\lambda_i \\ &\approx \sum_{i=1}^{n} \alpha_i \Delta\lambda_i \boldsymbol{D} \left.\frac{\partial g_i}{\partial \boldsymbol{\sigma}}\right|_C = \sum_{i=1}^{n} \alpha_i \Delta\lambda_i \boldsymbol{s}_i \end{aligned} \tag{8}$$

where (3) has been used. Thus, the plastic corrector is some linear combination of the directions

$$\boldsymbol{s}_i = \boldsymbol{D}\left.\frac{\partial g_i}{\partial \boldsymbol{\sigma}}\right|_C \tag{9}$$

given by each active yield surface. The updated stress state becomes

$$\boldsymbol{\sigma}^C = \boldsymbol{\sigma}^B - \Delta\boldsymbol{\sigma}^p = \boldsymbol{\sigma}^B - \sum_{i=1}^{n} \alpha_i \Delta\lambda_i \boldsymbol{s}_i \tag{10}$$

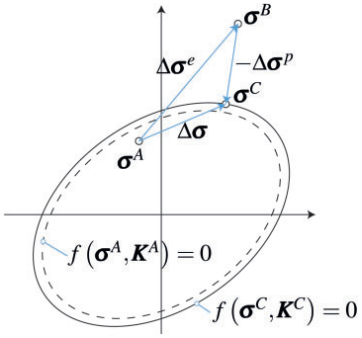

Figure 1. Sketch of the updating scheme.

In this regard, α_i is 1 for the yield criteria, which are satisfied for the updated stress state and zero otherwise. The updated stress state must fulfill

$$\alpha_i f_i\left(\boldsymbol{\sigma}^C, \boldsymbol{K}^C\right) = 0 \tag{11}$$

where $\boldsymbol{K}^C$ has been found from $\boldsymbol{\kappa}^C$, which in turn has been found using (5) such that

$$\boldsymbol{\kappa}^C = \boldsymbol{\kappa}^A + \sum_{i=1}^{n} \alpha_i \int_{\lambda_i^A}^{\lambda_i^C} \boldsymbol{k}_i d\lambda_i \approx \boldsymbol{\kappa}^A + \sum_{i=1}^{n} \alpha_i \Delta\lambda_i \boldsymbol{k}_i|_C \tag{12}$$

5 STRAIN HARDENING HOEK-BROWN MODEL

5.1 *Basic premises*

In order to implement the strain hardening Hoek-Brown model, the above mentioned aspects must be accounted for. With tension taken as positive, the Hoek-Brown criterion of (1) can be rewritten

$$f = \sigma_{\max} - \sigma_{\min} - \sigma_{ci}\left(s - m_b \frac{\sigma_{\max}}{\sigma_{ci}}\right)^a = 0 \tag{13}$$

where $\sigma_{\max}$ is the largest principal stress and $\sigma_{\min}$ is the smallest principal stress. Equation (13) forms a six-sided pyramid with curved sides in principal stress space along the hydrostatic axis, which bounds the allowable stress states, as seen on figure 2.

The plastic potential function is assumed to take the form of the Hoek-Brown criterion as well, however, the parameters are different from those of f, thus

$$g = \sigma_{\max} - \sigma_{\min} - \sigma_{ci_g}\left(s_g - m_{b_g} \frac{\sigma_{\max}}{\sigma_{ci}}\right)^{a_g} \tag{14}$$

The hardening parameters are comprised of

$$\boldsymbol{K} = \{\sigma_{ci}, m_b, s, a, \sigma_{sci_g}, m_{b_g}, s_g, a_g\} \tag{15}$$

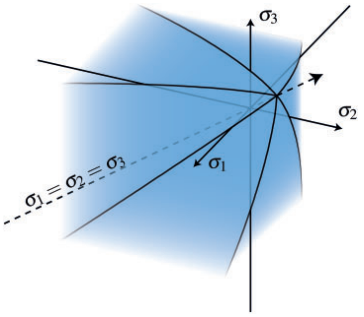

Figure 2. Sketch of Hoek-Brown criterion in principal stress space.

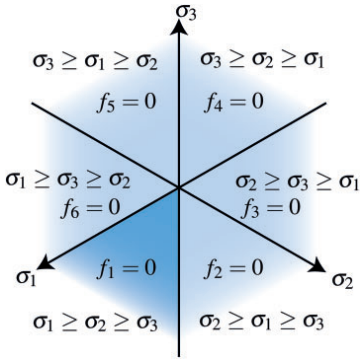

Figure 3. Sketch of Hoek-Brown criterion in principal stress space seen from the hydrostatic axis.

The state parameters, $\boldsymbol{\kappa}$, are assumed to be expressed by a single scalar value, $\overline{\varepsilon}^p$, called the accumulated plastic strain, which is assumed to evolve according to

$$d\overline{\varepsilon}^p = \sum_{i=1}^{n} \alpha_i \, d\lambda_i \tag{16}$$

i.e. $\boldsymbol{k}_i(\boldsymbol{\sigma}, \boldsymbol{K})$ is assumed to be 1, cf. (5). Thus, the change in accumulated plastic strain is the sum of the plastic multipliers involved. The state of the hardening parameters, $\boldsymbol{K}$, are found based on an arbitrary user defined set of points

$$\left(\overline{\varepsilon}_1^p, \boldsymbol{K}_1\right), \ \ldots, \ \left(\overline{\varepsilon}_k^p, \boldsymbol{K}_k\right) \tag{17}$$

Thus, the hardening parameters are found by linear interpolation between these points. If $\overline{\varepsilon}^p$ exceeds $\overline{\varepsilon}_k^p$, the hardening parameters are set according to the last point, and perfect plasticity is assumed during further plastic straining. Using this method, the model is able to simulate different kinds of behaviour, including elastic-brittle, strain hardening, strain softening and elastic-perfectly-plastic behaviour.

The return mapping scheme is carried out in principal stress space. This reduces the unknowns of $\boldsymbol{\sigma}^C$ from six to only three components, which can be visualized in a 3D space, and thus geometrical arguments can be applied. The predicted stress state, $\boldsymbol{\sigma}^B$, is thus transformed to principal stress space, denoted $\overline{\boldsymbol{\sigma}}^B$, and the corresponding updated stress state in principal stress space, $\overline{\boldsymbol{\sigma}}^C$, is found, which is then converted back to the original coordinate system, giving the updated stress state, $\boldsymbol{\sigma}^C$, that is of interest in the FE-model.

5.2 *Yield criterion regions*

Figure (3) shows the Hoek-Brown criterion seen from the hydrostatic axis.

If by definition we state that $\sigma_1 \geq \sigma_2 \geq \sigma_3$, when we transform $\boldsymbol{\sigma}^B$ to $\overline{\boldsymbol{\sigma}}^B$, then only surface f_1, f_2 and f_6 are of interest. There are four possible locations of the updated stress state. Either the stress state lies on surface f_1, the intersection between f_1 and f_2, the intersection between f_1 and f_6 or the intersection of f_1, f_2 and f_6, known as the apex. Even though the apex point is comprised of all six yield criteria, only three of them are needed to form a basis for the plastic strains. Thus, we are dealing with three yield functions

$$f_1 = \sigma_1 - \sigma_3 - \sigma_{ci}\left(s - m_b\frac{\sigma_1}{\sigma_{ci}}\right)^a = 0 \tag{18}$$

$$f_2 = \sigma_2 - \sigma_3 - \sigma_{ci}\left(s - m_b\frac{\sigma_2}{\sigma_{ci}}\right)^a = 0 \tag{19}$$

$$f_6 = \sigma_1 - \sigma_2 - \sigma_{ci}\left(s - m_b\frac{\sigma_1}{\sigma_{ci}}\right)^a = 0 \tag{20}$$

with the appertaining plastic potentials g_1, g_2 and g_6. Because the updated stress state can be situated at four different locations, four different return algorithms are required. However, before they can be put to use, it must first be clarified, which one to use for a given predictor stress state.

This is handled in a similar fashion to Clausen & Damkilde (2008), with the use of boundary planes. By evaluating (9) along the boundaries of each yield criterion, the principal stress space is divided into regions. The updated stress state of a given predictor stress state belongs to the yield criteria f_i, where $\boldsymbol{s}_i$ define the region, in which the predictor stress state is located.

For the Hoek-Brown model, $\boldsymbol{s}_1$ is given by

$$\boldsymbol{s}_1 = \frac{E}{(1+\nu)(1-2\nu)}\begin{Bmatrix}(1-\nu)k_g - \nu \\ \nu k_g - \nu \\ \nu k_g - 1 + \nu\end{Bmatrix} \tag{21}$$

where

$$k_g = \frac{\partial g_1}{\partial \sigma_1} = 1 + a_g m_{b_g}\left(s_g - m_{b_g}\frac{\sigma_1}{\sigma_{ci_g}}\right)^{a_g - 1} \tag{22}$$

similarly $\boldsymbol{s}_2$ and $\boldsymbol{s}_3$ is given by

$$\boldsymbol{s}_2 = \left\{ s_{1,2},\ s_{1,1},\ s_{1,3} \right\}^T,\ \boldsymbol{s}_3 = \left\{ s_{1,1},\ s_{1,3},\ s_{1,2} \right\}^T \quad (23)$$

where $s_{1,k}$ is the k'th component of $\boldsymbol{s}_1$. From (21) and (22), it is seen, that $\boldsymbol{s}_i$ only depend on σ_1.

If perfect plasticity is assumed, the boundaries given by $\boldsymbol{s}_i$ does not change during plastic flow. However, if hardening plasticity is applied, the boundaries of each criteria as well as $\boldsymbol{s}_i$ change as the hardening parameters change. Since the hardening parameters of the updated stress state, $\boldsymbol{K}^C$, is unknown, these boundaries are also unknown. Nonetheless, by evaluating $\boldsymbol{s}_i$ with the initial hardening parameters, $\boldsymbol{K}^A$, the correct return algorithm can be estimated and applied. The resulting updated stress state and hardening parameters can then be used to check, whether the correct return algorithm has been employed. This is done if any of the return algorithms fail to converge. The new boundaries are calculated using the hardening parameters of the last iteration, $\boldsymbol{K}_l^C$, and if the predictor stress state has fallen into a new region, that return algorithm is applied. If that is not the case, then it is suggested to decrease the load step of the global finite element calculations and try again.

5.3 *Return to f_1*

If the predictor stress state is believed to return to $f_1 = 0$, then only one plastic multiplier is in play and only $\alpha_1 = 1$. This leads to four unknowns, namely the three principal stresses $\overline{\boldsymbol{\sigma}}^C$ and $\Delta\lambda_1$, which is sufficient to compute the accumulated plastic strain, $\overline{\varepsilon}^p$, and the updated hardening parameters. The solution is required to obey

$$\sigma_1^C = \sigma_1^B - \Delta\lambda_1 s_{1,1} \quad (24)$$

$$\sigma_2^C = \sigma_2^B - \Delta\lambda_1 s_{1,2} \quad (25)$$

$$\sigma_3^C = \sigma_3^B - \Delta\lambda_1 s_{1,3} \quad (26)$$

$$f_1\left(\overline{\boldsymbol{\sigma}}^C, \boldsymbol{K}^C\right) = 0 \quad (27)$$

cf. (10) and (11). However, since $\boldsymbol{s}_1$ only depends upon σ_1^C, the unknowns σ_2^C and σ_3^C are known once σ_1^C is known cf. (25) and (26). Thus we only need two equations, and with a little rewriting of (24), we obtain

$$\sigma_1^C - \sigma_1^B + \Delta\lambda_1 s_{1,1} = 0 \quad (28)$$

$$f_1\left(\overline{\boldsymbol{\sigma}}^C, \boldsymbol{K}^C\right) = 0 \quad (29)$$

This system of equations is solved using a Newton-Raphson iteration scheme, where

$$\boldsymbol{R}_l = \begin{Bmatrix} \sigma_{1,l}^C - \sigma_1^B + \Delta\lambda_{1,l} s_{1,1} \\ f_1\left(\overline{\boldsymbol{\sigma}}_l^C, \boldsymbol{K}_l^C\right) \end{Bmatrix} \quad (30)$$

until $|\mathrm{norm}(\boldsymbol{R}_l)| < \mathrm{TOL}$, where TOL is the required tolerance. $\boldsymbol{K}_l^C$ is interpolated from the points of (17) based on $\overline{\varepsilon}_l^{p,C}$ given by

$$\overline{\varepsilon}_l^{p,C} = \overline{\varepsilon}^{p,A} + \Delta\lambda_{1,l} \quad (31)$$

To start the iterations, an initial guess is needed. $\sigma_{1,0}^C$ is based on the σ_1 value that would fulfill (18) if $\sigma_3 = \sigma_3^B$ and $\Delta\lambda_{1,0}$ is assumed equal to 0. If $\sigma_{1,l+1}^C$ exceeds the current apex of the yield criteria, a fail safe is adapted in which

$$\sigma_{1,l+1}^C = \rho\,\sigma_{a,l+1}^C + (1-\rho)\,\sigma_{1,l}^C \quad (32)$$

where $\sigma_{a,l+1}^C$ is the current apex of the Hoek Brown criterion based on $\boldsymbol{K}_{l+1}^C$, and $\rho = 0.99$.

The solution of (28) and (29) does not ensure that $\sigma_1^C \geq \sigma_2^C \geq \sigma_3^C$. The solution is thus checked to ensure this. If it turns out that $\sigma_2^C > \sigma_1^C$, the return to f_1 & f_2 is applied. If $\sigma_3^C > \sigma_2^C$, the return to f_1 & f_6 is applied.

5.4 *Return to f_1 & f_2*

If the updated stress state resides on the intersection between f_1 and f_2, where $\sigma_1 = \sigma_2$, then two yield criteria are active, $\alpha_1 = \alpha_2 = 1$, and two multipliers, $\Delta\lambda_1$ and $\Delta\lambda_2$, are needed. Based on a similar procedure as the f_1 return, it ends up in three equations, with three unknowns

$$\sigma_1^C - \sigma_1^B + \Delta\lambda_1 s_{1,1} + \Delta\lambda_2 s_{2,1} = 0 \quad (33)$$

$$\sigma_1^C - \sigma_2^B + \Delta\lambda_1 s_{1,2} + \Delta\lambda_2 s_{2,2} = 0 \quad (34)$$

$$f_1\left(\overline{\boldsymbol{\sigma}}^C, \boldsymbol{K}^C\right) = 0 \quad (35)$$

Note that (34) corresponds to $\sigma_1^C = \sigma_2^C$, which ensures that $f_2(\overline{\boldsymbol{\sigma}}^C, \boldsymbol{K}^C) = 0$. This system is solved in a similar manner to the system of the f_1 return.

5.5 *Return to f_1 & f_6*

If the updated stress state resides on the intersection between f_1 and f_6, where $\sigma_2 = \sigma_3$, then two yield criteria are active, $\alpha_1 = \alpha_6 = 1$, and two multipliers, $\Delta\lambda_1$ and $\Delta\lambda_6$, are needed. Based on a similar procedure as above, it ends up in three equations, with three unknowns

$$\sigma_1^C - \sigma_1^B + \Delta\lambda_1 s_{1,1} + \Delta\lambda_6 s_{6,1} = 0 \quad (36)$$

$$\sigma_3^C - \sigma_2^B + \Delta\lambda_1 s_{1,2} + \Delta\lambda_6 s_{6,2} = 0 \quad (37)$$

$$f_1\left(\overline{\boldsymbol{\sigma}}^C, \boldsymbol{K}^C\right) = 0 \quad (38)$$

Again (37) corresponds to $\sigma_2^C = \sigma_3^C$, which ensures that $f_6(\overline{\boldsymbol{\sigma}}^C, \boldsymbol{K}^C) = 0$.

5.6 *Return to f_1, f_2 & f_6*

The return algorithm where the updated stress state resides on the apex, is comprised of three active yield criteria, f_1, f_2 and f_6, $\alpha_1 = \alpha_2 = \alpha_6 = 1$, and thus three plastic multipliers are also needed, $\Delta\lambda_1$, $\Delta\lambda_2$ and $\Delta\lambda_6$. However, the return algorithm is a little different than the other algorithms, because the location of $\overline{\boldsymbol{\sigma}}^C$ is known to coincide with the intersection of the three active yield criteria, where $\sigma_1^C = \sigma_2^C = \sigma_3^C = \sigma_a^C$. The apex, σ_a^C, is known once $\boldsymbol{K}^C$ is known. Thus only the three equations of (10) are needed to solve the problem, i.e.

$$\sigma_a^C - \sigma_1^B + \Delta\lambda_1 s_{1,1} + \Delta\lambda_2 s_{2,1} + \Delta\lambda_3 s_{3,1} = 0 \tag{39}$$

$$\sigma_a^C - \sigma_1^B + \Delta\lambda_1 s_{1,2} + \Delta\lambda_2 s_{2,2} + \Delta\lambda_3 s_{3,2} = 0 \tag{40}$$

$$\sigma_a^C - \sigma_1^B + \Delta\lambda_1 s_{1,3} + \Delta\lambda_2 s_{2,3} + \Delta\lambda_3 s_{3,3} = 0 \tag{41}$$

If associated flow is assumed, the apex of the yield criteria and the plastic potentials coincide. Since the gradient of the plastic potential tends toward infinity on the apex, cf. (22), the plastic multipliers must approach zero in order to give finite strains. For this reason, perfect plasticity is assumed in the associated case with a return to the apex.

5.7 *Consistent constitutive matrices*

It can be shown, that the consistent constitutive matrix is given by

$$\boldsymbol{D}^{epc} = \boldsymbol{D}^c - \boldsymbol{D}^c \sum_{i=1}^{n}\sum_{k=1}^{n} \alpha_i \alpha_k \left(\boldsymbol{A}^{-1}\right)_{ik} \frac{\partial g_i}{\partial \boldsymbol{\sigma}} \left(\frac{\partial f_k}{\partial \boldsymbol{\sigma}}\right)^T \boldsymbol{D}^c \tag{42}$$

where $\boldsymbol{A}$ is the $n \times n$ matrix given by

$$A_{ik} = \alpha_i \alpha_k \left(\left(\frac{\partial f_i}{\partial \boldsymbol{\sigma}}\right)^T \boldsymbol{D}^c \frac{\partial g_k}{\partial \boldsymbol{\sigma}} + \left(\frac{\partial f_i}{\partial \boldsymbol{K}}\right)^T \frac{\partial \boldsymbol{K}}{\partial \overline{\boldsymbol{\varepsilon}}^p} \right) + (\alpha_i - 1)(\alpha_k - 1)\,\delta_{ik} \tag{43}$$

where $\boldsymbol{D}^c$ is the modified elastic stiffness matrix and δ_{ik} is the Kronecker delta. For further details see Clausen (2007) and Ottosen & Ristinmaa (2005). Once perfect plasticity is reached, the modified consistent constitutive matrices mentioned in Clausen (2007) is used in the calculations.

6 EXAMPLE: TUNNEL EXCAVATION

The numerical implementation is tested on a simulation of a tunnel excavation. The simulation models 1 m of a tunnel with a radius, r_T, of 10 m along the tunnel axis, z, using axissymmetry, cf. figure 4. The extend of the model reach out to $r_{BC} = 300$ m from the tunnel axis. The excavation is simulated by reducing the pressure, p, on the tunnel wall from the in-situ pressure, p_∞, to 0. The self weight of the rock material is neglected.

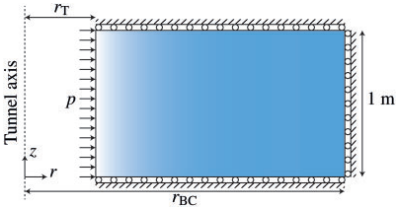

Figure 4. Sketch of the tunnel model.

Table 1. Hoek Brown parameters of tunnel rock mass material.

σ_{ci}	a	m_b	s	E	ν
80 MPa	0.51	2.01	0.0039	9 GPa	0.25
80 MPa	0.53	0.34	0	9 GPa	0.25

Table 2. Plastic potential parameters of tunnel rock mass material.

σ_{ci_g}	a_g	m_{b_g}	s_g
80 MPa	1.00	1.15	0
80 MPa	1.00	1.15	0

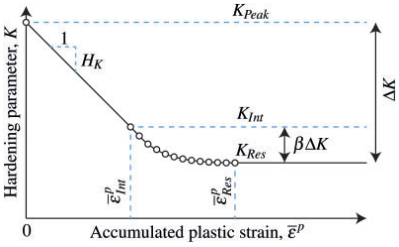

Figure 5. Evolution of the hardening parameters based on the accumulated plastic strain, $\overline{\varepsilon}^p$.

The parameters of the Hoek-Brown material are taken from example B of Sharan (2008). The parameters consists of peak parameters and residual parameters, cf. table 2. Notice however, that the numerical implementation is incapable of implementing the drop in Young's modulus described in Sharan (2008). Because of this, the peak modulus is assumed throughout the simulation, and the solution method in Sharan (2008) is utilized to get an analytical solution for an elastic-brittle rock material.

The plastic potential parameters are listed in table 2. These parameters result in non-associated flow and gives a constant dilation parameter, K_d, of 1.15, which makes comparing with the solution of Sharan (2008) possible.

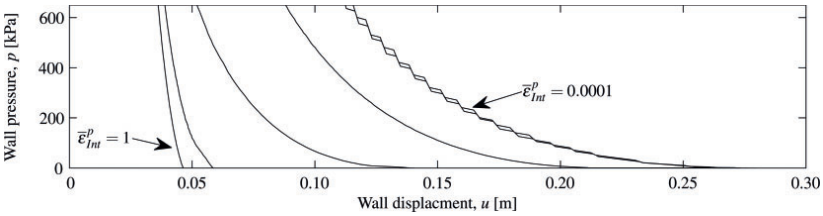

Figure 6. Tunnel wall movement, u, as a function of wall pressure, p. Notice that the curve for $\overline{\varepsilon}^p_{Int} = 0.0010$ and $\overline{\varepsilon}^p_{Int} = 0.0001$ almost overlap.

In the simulations, it is chosen, that during plastic straining, the hardening parameters drop from the peak parameters to the residual parameters according to figure 5.

As can be seen, the hardening parameters drop linearly from the peak value at zero plastic strain, to some intermediate value, K_{Int}, at some intermediate accumulated plastic strain, $\overline{\varepsilon}^p_{Int}$, followed by a non-linear evolution leading to perfect plasticity at $\overline{\varepsilon}^p_{Res}$. The intermediate value of the hardening parameter, K_{int}, is based on the parameter β, cf figure 5, which is set to 0.1. By setting the residual parameters equal to the peak parameters, perfect plasticity is achieved. The intermediate and residual accumulated plastic strains, $\overline{\varepsilon}^p_{Int}$ and $\overline{\varepsilon}^p_{Res}$, can be used to control the rate of softening. By letting these tend towards zero, an elastic-brittle behavior is achieved. $\overline{\varepsilon}^p_{Res}$ is chosen as $2\overline{\varepsilon}^p_{Int}$, and the simulation is performed for $\overline{\varepsilon}^p_{Int} = \{1; 0.1; 0.01; 0.005; 0.0025; 0.0010; 0.0001\}$, which spans an almost perfectly-plastic behavior, through strain softening to almost elastic-brittle behavior. Based on this, 300 points are calculated and used in the simulations, cf. (17). The model is meshed using 1600 linear-strain triangular elements with a gauss order of 13 and solved using a standard Newton-Raphson solution method with a maximum step length of $\Delta t = 5 \cdot 10^{-4}$, in order to get a detailed view of the equilibrium path, which can be seen on figure 6.

The analytical solution predicts a wall displacement of 0.0454 m in the elastic-perfectly-plastic case, and a wall displacement of 0.2789 m in the elastic-brittle case. The results from the finite element model results in a wall displacement between 0.0456 m and 0.2826 m respectively for $\overline{\varepsilon}^p_{Int} = 1$ and $\overline{\varepsilon}^p_{Int} = 0.0001$. A difference of 0.4% and 1.3% respectively. Further, the results of the simulations in between the elastic-perfectly-plastic and the elastic-brittle behaviour shows results between these two values, which is what would be expected.

The FE-simulations showed some mesh dependency, and the jagged nature of the more brittle rock simulations is believed to stem from a too coarse mesh. If the elastic predictor stress state falls just outside the yield surface, the yield surface shrinks very rapidly, and thus a large plastic multiplier is needed, which leads to large plastic strains. If the mesh is coarse, each gauss point represents a large portion of the model, and thus large displacements are also expected. If a finer mesh is employed, each gauss point represents smaller portions of the model, and thus smaller and more continuous displacements are expected. However, if a finer mesh is employed, the global equilibrium iterations become troublesome. This could perhaps be due to the stability issues surrounding numerical non-associated plasticity.

7 CONCLUSION

A strain hardening Hoek-Brown material model has been developed, which is capable of modeling many aspects of the observed behavior of jointed rock masses. A total of eight parameters are allowed to evolve based on the accumulated plastic strains. The model has been deployed on a FE-simulation of a tunnel excavation utilizing non-associated plasticity and the results obtained are in good agreement with the analytical solutions, however, some mesh dependency was observed.

REFERENCES

Clausen, J. (2007). *Efficient Non-Linear Finite Element Implementation of Elasto-Plasticity for Geotechnical Problems*. Ph. D. thesis, Computational Mechanics, Esbjerg Institute of Technology, Aalborg University Esbjerg. http://vbn.aau.dk/files/14058639/JCthesis.pdf.

Clausen, J. & L. Damkilde (2008). An exact implementation of the Hoek-Brown criterion for elasto-plastic finite element calculations. *International Journal of Rock Mechanics & Mining Sciences 45*, 831–847.

de Souza Neto, E., D. Perić, & D. Owen (2008). *Computational Methods for Plasticity*. London: Wiley.

Hoek, E. & E. T. Brown (1997). Practical estimates of rock mass strength. *Internation Journal of Rock Mechanics & Mining Sciences 34*, 1165–1186.

Hoek, E., C. Carranza-Torres, & B. Corkum (2002). Hoek-Brown failure criterion – 2002 edition. *Proc. NARMS-TAC Conference, Toronto 1*, 267–273.

Hoek, E. & M. S. Diederichs (2006). Empirical estimation of rock mass modulus. *Internation Journal of Rock Mechanics & Mining Sciences 43*, 203–215.

Ottosen, N. S. & M. Ristinmaa (2005). *The Mechanics of Constitutive Modeling*. London: Elsevier.

Sharan, S. (2008). Analytical solutions for stress and displacements around a circular opening in a generalized Hoek-Brown rock. *International Journal of Rock Mechanics & Mining Sciences 45*, 78–85.

Paper B

Finite element implementation of the Hoek–Brown material model with general strain softening behavior

E. S. Sørensen, J. Clausen & L. Damkilde

The paper has been published in
International Journal of Rock Mechanics and Mining Sciences Vol. 78,
pp. 163–174, 2015.

International Journal of Rock Mechanics & Mining Sciences 78 (2015) 163–174

Contents lists available at ScienceDirect

International Journal of Rock Mechanics & Mining Sciences

journal homepage: www.elsevier.com/locate/ijrmms

Finite element implementation of the Hoek–Brown material model with general strain softening behavior

E.S. Sørensen*, J. Clausen, L. Damkilde

Department of Civil Engineering, Aalborg University, Sofiendalsvej 11, 9000 Aalborg, Denmark

ARTICLE INFO

Article history:
Received 15 October 2014
Received in revised form
4 May 2015
Accepted 21 May 2015

Keywords:
Hoek–Brown criterion
Rock mass
Strain softening
Return mapping

ABSTRACT

A numerical implementation of the Hoek–Brown criterion is presented, which is capable of modeling different post-failure behaviors observed in jointed rock mass. This is done by making the material parameters a function of the accumulated plastic strain. The implementation is for use in finite element calculations, and is based on the return mapping framework. The updated stress state together with the consistent constitutive matrix is found in principal stress space based on the principles of boundary planes. The implementation is verified through the simulation of a tunnel excavation for perfectly-plastic, brittle and strain softening material behavior and the results are compared with known solutions.

1. Introduction

When dealing with rock mass modeling, the preferred material model is the Hoek–Brown model first introduced by Hoek and Brown [1] and subsequently refined to its current form given in Hoek et al. [2]. This model is available in an elastic–perfectly-plastic version in various commercial finite element programs. However, according to Hoek and Brown [3], the post-failure behavior is only believed to mimic perfect plasticity for very poor quality rock masses. Rock masses of greater quality are suggested to experience either a brittle or strain softening behavior when exposed to plastic straining.

Currently, this constrains the use of the Hoek–Brown model, which is often disregarded in favor of an approximated Mohr–Coulomb model able to incorporate such post-failure behavior when needed. As an alternative, the elastic–perfectly-plastic Hoek–Brown model can be used with a parameter set believed to be representative for the entire rock mass of the problem at hand. However, both methods have significant shortcomings, which might result in over-sized or unsafe structures.

Based on the framework of elasto-plasticity, a strain softening Hoek–Brown model is developed for use in finite element analyses. The model is able to behave in a user defined way including hardening, softening, perfect plasticity as well as brittle behavior.

First, the Hoek–Brown failure criterion is introduced, followed by a brief description of the relevant equations within the elasto-plastic framework. Then follows the derivation and implementation of the strain hardening model. Finally, the model is applied to a tunnel excavation simulation with various material behavior. The work presented here is a further development of Sørensen et al. [4]. The problems of bifurcation and strain localization which are associated with strain softening will not be accounted for, since it is a subject in itself.

2. Rock mass behavior and the Hoek–Brown criterion

Rock material is a wide expression used to describe a solid made up of minerals. Depending on the size of a rock sample, see Fig. 1, rock material typically ranges from isotropic intact rock mass without any discontinuities, through very anisotropic rock mass with a few dominating discontinuities, to an isotropic jointed rock mass with a large number of randomly oriented evenly spaced discontinuities with the same characteristics [5].

If a representative sample of the rock material can be regarded as either intact rock or as jointed rock mass, then the material can be regarded as isotropic, provided that the size of the representative sample is small compared to some characteristic length of the problem. If the discontinuities of the sample are oriented in a non-random order, it might be necessary to model the rock material as an anisotropic continuum. If large fractures (faults) dominate the construction site of the structure, it may also be necessary to include such fractures explicitly in the model. In the following, it is assumed that the rock material can be modeled

* Corresponding author. Tel.: +45 99 40 85 67.
E-mail addresses: ess@civil.aau.dk (E.S. Sørensen), jc@civil.aau.dk (J. Clausen), lda@civil.aau.dk (L. Damkilde).

http://dx.doi.org/10.1016/j.ijrmms.2015.05.005
1365-1609/

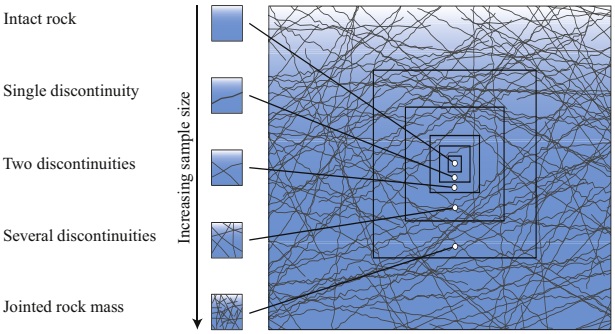

Fig. 1. Depending on the sample size, rock mass ranges from intact to jointed rock mass. Inspired by Hoek [5].

as an isotropic continuum. In order to be able to include rock material in finite element models, the properties of the rock material need to be known and somehow quantified. Extensive empirical research has lead to the formulation of the generalized Hoek–Brown criterion, Eq. (1), which predicts the stress states that cause failure in rock materials [2]

$$\sigma_1' = \sigma_3' + \sigma_{ci}\left(m_b\frac{\sigma_3'}{\sigma_{ci}} + s\right)^a \tag{1}$$

σ_1' and σ_3' are the major and minor effective principal stresses respectively, where compression is taken as positive. As the criterion suggests, four parameters are needed in order to assess the strength of the rock material, namely the uniaxial compressive strength of the intact rock material, σ_{ci}, and the constants m_b, s and a. The constants can be estimated based on the Geological Strength Index (GSI), the disturbance factor, D, and the intact rock material constant, m_i, by using the following expressions [2]:

$$m_b = m_i\ \exp\left(\frac{\mathrm{GSI}-100}{28-14D}\right) \tag{2}$$

$$s = \exp\left(\frac{\mathrm{GSI}-100}{9-3D}\right) \tag{3}$$

$$a = \frac{1}{2} + \frac{1}{6}\left(\exp\left(\frac{-\mathrm{GSI}}{15}\right) - \exp\left(\frac{-20}{3}\right)\right) \tag{4}$$

The Geological Strength Index is a measure of the rock material's quality based on field observations, which takes into account the composition and structure of the in situ rock material as well as the surface conditions. Based on this, the GSI is assigned on a scale ranging from 0 to 100, where 100 indicates a very good quality [6,7].

The disturbance factor, D, is used to take into account the blast damage that part of the rock material might suffer from. It ranges from 0 to 1, where 0 indicates undisturbed rock material. The material constant m_i and the uniaxial compressive strength of the intact rock material, σ_{ci}, are found using laboratory tests on the intact rock material. The elastic modulus of the rock material can be estimated by [8]

$$E_{rm} = 100,000\ \mathrm{MPa}\left(\frac{1-D/2}{1+\exp((75+25D-\mathrm{GSI})/11)}\right) \tag{5}$$

Once the rock material has reached a stress state which causes failure, it loses some of its strength, as mentioned previously. The manner in which the strength drops is not entirely determined, but three possible characteristics are mentioned in Hoek and Brown [3]. It is believed that very good quality hard rock masses undertake an elastic-brittle behavior, where the strength of the rock material rapidly drops to some residual strength once the failure criterion is reached, see Fig. 2a. Average quality rock mass is assumed to show a strain softening relationship between the strength of the material and the plastic straining which it undergoes, see Fig. 2b.Very poor quality rock mass behaves in an elastic–perfectly plastic way, see Fig. 2c. For an implementation of an elastic–perfectly plastic exact Hoek–Brown criterion see Clausen

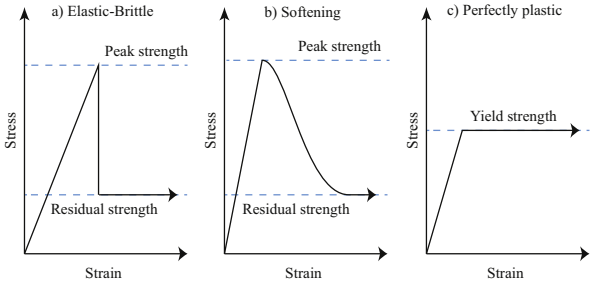

Fig. 2. Post-failure rock mass behavior.

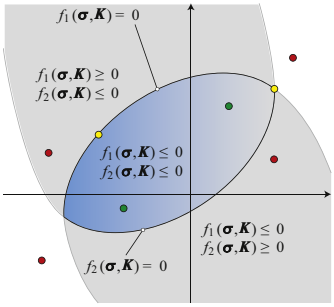

Fig. 3. Sketch of two yield functions f_1 and f_2. Each colored dot represents a combination of a stress state, $\boldsymbol{\sigma}$ and a set of hardening parameters, $\boldsymbol{K}$, ($\boldsymbol{\sigma}$, $\boldsymbol{K}$), which is either elastic (green), plastic (yellow) or inadmissible (red). (For interpretation of the references to color in this figure caption, the reader is referred to the web version of this paper.)

and Damkilde [9].

3. Plasticity fundamentals

The basic theory behind plasticity relies on one or more yield functions, $f_1, \ldots, f_n$, which are scalar functions of the stress state, $\boldsymbol{\sigma}$, and some hardening parameters, $\boldsymbol{K}$. Plastic strains start to develop once the material reaches its yielding limit, which is defined by the yield criteria

$$f_i(\boldsymbol{\sigma}, \boldsymbol{K}) = 0, \quad i = 1, \ldots, n \tag{6}$$

Any combination of $\boldsymbol{\sigma}$ and $\boldsymbol{K}$ resulting in negative values of all yield functions are elastic stress states, as shown with the green points in Fig. 3. Any combination resulting in a positive value of any of the functions is inadmissible, as shown by the red points, and any combination of $\boldsymbol{\sigma}$ and $\boldsymbol{K}$ fulfilling one or more of the criteria leads to additional plastic straining, as shown by the yellow points.

The manner in which the plastic strains develop is governed by the plastic potential functions, $g_1, \ldots, g_n$, which are also functions of $\boldsymbol{\sigma}$ and $\boldsymbol{K}$, and the non-negative plastic multipliers $\lambda_1, \ldots, \lambda_n$, such that [10]

$$d\boldsymbol{\varepsilon}^p = \sum_{i=1}^{n} d\lambda_i \frac{\partial g_i}{\partial \boldsymbol{\sigma}} = \sum_{i=1}^{n} d\lambda_i \boldsymbol{b}_i \tag{7}$$

where

$$\boldsymbol{b}_i = \frac{\partial g_i}{\partial \boldsymbol{\sigma}} \tag{8}$$

has been introduced for readability. The hardening parameters, $\boldsymbol{K}$, are functions of the state variables, $\boldsymbol{\kappa}$, that define the internal state of the material

$$\boldsymbol{K} = \boldsymbol{K}(\boldsymbol{\kappa}) \tag{9}$$

The evolution of the state variables is defined by the evolution law, which is also a function of $\boldsymbol{\sigma}$ and $\boldsymbol{K}$

$$d\boldsymbol{\kappa} = d\boldsymbol{\kappa}(\boldsymbol{\sigma}, \boldsymbol{K}) \tag{10}$$

Further it is required that

$$d\lambda_i f_i = 0, \quad d\lambda_i \geq 0, \quad f_i \leq 0 \tag{11}$$

must hold for all yield criteria. This means that either there is no plastic straining related to yield criterion i, such that $d\lambda_i = 0$ while $f_i \leq 0$, or there is plastic straining related to yield criterion i, giving $d\lambda_i \geq 0$ and $f_i = 0$, which results in the consistency condition

$$df_i = \left(\frac{\partial f_i}{\partial \boldsymbol{\sigma}}\right)^T d\boldsymbol{\sigma} + \left(\frac{\partial f_i}{\partial \boldsymbol{K}}\right)^T d\boldsymbol{K} = 0 \tag{12}$$

The yield criteria which are fulfilled, i.e. $f_i = 0$ and $d\lambda_i \geq 0$, are said to be active criteria, due to their contribution to plastic straining.

Further details of the FE-method and plasticity can be found in Ottosen and Ristinmaa [11], de Souza Neto et al. [12] and Clausen [13].

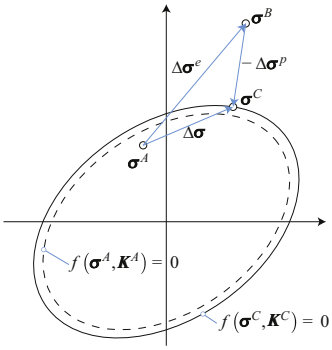

Fig. 4. Sketch of the updating scheme.

4. Return mapping

The numerical implementation relies on return mapping, which initially assumes that the strain increment, $\Delta\boldsymbol{\varepsilon}$, from the global FE equilibrium iterations, is entirely elastic, resulting in an elastic predictor stress increment

$$\Delta\boldsymbol{\sigma}^e = \boldsymbol{D}\Delta\boldsymbol{\varepsilon} \tag{13}$$

where $\boldsymbol{D}$ is the elastic constitutive matrix. Combining the initial stress state, $\boldsymbol{\sigma}^A$, with the elastic predictor increment results in a predicted elastic stress state

$$\boldsymbol{\sigma}^B = \boldsymbol{\sigma}^A + \Delta\boldsymbol{\sigma}^e \tag{14}$$

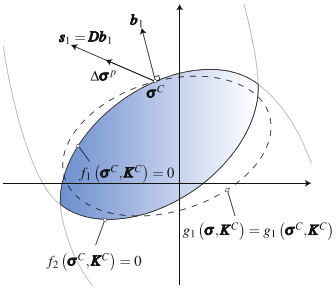

Fig. 5. Direction of the plastic corrector of a return with one active yield function in a model with two yield functions f_1 and f_2.

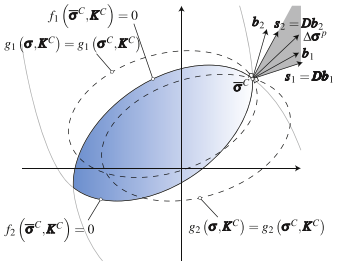

Fig. 6. Direction of the plastic corrector of a return with two active yield functions in a model with two yield functions f_1 and f_2.

If the evaluation of one or more of the yield criteria with this stress state and the initial hardening parameters, $\boldsymbol{K}^A$, results in a positive value, the stress state is inadmissible, cf. Fig. 4. Hence an updated stress state, $\boldsymbol{\sigma}^C$, needs to established. Further the strain increment must be composed of an elastic part, $\Delta\boldsymbol{\varepsilon}^e$, and a plastic part, $\Delta\boldsymbol{\varepsilon}^p$. By use of (7), the plastic strain increment is approximately given by

$$\Delta\boldsymbol{\varepsilon}^p=\sum_{i=1}^{n}\int_{\lambda_i^A}^{\lambda_i^C}\boldsymbol{b}_i\,d\lambda_i\approx\sum_{i=1}^{n}\Delta\lambda_i\boldsymbol{b}_i|_C \tag{15}$$

where implicit integration has been employed, as can be seen from $\boldsymbol{b}_i|_C$.

Since only the elastic strains contribute to the stress increment, $\boldsymbol{\sigma}^B$ needs to be corrected by an amount

$$\Delta\boldsymbol{\sigma}^p=\boldsymbol{D}\Delta\boldsymbol{\varepsilon}^p=\sum_{i=1}^{n}\Delta\lambda_i\boldsymbol{D}\boldsymbol{b}_i|_C=\sum_{i=1}^{n}\Delta\lambda_i\boldsymbol{s}_i \tag{16}$$

known as the plastic corrector. Further (11) results in the fact that $\Delta\lambda_i=0$ for all the yield criteria which are not active. Thus, the plastic corrector is some linear combination of the vectors

$$\boldsymbol{s}_i=\boldsymbol{D}\boldsymbol{b}_i|_C \tag{17}$$

given by each active yield surface, as illustrated in Fig. 5 in the case of one active yield surface and Fig. 6 in the case of two active yield surfaces.

In the general case, the updated stress state becomes

$$\boldsymbol{\sigma}^C=\boldsymbol{\sigma}^B-\Delta\boldsymbol{\sigma}^p=\boldsymbol{\sigma}^B-\sum_{i=1}^{n}\Delta\lambda_i\boldsymbol{s}_i \tag{18}$$

which according to (11) must fulfill

$$\Delta\lambda_i f_i(\boldsymbol{\sigma}^C,\boldsymbol{K}^C)=0,\quad \Delta\lambda_i\geq 0,\quad f_i(\boldsymbol{\sigma}^C,\boldsymbol{K}^C)\leq 0 \tag{19}$$

where $\boldsymbol{K}^C$ has been found from $\boldsymbol{\kappa}^C$, which in turn has been found using (10) such that

$$\boldsymbol{\kappa}^C=\boldsymbol{\kappa}^A+\int_{\boldsymbol{\kappa}^A}^{\boldsymbol{\kappa}^C}d\boldsymbol{\kappa}\approx\boldsymbol{\kappa}^A+\Delta\boldsymbol{\kappa} \tag{20}$$

5. Basis of strain hardening Hoek–Brown model

To implement the strain hardening Hoek–Brown model, the yield criteria, plastic potentials and evolution functions must be defined. With tension taken as positive, the Hoek–Brown criterion of (1) can be rewritten as

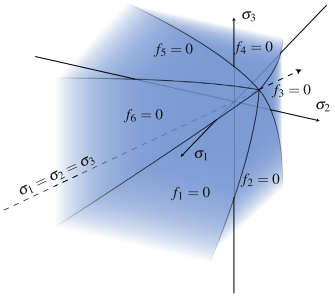

Fig. 7. Sketch of Hoek–Brown criterion in principal stress space.

$$f(\sigma_{\max},\sigma_{\min})=\sigma_{\max}-\sigma_{\min}-\sigma_{ci}\left(s-m_b\frac{\sigma_{\max}}{\sigma_{ci}}\right)^a=0 \tag{21}$$

where $\sigma_{\max}$ is the largest principal stress and $\sigma_{\min}$ is the smallest principal stress. The primes denoting effective stresses have been omitted for readability, and are implied during the rest of the paper. Eq. (21) is an isotropic non-linear pressure dependent criterion. The visualization of Eq. (21) in principal stress space is shown in Fig. 7. As can be seen, the allowable stress states are bounded by a six-sided pyramid with curved surfaces in principal stress space along the hydrostatic axis made up of six yield criteria, f_1-f_6, given by

$$\begin{aligned}&f_1=f(\sigma_1,\sigma_3)=0,\quad f_2=f(\sigma_2,\sigma_3)=0,\quad f_3=f(\sigma_2,\sigma_1)=0,\\&f_4=f(\sigma_3,\sigma_1)=0,\quad f_5=f(\sigma_3,\sigma_2)=0,\quad f_6=f(\sigma_1,\sigma_2)=0\end{aligned} \tag{22}$$

Due to symmetry, the apex is located on the hydrostatic axis, $\sigma_1=\sigma_2=\sigma_3=\sigma_a$, which gives

$$\sigma_a=\frac{s}{m_b}\sigma_{ci} \tag{23}$$

and sets the limit for the maximum allowable tension, that the rock mass is able to withstand. Further, for a given $\sigma_{\max}$,

$$\sigma_{\min}=\sigma_{\max}-\sigma_{ci}\left(s-m_b\frac{\sigma_{\max}}{\sigma_{ci}}\right)^a \tag{24}$$

satisfies the criterion.

In accordance with Clausen and Damkilde [9], the plastic potential function is chosen to take the form of the Hoek–Brown criterion as well, however, the parameters are different from those of f, thus

$$g=\sigma_{\max}-\sigma_{\min}-\sigma_{cig}\left(s_g-m_{bg}\frac{\sigma_{\max}}{\sigma_{cig}}\right)^{a_g} \tag{25}$$

resulting in g_1 to g_6 similar to Eq. (22), which gives the possibility of both associated and non-associated plasticity. Further, the parameters of the Hoek–Brown criterion can be chosen, such that a constant rate of dilation can be achieved, which e.g. is assumed in Sharan [14].

The hardening parameters are composed of

$$\boldsymbol{K}=\{\sigma_{ci},m_b,s,a,\sigma_{scig},m_{bg},s_g,a_g\} \tag{26}$$

The state parameters, $\boldsymbol{\kappa}$, are assumed to be expressed by a single scalar value, $\bar{\varepsilon}^p$, called the accumulated plastic strain, i.e.

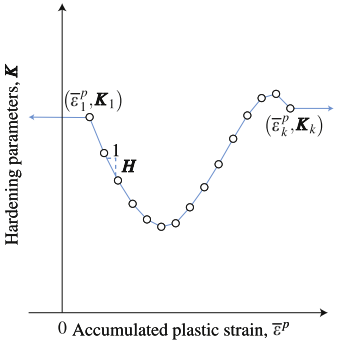

Fig. 8. Example of arbitrary $\bar{\varepsilon}^p - \boldsymbol{K}$ curve defined by a set of $(\bar{\varepsilon}^p, \boldsymbol{K})$ points. Perfect plasticity is assumed before and after the user defined points.

$$\boldsymbol{\kappa} = \{\bar{\varepsilon}^p\} \tag{27}$$

which is some function of the plastic strains

$$\bar{\varepsilon}^p = \bar{\varepsilon}^p(\boldsymbol{\varepsilon}^p) \tag{28}$$

Based on the choice of (28), the evolution law can be established cf. (10). Several different versions are used in the literature, but the following two are often seen:

$$d\bar{\varepsilon}^p = \sqrt{\frac{2}{3}(d\boldsymbol{\varepsilon}^p)^T d\boldsymbol{\varepsilon}^p} \quad \text{or} \quad d\bar{\varepsilon}^p = d\gamma^p = d\varepsilon_1^p - d\varepsilon_3^p \tag{29}$$

The return algorithm is capable of handling any choice of (28), as long as the necessary derivatives can be established. For further details, see Section 7 and Appendix A. The state of the hardening parameters, $\boldsymbol{K}$, are found based on an arbitrary user defined set of points

$$\{(\bar{\varepsilon}_1^p, \boldsymbol{K}_1), \ldots, (\bar{\varepsilon}_k^p, \boldsymbol{K}_k)\} \tag{30}$$

as shown in Fig. 8.

Thus, the hardening parameters are found by linear interpolation between these points. If $\bar{\varepsilon}^p$ is lower than the first user defined point, $\bar{\varepsilon}_1^p$, or bigger than the last defined point, $\bar{\varepsilon}_k^p$, the hardening parameters are set according to $\boldsymbol{K}_1$ and $\boldsymbol{K}_k$ respectively. Thus perfect plasticity is assumed before and after the user defined points. Using this method, the model is able to simulate different kinds of behavior, including elastic-brittle, strain hardening, strain softening and elastic–perfectly-plastic behavior.

The return mapping scheme is carried out in principal stress space. This reduces the unknowns of $\boldsymbol{\sigma}^C$ from six to only three components, which can be visualized in a 3D space, and thus geometrical arguments can be applied, see Clausen et al. [15]. The predicted stress state, $\boldsymbol{\sigma}^B$, is thus transformed to principal stress space, denoted $\bar{\boldsymbol{\sigma}}^B$, and the corresponding updated stress state in principal stress space, $\bar{\boldsymbol{\sigma}}^C$, is found, which is then converted back to the original coordinate system, giving the updated stress state, $\boldsymbol{\sigma}^C$, that is of interest in the FE-model.

6. Yield criterion regions

Fig. 9 shows the Hoek–Brown criterion seen from the hydrostatic axis. It is chosen that $\sigma_1 \geq \sigma_2 \geq \sigma_3$, when $\boldsymbol{\sigma}^B$ is transformed to $\bar{\boldsymbol{\sigma}}^B$, thus the lower left section of the stress space visualized in Fig. 9 is of primary interest together with the yield surface f_1. There are four possible locations of the updated stress state. Either the stress state lies on surface f_1, the intersection between f_1 and f_2 (known as the triaxial compressive meridian), the intersection between f_1 and f_6 (known as the triaxial tensile meridian), or at the apex, the intersection of all six yield surfaces, $f_1 - f_6$.

The intersection between f_1 and f_2 is a curve, $\boldsymbol{l}_1$, in principal stress space given by $\sigma_1 = \sigma_2$, which results in

$$\boldsymbol{l}_1 = \begin{Bmatrix} \sigma_1 \\ \sigma_2 \\ \sigma_3 \end{Bmatrix} = \begin{Bmatrix} \sigma_1 \\ \sigma_1 \\ \sigma_1 - \sigma_{ci}\left(s - m_b\dfrac{\sigma_1}{\sigma_{ci}}\right)^a \end{Bmatrix} \tag{31}$$

and similarly, the intersection, $\boldsymbol{l}_6$, between f_1 and f_6 is given by $\sigma_2 = \sigma_3$, resulting in

$$\boldsymbol{l}_6 = \begin{Bmatrix} \sigma_1 \\ \sigma_2 \\ \sigma_3 \end{Bmatrix} = \begin{Bmatrix} \sigma_1 \\ \sigma_1 - \sigma_{ci}\left(s - m_b\dfrac{\sigma_1}{\sigma_{ci}}\right)^a \\ \sigma_1 - \sigma_{ci}\left(s - m_b\dfrac{\sigma_1}{\sigma_{ci}}\right)^a \end{Bmatrix} \tag{32}$$

It is crucial for the return algorithm to know which of the four

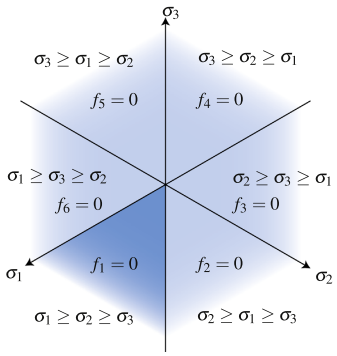

Fig. 9. Sketch of Hoek–Brown criterion in principal stress space seen from the hydrostatic axis.

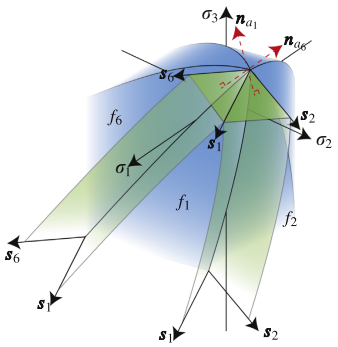

Fig. 10. Boundaries of the different regions of the yield criterion.

locations the updated stress state should reside on. This is handled in a similar fashion to Clausen and Damkilde [9], with the use of boundary planes.

By using Eq. (16), any updated stress state situated solely on f_1 results in a plastic corrector increment, $\Delta\boldsymbol{\sigma}^p$, which is in the direction of $\boldsymbol{s}_1$ given by

$$\boldsymbol{s}_1 = \begin{Bmatrix} s_{1,1} \\ s_{1,2} \\ s_{1,3} \end{Bmatrix} = \frac{E_{rm}}{(1+\nu)(1-2\nu)} \begin{Bmatrix} (1-\nu)k_g - \nu \\ \nu k_g - \nu \\ \nu k_g - 1 + \nu \end{Bmatrix} \tag{33}$$

where ν is Poisson's ratio and k_g is given by

$$k_g = \frac{\partial g_1}{\partial \sigma_1} = 1 + a_g m_{b_g} \left(s_g - m_{b_g} \frac{\sigma_1}{\sigma_{cig}} \right)^{a_g - 1} \tag{34}$$

By evaluating $\boldsymbol{s}_1$ along the boundaries of f_1, a region with all the possible predictor stress states belonging exclusively to the f_1 yield surface is identified. Similarly, by evaluating $\boldsymbol{s}_1$ and $\boldsymbol{s}_2$ along the $f_1 - f_2$ intersection, $\boldsymbol{l}_1$, the predictor stress states belonging to $\boldsymbol{l}_1$ can be established. The same arguments apply for stress states belonging to $\boldsymbol{l}_6$, see Fig. 10.

From this figure, it is also seen that the boundary separating the $\boldsymbol{l}_1$ region and the apex consists of the plane spanned by $\boldsymbol{s}_1$ and $\boldsymbol{s}_2$ evaluated at the apex, which results in the normal

$$\boldsymbol{n}_{a1} = \boldsymbol{s}_1 \times \boldsymbol{s}_2 \tag{35}$$

where $\times$ denotes the cross product. Similarly, the boundary separating $\boldsymbol{l}_6$ from the apex is a plane spanned by $\boldsymbol{s}_1$ and $\boldsymbol{s}_6$ with a normal given by

$$\boldsymbol{n}_{a6} = \boldsymbol{s}_6 \times \boldsymbol{s}_1 \tag{36}$$

A complicating factor is that the boundaries are made up of the directions given by $\boldsymbol{s}_1$, $\boldsymbol{s}_2$ and $\boldsymbol{s}_6$ as well as the location of $\boldsymbol{l}_1$, $\boldsymbol{l}_6$ and σ_a which are all dependent on the hardening parameters, $\boldsymbol{K}$, and thus dependent upon the state parameter $\bar{\varepsilon}^p$, which is not known beforehand. Another difficulty arises due to the fact that the boundaries separating f_1 from $\boldsymbol{l}_1$ and $\boldsymbol{l}_6$ are non-linear and it is computationally expensive to determine $\bar{\boldsymbol{\sigma}}^B$ relative to these boundaries.

Due to these complications, it is more difficult to estimate the correct return algorithm beforehand than it is to verify afterwards. Suppose that the updated state parameter, $\bar{\varepsilon}^{p,C}$, together with the updated stress state, $\bar{\boldsymbol{\sigma}}^C$, has been found in some way.

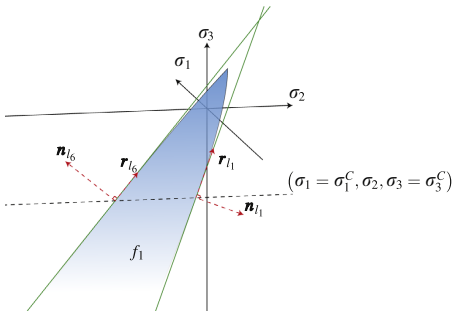

Fig. 11. The boundaries (in green) separating f_1 from $\boldsymbol{l}_1$ and $\boldsymbol{l}_6$ evaluated at $(\sigma_1^C, \sigma_2^C, \sigma_3^C)$ and $(\sigma_1^C, \sigma_2^C, \sigma_3^C)$ respectively. The viewing angle is such that $\boldsymbol{s}_1$ is directed towards the viewer, and is thus not visible in the figure. (For interpretation of the references to color in this figure caption, the reader is referred to the web version of this paper.)

Table 1
Schematic of region estimation.

Criteria	Update should stem from
$\boldsymbol{n}_{a1}^T(\bar{\boldsymbol{\sigma}}^B - \boldsymbol{\sigma}_a) > 0$ and $\boldsymbol{n}_{a6}^T(\bar{\boldsymbol{\sigma}}^B - \boldsymbol{\sigma}_a) > 0$	Apex
$\boldsymbol{n}_{l1}^T(\bar{\boldsymbol{\sigma}}^B - \boldsymbol{\sigma}_{l1}) > 0$	$\boldsymbol{l}_1$
$\boldsymbol{n}_{l6}^T(\bar{\boldsymbol{\sigma}}^B - \boldsymbol{\sigma}_{l6}) > 0$	$\boldsymbol{l}_6$
Otherwise	f_1

It can easily be clarified whether the updated stress state should stem from a return to the apex, since $\bar{\boldsymbol{\sigma}}^B$ should be located above the planes given by the normals $\boldsymbol{n}_{a1}$ and $\boldsymbol{n}_{a6}$, see Fig. 10. Since the boundaries go through the apex, $\boldsymbol{\sigma}_a = (\sigma_a, \sigma_a, \sigma_a)$, this is the case if

$$\boldsymbol{n}_{a1}^T(\bar{\boldsymbol{\sigma}}^B - \boldsymbol{\sigma}_a) > 0 \quad \text{and} \quad \boldsymbol{n}_{a6}^T(\bar{\boldsymbol{\sigma}}^B - \boldsymbol{\sigma}_a) > 0 \tag{37}$$

In order to investigate whether the updated stress state should stem from a return exclusively to f_1, the boundary separating f_1 from $\boldsymbol{l}_1$ is evaluated at $\boldsymbol{\sigma}_{l1} = (\sigma_1^C, \sigma_2^C, \sigma_3^C)$ and the boundary separating f_1 from $\boldsymbol{l}_6$ is evaluated at $\boldsymbol{\sigma}_{l6} = (\sigma_1^C, \sigma_2^C, \sigma_3^C)$. Together with the direction, $\boldsymbol{r}_{l1}$ and $\boldsymbol{r}_{l6}$ of $\boldsymbol{l}_1$ and $\boldsymbol{l}_6$ respectively at these locations, two planes are formed, see Fig. 11, given by the normals

$$\boldsymbol{n}_{l1} = \boldsymbol{r}_{l1} \times \boldsymbol{s}_1, \quad \boldsymbol{r}_{l1} = \begin{Bmatrix} 1 \\ 1 \\ k \end{Bmatrix}, \quad \boldsymbol{n}_{l6} = \boldsymbol{s}_1 \times \boldsymbol{r}_{l6}, \quad \boldsymbol{r}_{l6} = \begin{Bmatrix} 1 \\ k \\ k \end{Bmatrix} \tag{38}$$

where k is the f_1-equivalent to (34). If $\bar{\boldsymbol{\sigma}}^B$ is located "below" both these planes the update should stem from a return to f_1. This is the case if

$$\boldsymbol{n}_{l1}^T(\bar{\boldsymbol{\sigma}}^B - \boldsymbol{\sigma}_{l1}) < 0 \quad \text{and} \quad \boldsymbol{n}_{l6}^T(\bar{\boldsymbol{\sigma}}^B - \boldsymbol{\sigma}_{l6}) < 0 \tag{39}$$

If $\bar{\boldsymbol{\sigma}}^B$ is located above the plane spanned by $\boldsymbol{n}_{l1}$, the first inequality of (39) is not satisfied, and the updated stress state should stem from a return to $\boldsymbol{l}_1$. Similarly, if $\bar{\boldsymbol{\sigma}}^B$ is located above the plane spanned by $\boldsymbol{n}_{l6}$, the second inequality of (39) is not satisfied, and the updated stress state should stem from a return to $\boldsymbol{l}_6$. The different criteria are condensed in Table 1.

An advantage of the above procedure is that it is also able to give a fast prediction of which location the updated stress state should reside on, even for a solution that has been guessed upon. Thus for a given start guess of $\bar{\varepsilon}^{p,C}$ and $\bar{\boldsymbol{\sigma}}^C$, the guess can be improved upon based on the believed location of the updated stress state, and then checked again, to verify whether the used location was appropriate.

7. Return algorithm

The starting point of the algorithm is to make an initial guess of $\bar{\boldsymbol{\sigma}}^C$ and the plastic multipliers $\Delta\lambda_i$, which fulfill the requirements of (19). This guess is based on a return exclusively to the f_1 surface. Thus, the only plastic multiplier allowed to be non-zero is $\Delta\lambda_1$. However, since there is no readily available information about how much plastic straining develops, $\Delta\lambda_1 = 0$ is guessed upon, resulting in a plastic strain increment of zero. With this information, $\bar{\varepsilon}^{p,C} = \bar{\varepsilon}^{p,A}$ is implied giving $\boldsymbol{K}^C = \boldsymbol{K}^A$. Further, the guess must satisfy $f_1 = 0$. The value of $\sigma_3^C = \sigma_3^B$ is chosen. Since all the parameters of the yield criterion are given by $\boldsymbol{K}^A$, a legitimate guess of σ_1^C can be found by solving $f(\sigma_1^C, \sigma_3^B) = 0$, cf. (21) and (22). The last requirement is that f_2 through f_6 must be equal or below 0. This is

satisfied if $\sigma_1^C \geq \sigma_2^C \geq \sigma_3^C$. If σ_2^B fulfills this requirement, it is used as the initial guess of σ_2^C, if $\sigma_2^B \geq \sigma_1^C$ then $\sigma_2^C = \sigma_1^C$ is used and finally if $\sigma_2^B \leq \sigma_3^C$ then $\sigma_2^C = \sigma_3^C$ is used. The only thing left to check is the fulfillment of (18). Since the solution is only guessed upon, it cannot be expected to be satisfied. Thus the solution procedure centers around making the residual, $\boldsymbol{R}$, of this requirement zero, i.e.

$$\boldsymbol{R}(\bar{\boldsymbol{\sigma}}^C, \Delta\lambda_i) = \begin{Bmatrix} R_1 \\ R_2 \\ R_3 \end{Bmatrix} = \bar{\boldsymbol{\sigma}}^C - \bar{\boldsymbol{\sigma}}^B + \sum_{i=1}^{6} \Delta\lambda_i \boldsymbol{s}_i = \begin{Bmatrix} 0 \\ 0 \\ 0 \end{Bmatrix} \tag{40}$$

By using the procedure in Section 6 to find the likely location of the updated stress state, the guess of $\bar{\boldsymbol{\sigma}}^C$ and $\Delta\lambda_i$ can be improved upon based on one of the steps listed below. Then the new likely return region can be found and the guess can be improved upon again. This continues until $|\text{norm}(\boldsymbol{R}_l)| < \xi_R$, where ξ_R is the allowable tolerance.

7.1. Return to f_1

If the predictor stress state is believed to return to f_1, (40) simplifies to

$$R_1 = \sigma_1^C - \sigma_1^B + \Delta\lambda_1 s_{1,1} = 0 \tag{41}$$

$$R_2 = \sigma_2^C - \sigma_2^B + \Delta\lambda_1 s_{1,2} = 0 \tag{42}$$

$$R_3 = \sigma_3^C - \sigma_3^B + \Delta\lambda_1 s_{1,3} = 0 \tag{43}$$

As was the case of the starting guess, σ_1^C and σ_3^C are related through the requirement $f_1 = 0$. There is no exact requirements on σ_2^C except that $\sigma_1^C \geq \sigma_2^C \geq \sigma_3^C$, so an estimate can be found using (42) itself. Further, $\boldsymbol{s}_1$ only depends upon ${\sigma_1}^C$ and $\Delta\lambda_1$. Thus, the unknowns ${\sigma_2}^C$ and ${\sigma_3}^C$ are known once ${\sigma_1}^C$ and $\Delta\lambda_1$ are known.

An improved guess of σ_1^C and $\Delta\lambda_1$ can be found using a classic Newton–Raphson step on (41) and (43)

$$\begin{Bmatrix} \sigma_{1,k+1}^C \\ \Delta\lambda_{1,k+1} \end{Bmatrix} = \begin{Bmatrix} \sigma_{1,k}^C \\ \Delta\lambda_{1,k} \end{Bmatrix} + \begin{Bmatrix} d\sigma_1^C \\ d\Delta\lambda_1 \end{Bmatrix},$$
$$\begin{Bmatrix} d\sigma_1^C \\ d\Delta\lambda_1 \end{Bmatrix} = \begin{bmatrix} \frac{\partial R_1}{\partial \sigma_1^C} & \frac{\partial R_1}{\partial \Delta\lambda_1} \\ \frac{\partial R_3}{\partial \sigma_1^C} & \frac{\partial R_3}{\partial \Delta\lambda_1} \end{bmatrix}^{-1} \begin{Bmatrix} -R_{1,k} \\ -R_{3,k} \end{Bmatrix} \tag{44}$$

where k indicates the kth guess. The gradient of $\boldsymbol{R}$ is derived in Appendix A. In order to assure that $\Delta\lambda_1$ is positive, $\Delta\lambda_1$ is actually updated using

$$\Delta\lambda_{1,k+1} = \max(0, \Delta\lambda_{1,k} + d\Delta\lambda_1) \tag{45}$$

Afterwards, $\Delta\boldsymbol{e}^p$ is calculated based on $\sigma_{1,k}^C$, from the old guess, which in turn is used to calculate $\bar{\varepsilon}^p$ and $\boldsymbol{K}^C$. Based on this, it can be established, whether $\sigma_{1,k+1}^C$ is above the current apex of the Hoek Brown criterion. In such a case, a fail safe is adapted in which

$$\sigma_{1,k+1}^C = \mu\sigma_{a,k+1}^C + (1-\mu)\sigma_{1,k}^C \tag{46}$$

where $\sigma_{a,k+1}^C$ is the new apex based on the guess of $\boldsymbol{K}^C$ and $0 \leq \mu \leq 1$. If however the corrected $\sigma_{1,k+1}^C$ also is above the current apex, which could be the case during softening, then

$$\sigma_{1,k+1}^C = \sigma_{a,k+1}^C - \zeta \tag{47}$$

is used, where ζ is some small number depending on the precision of the computer. The implementation has shown very sensitive to how $\sigma_{1,k+1}^C$ is corrected, and the above solution has been the least troublesome of a variety of alternatives.

Afterwards, σ_3^C can be found so that $f_1 = 0$ is fulfilled. Finally σ_2^C is calculated using (42) and corrected so that the requirement $\sigma_1^C \geq \sigma_2^C \geq \sigma_3^C$ is fulfilled.

7.2. Return to $\boldsymbol{l}_1$

If the predictor stress state is believed to return to $\boldsymbol{l}_1$, where $\sigma_1 = \sigma_2$, then two yield criteria are active, and two multipliers, $\Delta\lambda_1$ and $\Delta\lambda_2$, are needed. Based on a similar procedure as the f_1 return, it ends up in three equations, with three unknowns

$$R_1 = \sigma_1^C - \sigma_1^B + \Delta\lambda_1 s_{1,1} + \Delta\lambda_2 s_{2,1} = 0 \tag{48}$$

$$R_2 = \sigma_2^C - \sigma_2^B + \Delta\lambda_1 s_{1,2} + \Delta\lambda_2 s_{2,2} = 0 \tag{49}$$

$$R_3 = \sigma_3^C - \sigma_3^B + \Delta\lambda_1 s_{1,3} + \Delta\lambda_2 s_{2,3} = 0 \tag{50}$$

Due to the fact that $\sigma_1 = \sigma_2$ on $\boldsymbol{l}_1$, $f_2(\bar{\boldsymbol{\sigma}}^C, \boldsymbol{K}^C) = 0$ is automatically satisfied if $f_1(\bar{\boldsymbol{\sigma}}^C, \boldsymbol{K}^C) = 0$ is satisfied, and further (48)–(50) can be simplified to give

$$R_1 = \sigma_1^C - \sigma_1^B + \Delta\lambda_1 s_{1,1} + \Delta\lambda_2 s_{1,2} = 0 \tag{51}$$

$$R_2 = \sigma_1^C - \sigma_2^B + \Delta\lambda_1 s_{1,2} + \Delta\lambda_2 s_{1,1} = 0 \tag{52}$$

$$R_3 = \sigma_3^C - \sigma_3^B + \Delta\lambda_1 s_{1,3} + \Delta\lambda_2 s_{1,3} = 0 \tag{53}$$

because

$$\boldsymbol{s}_2 = \begin{Bmatrix} s_{2,1} \\ s_{2,2} \\ s_{2,3} \end{Bmatrix} = \begin{Bmatrix} s_{1,2} \\ s_{1,1} \\ s_{1,3} \end{Bmatrix} \tag{54}$$

when $\sigma_1 = \sigma_2$. The system is solved for $d\sigma_1^C$, $d\Delta\lambda_1$ and $d\Delta\lambda_2$ in a similar manner to the system of the f_1 return.

7.3. Return to $\boldsymbol{l}_6$

If the predictor stress state is believed to return to $\boldsymbol{l}_6$, where $\sigma_2 = \sigma_3$, the two plastic multipliers, $\Delta\lambda_1$ and $\Delta\lambda_6$, are needed. Based on a similar procedure as above, it ends up in three equations, with three unknowns which can be written as

$$\sigma_1^C - \sigma_1^B + \Delta\lambda_1 s_{1,1} + \Delta\lambda_6 s_{1,1} = 0 \tag{55}$$

$$\sigma_3^C - \sigma_2^B + \Delta\lambda_1 s_{1,2} + \Delta\lambda_6 s_{1,3} = 0 \tag{56}$$

$$\sigma_3^C - \sigma_3^B + \Delta\lambda_1 s_{1,3} + \Delta\lambda_6 s_{1,2} = 0 \tag{57}$$

because

$$\boldsymbol{s}_6 = \begin{Bmatrix} s_{6,1} \\ s_{6,2} \\ s_{6,3} \end{Bmatrix} = \begin{Bmatrix} s_{1,1} \\ s_{1,3} \\ s_{1,2} \end{Bmatrix} \tag{58}$$

when $\sigma_2 = \sigma_3$. The system is solved for $d\sigma_1^C$, $d\Delta\lambda_1$ and $d\Delta\lambda_6$ as above.

7.4. Return to apex

The return algorithm where the updated stress state resides on the apex indicates that six yield criteria are active. However, three

criteria are enough to form a basis for the plastic corrector increment, $\Delta\boldsymbol{\sigma}^p$. Further, it is necessary that the plastic multipliers, $\Delta\lambda_i$, are positive. Thus, the three active yield criteria cannot be picked at random. To establish a possible solution, it is assumed that f_1 is active. If the previous guess was associated with a $\boldsymbol{I}_6$ – guess, then f_6 is also assumed active, otherwise f_2 is used. To find the third active yield criterion, the four remaining yield surfaces are tried one by one in the search for a solution that results in three positive plastic multipliers.

Because the location of $\bar{\boldsymbol{\sigma}}^C$ is known to coincide with the intersection of the three active yield criteria, where $\sigma_1^C = \sigma_2^C = \sigma_3^C = \sigma_a^C$, the apex, $\sigma_a{}^C$, is known once $\boldsymbol{K}^C$ is known. Thus only the three equations of (18) are needed to solve the problem, i.e.

$$\sigma_a^C - \sigma_1^B + \Delta\lambda_1 s_{1,1} + \Delta\lambda_x s_{x,1} + \Delta\lambda_y s_{y,1} = 0 \tag{59}$$

$$\sigma_a^C - \sigma_2^B + \Delta\lambda_1 s_{1,2} + \Delta\lambda_x s_{x,2} + \Delta\lambda_y s_{y,2} = 0 \tag{60}$$

$$\sigma_a^C - \sigma_3^B + \Delta\lambda_1 s_{1,3} + \Delta\lambda_x s_{x,3} + \Delta\lambda_y s_{y,3} = 0 \tag{61}$$

where x is either 2 or 6 and y is one of the remaining four. The system of equations is solved for $d\Delta\lambda_1$, $d\Delta\lambda_x$ and $d\Delta\lambda_y$.

8. Consistent constitutive matrices

In order to secure quadratic convergence of the global finite element iterations, the consistent constitutive matrix given by

$$\boldsymbol{D}^{epc} = \frac{\partial\Delta\boldsymbol{\sigma}}{\partial\Delta\boldsymbol{\varepsilon}} \tag{62}$$

needs to be established [16]. If the stress state is entirely elastic, this matrix is simply given as the elastic constitutive matrix, $\boldsymbol{D}$. In the cases of plastic straining in multisurface plasticity, only the active yield surfaces contribute to the consistent constitutive matrix and an expression can be found in Ottosen and Ristinmaa [11]. This expression can be written in a more general form that automatically omit the inactive yield surfaces by expanding it to

$$\boldsymbol{D}^{epc} = \boldsymbol{D}^c - \boldsymbol{D}^c \sum_{i=1}^{n}\sum_{k=1}^{n} \alpha_i\alpha_k (\boldsymbol{A}^{-1})_{ik} \frac{\partial\Delta\boldsymbol{\varepsilon}^p}{\partial\Delta\lambda_i} \left(\frac{\partial f_k}{\partial\boldsymbol{\sigma}}\right)^T \boldsymbol{D}^c \tag{63}$$

where $\boldsymbol{A}$ is the $n \times n$ matrix given by

$$A_{ik} = \alpha_i\alpha_k \left(\left(\frac{\partial f_i}{\partial\boldsymbol{\sigma}}\right)^T \boldsymbol{D}^c \frac{\partial\Delta\boldsymbol{\varepsilon}^p}{\partial\Delta\lambda_k} + \left(\frac{\partial f_i}{\partial\boldsymbol{K}}\right)^T \frac{\partial\boldsymbol{K}}{\partial\bar{\varepsilon}^p} \frac{\partial\bar{\varepsilon}^p}{\partial\Delta\lambda_k} \right) + (\alpha_i - 1)(\alpha_k - 1)\delta_{ik} \tag{64}$$

δ is the Kronecker delta, α_i is defined as

$$\alpha_i = \begin{cases} 1 & \text{if } f_i \text{ is active, i.e } \Delta\lambda_i > 0 \\ 0 & \text{if } f_i \text{ is inactive, i.e. } \Delta\lambda_i = 0 \end{cases} \tag{65}$$

n is the total number of yield surfaces and $\boldsymbol{D}^c$ is the modified elastic stiffness matrix given by

$$\boldsymbol{D}^c = \boldsymbol{T}\boldsymbol{D} \tag{66}$$

with $\boldsymbol{T}$ being the modification matrix given by

$$\boldsymbol{T} = \left(\boldsymbol{I} + \sum_{i=1}^{n} \Delta\lambda_i \frac{\partial\boldsymbol{b}_i}{\partial\boldsymbol{\sigma}} \right)^{-1} \tag{67}$$

Since the Hoek–Brown criterion is formulated in principal stress space, the consistent constitutive matrix is found relative to the rotated coordinate system of $\bar{\boldsymbol{\sigma}}^B$, which is denoted $\hat{\boldsymbol{D}}^{epc}$. Afterwards, $\hat{\boldsymbol{D}}^{epc}$ is then rotated back to the original coordinate system, giving $\boldsymbol{D}^{epc}$, just as $\bar{\boldsymbol{\sigma}}^C$ is rotated back to $\boldsymbol{\sigma}^C$. For further details see Clausen et al. [15], Clausen [13] and Ottosen and Ristinmaa [11].

9. Verification: tunnel excavation

The numerical implementation is tested on a simulation of a circular tunnel excavation in an infinite rock mass. The goal is to obtain the ground response curves for the tunnel, see e.g. [17]. The excavation is simulated by reducing the pressure, p, on the tunnel wall from the in situ pressure, p_∞, at time $T=0$, to 0 at time $T=1$, cf. Fig. 12.

The self-weight of the rock material is neglected, so the axisymmetric properties of the problem are utilized, and a 1 m section of the tunnel wall in the z-direction is modeled, cf. Fig. 12. The radius of the tunnel is r_T and the extend of the model is limited to a radius of r_{BC}. The domain is modeled by a simple mesh consisting of isoparametric quadrilateral 9-node elements with 2×2 Gauss points. In order to minimize problems of bifurcations and strain localization, only one element is used in the z-direction. Further, the element size varies linearly, so that the element farthest away is 4 times bigger than the one at the tunnel wall. Based on a convergence analysis of the following simulations, a total of 12 800 elements have been used.

In the following, the numerical implementation will be sought verified for three different post-peak behaviors, namely elastic–perfectly-plastic, softening and elastic-brittle, cf. Fig. 2.

9.1. Elastic–perfectly-plastic and elastic-brittle behavior

For the elastic–perfectly-plastic and elastic-brittle behavior, the implementation will be compared with the analytical solution of Sharan [14], which is able to handle both scenarios.

As basis for the comparison, the material parameters of examples A

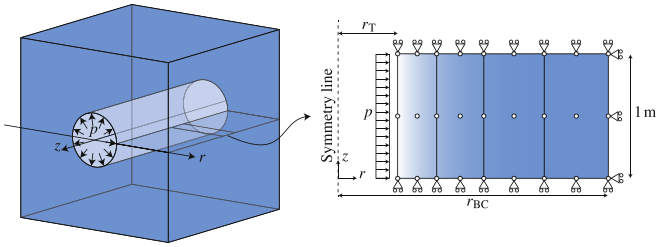

Fig. 12. Concept of the axisymmetric FE-model of the tunnel excavation.

Table 2
Hoek–Brown parameters of tunnel rock mass material. Examples from Sharan [14].

Example		σ_{ci} (MPa)	a (–)	m_b (–)	s (–)	σ_{cig} (MPa)	a_g (–)	m_{bg} (–)	s_g (–)	K_d (–)	E (GPa)	ν (–)
A	$\boldsymbol{K}_{peak}$	150	0.5	10.2	0.062	150	1	0.5	0.062	1.5	42	0.2
	$\boldsymbol{K}_{res}$	150	0.51	1.27	0.0002	150	1	0.5	0.062	1.5	42	0.2
B	$\boldsymbol{K}_{peak}$	80	0.51	2.01	0.0039	80	1	0.15	0.0039	1.15	9	0.25
	$\boldsymbol{K}_{res}$	80	0.53	0.34	0	80	1	0.15	0.0039	1.15	9	0.25

and B of Sharan [14] are utilized. The parameters consists of peak parameters and residual parameters, cf. Table 2. In the method of Sharan [14], the ratio between the plastic strains in the σ_1-direction and the σ_3-direction is governed by a constant dilation parameter, K_d. The same behavior can be obtained using the plastic potential of Eq. (25) by setting $a_g = 1$ and $m_{bg} = K_d - 1$ cf. Eq. (34). Since the exponent $(a_g - 1)$ becomes 0, the values of s_g and σ_{cig} are irrelevant in this case, and thus the peak values have been specified.

The numerical implementation is incapable of handling the drop in Young's modulus described in the method of Sharan [14]. Because of this, Young's modulus is maintained constant throughout the simulation using the peak value. Thus the results listed for examples A and B in Sharan [14] cannot be compared directly. Therefore the examples have been recalculated using the solution method in Sharan [14] without the drop in Young's modulus to get comparable results.

In example A, $K_d = 1.5$ and $p_\infty = 150$ MPa has been chosen and in example B, $K_d = 1.15$ and $p_\infty = 20$ MPa has been chosen. Both resulting in non-associated plasticity. The radius of the tunnel is $r_T = 10$ m and the modeled domain is bounded by $r_{BC} = 300$ m.

For both examples, three simulations have been carried out in total, namely two elastic–perfectly-plastic simulations using $\boldsymbol{K}_{peak}$ and $\boldsymbol{K}_{res}$ respectively, and one elastic-brittle simulation where the parameters drop instantaneous from $\boldsymbol{K}_{peak}$ to $\boldsymbol{K}_{res}$ once yielding occurs.

The set of user defined points, cf. (30), needed to achieve perfect plasticity is simply

$$\{(0, \boldsymbol{K}_{peak})\} \quad \text{or} \quad \{(0, \boldsymbol{K}_{res})\}$$

respectively, since perfect plasticity is assumed before and after the user defined points, cf. Fig. 8. To achieve the brittle behavior, two points are needed, namely

$$\{(0, \boldsymbol{K}_{peak}), (0, \boldsymbol{K}_{res})\}$$

which represents an instantaneous drop in the hardening parameters. The way in which $\bar{\varepsilon}^p$ is defined, is indifferent, when perfect plasticity or brittle behavior is needed. The implementation will thus make use of the second version of $\bar{\varepsilon}^p$ as shown in (29).

The ground response curves of the simulations can be seen in Fig. 13, together with the solutions obtained from Sharan [14].

A comparison of the final tunnel wall displacement and the radius of the plastic zone is listed in Table 3. As can be seen, the numerical implementation gives results close to the analytical solution.

9.2. Strain softening behavior

Several solution procedures have been developed for circular tunnel excavations in strain softening rock masses. See e.g. Alonso et al. [18], Lee and Pietruszczak [19] and Wang et al. [20]. The numerical implementation will be compared to one example from Alonso et al. [18] and four examples from Lee and Pietruszczak [19]. All five examples have been treated in Wang et al. [20]. The material parameters of the five examples can be seen in Table 4. In all the examples, the parameters evolve linearly from a set of peak parameters, $\boldsymbol{K}_{peak}$, at $\bar{\varepsilon}^p = 0$ to a set of residual parameters, $\boldsymbol{K}_{res}$, after some amount of plastic straining. Hereafter perfect plasticity sets in. The only difference between examples L1 through L4 is in the evolution of a. The dilation angle ψ relates to K_d through

$$K_d = \frac{1 + \sin(\psi)}{1 - \sin(\psi)} \tag{68}$$

and the parameters of the plastic potential are thus found in a similar manner as for the perfectly-plastic and brittle models shown above. Again, this results in non-associated plasticity.

In the mentioned papers, the state variable, $\bar{\varepsilon}^p$, controlling the softening behavior, is chosen to be the deviatoric plastic strain

$$\bar{\varepsilon}^p = \varepsilon_1^p - \varepsilon_3^p$$

which will also be used in these simulations. In all examples, the tunnel radius is $r_T = 3$ m and the domain is bound by $r_{BC} = 300$ m. In example A, $p_\infty = 3.31$ MPa, while in examples L1 through L4, $p_\infty = 15$ MPa.

The ground response curves of the simulations can be seen in Fig. 14, together with solutions obtained from the algorithm of Wang et al. [20]. The wall displacement has been scaled relative to the wall displacement at the onset of plastic straining given by $r_T(p_\infty - p_c)/(2G)$, where p_c is the wall pressure at the onset of plastic straining. For further details see e.g. Lee and Pietruszczak [19].

When the ground response curve of example A1 is compared to the one shown in Alonso et al. [18], it is observed that the found

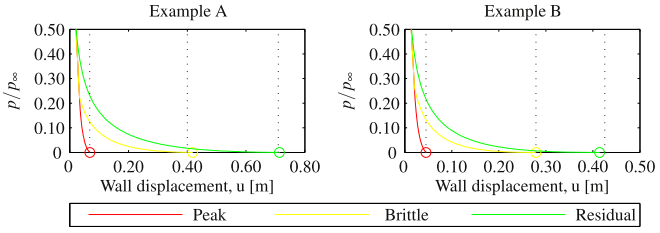

Fig. 13. Ground response curves for examples A and B. The dotted vertical lines represent the solution obtained by the procedure in Sharan [14].

Table 3
Comparison of results for elastic–perfectly-plastic and brittle material behavior.

Example		Wall displacement (m)			Plastic radius (m)		
		Sharan [14]	Present	Difference (%)	Sharan [14]	Present	Difference (%)
A	Peak	0.0683	0.0688	0.60	12.8918	12.8813	−0.08
	Brittle	0.4004	0.4179	4.36	23.4110	23.2750	−0.58
	Residual	0.7099	0.7133	0.49	38.6563	38.2756	−0.98
B	Peak	0.0453	0.0453	0.01	13.7586	13.7430	−0.11
	Brittle	0.2789	0.2789	−0.02	28.8523	28.5408	−1.08
	Residual	0.4254	0.4141	−2.66	46.3457	45.5650	−1.68

solution deviates significantly. However, this same deviation has also been found in Wang et al. [20], and when compared with the ground response curve presented there, it fits quite well. Hence the obtained results are believed to be correct. The ground response curves of L1 through L4 compares very well with the ones presented in Lee and Pietruszczak [19]. A comparable figure is not readily available in Wang et al. [20], but the described solution method has been implemented to get a more detailed comparison, as shown in Table 5, where the tunnel wall displacement and the plastic zone has been compared. As can be seen, this study results in slightly higher displacements than that of Wang et al. [20], while arriving at practically the same plastic zone. Based on this, the implementation is believed to be sound.

10. Conclusion

A non-associated strain hardening Hoek–Brown material model has been developed, which is capable of modeling an arbitrary user-defined hardening behavior. For jointed rock masses, this typically results in an elastic-brittle behavior, strain softening or perfect plasticity. A total of eight parameters are allowed to evolve based on the accumulated plastic strains. Through a transformation of the stress state to principal stress space, the model makes use of an implicit return mapping scheme. Since four possible locations of the updated stress state exist, four different return methods had to be developed. The correct algorithm is then guessed upon by the use of boundary planes. After successfully determining the updated stress state, the consistent constitutive matrix is found. Finally, the results are transformed back into the original coordinate system of the FE-model.

The model has been deployed on a FE-simulation of a tunnel excavation utilizing non-associated plasticity. Both elastic-brittle, strain softening and elastic–perfectly plastic post-failure behaviors were tried. The results obtained in the tunnel simulation are in good agreement with the analytical solutions.

Appendix A. Gradient of R

In order to find the solution to the equations used in the different return algorithms, the derivatives of $\boldsymbol{R}$ with respect to σ_1^C and $\Delta\lambda_i$ need to be established. The general formulation of the first entry in Eq. (40) reads

$$R_1 = \sigma_1^C - \sigma_1^B + \sum_{i=1}^{n} \Delta\lambda_i s_{i,1} \tag{A.1}$$

which when differentiated with respect to σ_1^C leads to

$$\frac{\partial R_1}{\partial \sigma_1^C} = 1 + \boldsymbol{D} \sum_{i=1}^{n} \Delta\lambda_i \frac{\partial \boldsymbol{b}_{i,1}}{\partial \sigma_1^C} \tag{A.2}$$

for $i=1$ one obtains

$$\frac{\partial \boldsymbol{b}_1}{\partial \sigma_1^C} = \begin{Bmatrix} \dfrac{\partial k_g}{\partial \sigma_1^C} \\ 0 \\ 0 \end{Bmatrix} \tag{A.3}$$

where

$$\frac{\partial k_g}{\partial \sigma_1^C} = (1 - a_g) \frac{a_g m_g^2}{\sigma_{cig}} \left(s_g - m_g \frac{\sigma_1^C}{\sigma_{cig}} \right)^{a_g - 2} \tag{A.4}$$

The derivative of the second entry of $\boldsymbol{R}$ with respect to σ_1 is very similar to the derivative of R_1 if it is a $\boldsymbol{l}_1$ step, since $\sigma_1 = \sigma_2$. On the other hand the derivative is very similar to the derivative of R_3 shown below, if it is $\boldsymbol{l}_6$ step, since $\sigma_2 = \sigma_3$.

The third entry of $\boldsymbol{R}$ in Eq. (40) has the general form of

$$R_3 = \sigma_3^C - \sigma_3^B + \sum_{i=1}^{n} \Delta\lambda_i s_{i,3} \tag{A.5}$$

The derivative of R_3 with respect to σ_1^C results in

Table 4
Hoek–Brown parameters of tunnel rock mass material exhibiting strain softening behavior. Example A1 is from Alonso et al. [18] while examples L1–L4 are from Lee and Pietruszczak [19].

Example		$\bar{\varepsilon}^p$ (−)	σ_{ci} (MPa)	a (−)	m_b (−)	s (−)	σ_{cig} (MPa)	a_g (−)	m_{bg} (−)	s_g (−)	ψ (deg)	E (GPa)	ν (−)
A1	$\boldsymbol{K}_{peak}$	0	27.6	0.50	0.50	0.001	27.6	1	0.698	0.001	15	1.38	0.25
	$\boldsymbol{K}_{res}$	0.0125	27.6	0.50	0.10	0.0005	27.6	1	0.191	0.0005	5	1.38	0.25
L1	$\boldsymbol{K}_{peak}$	0	30.0	0.50	2.00	0.004	25.0	1	0.698	0.004	15	5.70	0.25
	$\boldsymbol{K}_{res}$	0.01	25.0	0.50	0.60	0.002	25.0	1	0.191	0.002	5	5.70	0.25
L2	$\boldsymbol{K}_{peak}$	0	30.0	0.55	2.00	0.004	25.0	1	0.698	0.004	15	5.70	0.25
	$\boldsymbol{K}_{res}$	0.01	25.0	0.55	0.60	0.002	25.0	1	0.191	0.002	5	5.70	0.25
L3	$\boldsymbol{K}_{peak}$	0	30.0	0.60	2.00	0.004	25.0	1	0.698	0.004	15	5.70	0.25
	$\boldsymbol{K}_{res}$	0.01	25.0	0.60	0.60	0.002	25.0	1	0.191	0.002	5	5.70	0.25
L4	$\boldsymbol{K}_{peak}$	0	30.0	0.50	2.00	0.004	25.0	1	0.698	0.004	15	5.70	0.25
	$\boldsymbol{K}_{res}$	0.01	25.0	0.60	0.60	0.002	25.0	1	0.191	0.002	5	5.70	0.25

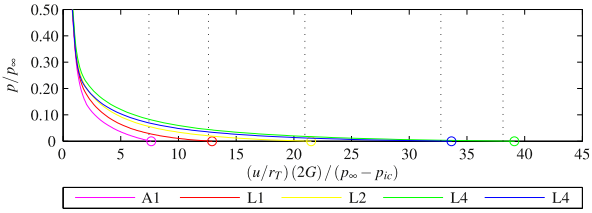

Fig. 14. Ground response curves for strain softening models. The dotted vertical lines represent the solution obtained by the procedure in Wang et al. [20].

Table 5
Comparison of results for strain softening material behavior.

Example	Wall displacement (m)			Plastic radius (m)		
	Wang et al. [20]	Present	Difference (%)	Wang et al. [20]	Present	Difference (%)
A1	0.0423	0.0435	2.69	6.30	6.31	0.12
L1	0.0771	0.0790	2.48	7.91	7.90	−0.06
L2	0.1249	0.1281	2.60	9.83	9.82	−0.12
L3	0.2218	0.2275	2.55	12.78	12.76	−0.17
L4	0.2003	0.2059	2.80	11.94	11.92	−0.14

$$\frac{\partial R_3}{\partial \sigma_1^C} = k + \boldsymbol{D}\sum_{i=1}^{n}\Delta\lambda_i\frac{\partial b_{i,3}}{\partial \sigma_1^C} \tag{A.6}$$

where

$$k = \frac{\partial \sigma_3^C}{\partial \sigma_1^C} = 1 + am_b\left(s - m_b\frac{\sigma_1^C}{\sigma_{ci}}\right)^{a-1} \tag{A.7}$$

The derivative of R_1 with respect to $\Delta\lambda_i$ is given by

$$\frac{\partial R_1}{\partial \Delta\lambda_i} = \boldsymbol{D}\left(b_{i,1} + \sum_{j=1}^{n}\Delta\lambda_j\frac{\partial b_{j,1}}{\partial \Delta\lambda_i}\right) \tag{A.8}$$

for $j=1$ one obtains

$$\frac{\partial \boldsymbol{b}_1}{\partial \Delta\lambda_i} = \begin{Bmatrix} \dfrac{\partial k_g}{\partial \Delta\lambda_i} \\ 0 \\ 0 \end{Bmatrix} \tag{A.9}$$

Since k_g is dependent on the hardening parameters, which in turn is dependent on $\bar{\varepsilon}^p$, this results in

$$\frac{\partial k_g}{\partial \Delta\lambda_i} = \frac{\partial k_g}{\partial \bar{\varepsilon}^p}\frac{\partial \bar{\varepsilon}^p}{\partial \Delta\lambda_i} \tag{A.10}$$

where

$$\begin{aligned}\frac{\partial k_g}{\partial \bar{\varepsilon}^p} &= \frac{\partial k_g}{\partial a_g}\frac{\partial a_g}{\partial \bar{\varepsilon}^p} + \frac{\partial k_g}{\partial m_{b_g}}\frac{\partial m_{b_g}}{\partial \bar{\varepsilon}^p} + \frac{\partial k_g}{\partial s_g}\frac{\partial s_g}{\partial \bar{\varepsilon}^p} + \frac{\partial k_g}{\partial \sigma_{ci_g}}\frac{\partial \sigma_{ci_g}}{\partial \bar{\varepsilon}^p} \\ &= \frac{\partial k_g}{\partial a_g}H_{a_g} + \frac{\partial k_g}{\partial m_{b_g}}H_{m_{b_g}} + \frac{\partial k_g}{\partial s_g}H_{s_g} + \frac{\partial k_g}{\partial \sigma_{ci_g}}H_{\sigma_{ci_g}}\end{aligned} \tag{A.11}$$

The different H-values are the relevant gradients of the user-defined points given in (30). The second derivative in (A.10) is dependent upon the choice of $\bar{\varepsilon}^p$. If the first version listed in (29) is used, then it can be found that

$$\frac{\partial \bar{\varepsilon}^p}{\partial \Delta\lambda_i} = \frac{\sqrt{\frac{2}{3}}\frac{1}{\|\Delta\boldsymbol{\varepsilon}^p\|}}{1 - \sqrt{\frac{2}{3}}\frac{1}{\|\Delta\boldsymbol{\varepsilon}^p\|}(\Delta\boldsymbol{\varepsilon}^p)^T\boldsymbol{c}}(\Delta\boldsymbol{\varepsilon}^p)^T\boldsymbol{b}_i \tag{A.12}$$

where

$$\boldsymbol{c} = \sum_{j=1}^{n}\Delta\lambda_j\frac{\partial \boldsymbol{b}_j}{\partial \bar{\varepsilon}^p} \tag{A.13}$$

has been introduced for readability. If the second version listed in (29) is used, then it can be found that

$$\frac{\partial \bar{\varepsilon}^p}{\partial \Delta\lambda_i} = \frac{b_{i,1} - b_{i,3}}{1 - (c_1 - c_3)} \tag{A.14}$$

where c_1 and c_3 are the first and the third component of $\boldsymbol{c}$.

The derivative of R_2 with respect to $\Delta\lambda i$ is either similar to the one for R_1 or the one below for R_3, depending on whether it is a $\boldsymbol{I}_1$ or $\boldsymbol{I}_6$ step.

The derivative of R_3 with respect to $\Delta\lambda_i$ is given by

$$\frac{\partial R_3}{\partial \Delta\lambda_i} = l + \boldsymbol{D}\left(b_{i,3} + \sum_{j=1}^{n}\Delta\lambda_j\frac{\partial b_{j,3}}{\partial \Delta\lambda_i}\right) \tag{A.15}$$

where

$$l = \frac{\partial \sigma_3^C}{\partial \Delta\lambda_i} = \frac{\partial \sigma_3^C}{\partial \bar{\varepsilon}^p}\frac{\partial \bar{\varepsilon}^p}{\partial \Delta\lambda_i} \tag{A.16}$$

and

$$\begin{aligned}\frac{\partial \sigma_3^C}{\partial \bar{\varepsilon}^p} &= \frac{\partial \sigma_3^C}{\partial a}\frac{\partial a}{\partial \bar{\varepsilon}^p} + \frac{\partial \sigma_3^C}{\partial m_b}\frac{\partial m_b}{\partial \bar{\varepsilon}^p} + \frac{\partial \sigma_3^C}{\partial s}\frac{\partial s}{\partial \bar{\varepsilon}^p} + \frac{\partial \sigma_3^C}{\partial \sigma_{ci}}\frac{\partial \sigma_{ci}}{\partial \bar{\varepsilon}^p} \\ &= \frac{\partial \sigma_3^C}{\partial a}H_a + \frac{\partial \sigma_3^C}{\partial m_b}H_{m_b} + \frac{\partial \sigma_3^C}{\partial s}H_s + \frac{\partial \sigma_3^C}{\partial \sigma_{ci}}H_{\sigma_{ci}}\end{aligned} \tag{A.17}$$

References

[1] Hoek E, Brown ET. Empirical strength criterion for rock masses. J Geotech Eng 1980;106:1013–35.
[2] Hoek E, Carranza-Torres C, Corkum B. Hoek–Brown failure criterion, 2002 ed. Proceedings of NARMS-TAC conference, Toronto, vol. 1, 2002. p. 267–73.
[3] Hoek E, Brown ET. Practical estimates of rock mass strength. Int J Rock Mech Min Sci 1997;34:1165–86.
[4] Sørensen ES, Clausen J, Damkilde L. Numerical implementation of the Hoek–Brown material model with strain hardening. In: Proceedings of the 5th international conference on structural engineering, mechanics and computation, Cape Town, South Africa, 2013. p. 375–80.
[5] Hoek E. Strength of jointed rock masses. Géotechnique 1983;23(3):187–223.
[6] Marinos P, Hoek E. GSI: a geologically friendly tool for rock mass strength estimation. In: Proceedings of the international conference on geotechnical and geological engineering, Melbourne, Australia, 2000. p. 1422–46.
[7] Hoek E. Practical rock engineering, 2007.
[8] Hoek E, Diederichs MS. Empirical estimation of rock mass modulus. Int J Rock Mech Min Sci 2006;43:203–15.
[9] Clausen J, Damkilde L. An exact implementation of the Hoek–Brown criterion for elasto-plastic finite element calculations. Int J Rock Mech Min Sci

2008;45:831–47.
[10] Koiter WT. Stress–strain relations, uniqueness and variational theorems for elasto-plastic materials with a singular yield surface. Q Appl Math 1953;11:350–4.
[11] Ottosen NS, Ristinmaa M. The mechanics of constitutive modeling. London: Elsevier; 2005.
[12] de Souza Neto EA, Perić D, Owen DRJ. Computational methods for plasticity. London: Wiley; 2008.
[13] Clausen J. Efficient non-linear finite element implementation of elasto-plasticity for geotechnical problems [Ph.D. thesis]. Computational Mechanics, Esbjerg Institute of Technology, Aalborg University Esbjerg ⟨http://vbn.aau.dk/files/14058639/JCthesis.pdf⟩, 2007.
[14] Sharan SK. Analytical solutions for stress and displacements around a circular opening in a generalized Hoek–Brown rock. Int J Rock Mech Min Sci 2008;45:78–85.
[15] Clausen J, Damkilde L, Andersen L. Efficient return algorithms for associated plasticity with multiple yield planes. Int J Numer Methods Eng 2006;66:1036–59.
[16] Simo JC, Taylor RL. Consistent tangent operators for rate-independent elasto-plasticity. Comput Methods Appl Mech Eng 1985;48:101–18.
[17] Brown ET, Bray JW, Ladanyi B, Hoek E. Ground response curves for rock tunnels. J Geotech Eng 1983;109:15–39.
[18] Alonso E, Alejano LR, Varas F, Fdez-Manín G, Carranza-Torres C. Ground response curves for rock masses exhibiting strain-softening behavior. Int J Numer Anal Methods Geomech 2003;27:1153–85.
[19] Lee Y-K, Pietruszczak S. A new numerical procedure for elasto-plastic analysis of a circular opening excavated in a strain-softening rock mass. Tunn Undergr Space Technol 2008;23:588–99.
[20] Wang S, Yin X, Tang H, Ge X. A new approach for analyzing circular tunnel in strain-softening rock masses. Int J Rock Mech Min Sci 2010;47:170–8.

Paper C

Implementation of the modified Hoek-Brown model into the finite element method

E. S. Sørensen, J. Clausen, R. S. Merifield & L. Damkilde

The paper has been published in
28th Nordic Seminar on Computational Mechanics 22-23 October Tallinn, 2015, Proceedings of the NSCM28 pp. 163–166, 2015.

28th Nordic Seminar on Computational Mechanics
NSCM-28
A. Berezovski, K.Tamm, T.Peets (Eds.)

IMPLEMENTATION OF THE MODIFIED HOEK-BROWN MODEL INTO THE FINITE ELEMENT METHOD

EMIL S. SØRENSEN*, JOHAN CLAUSEN*, RICHARD S. MERIFIELD† AND LARS DAMKILDE*

*Department of Civil Engineering, Aalborg University, 9000 Aalborg, Denmark,
e-mail: ess@civil.aau.dk – web page: www.civil.aau.dk

†GeoSolutions, SMEC, Newcastle, Australia, e-mail:
Richard.Merifield@smec.com – Web page: www.smec.com

Key words: Hoek-Brown, Tension cut-off, Elasto-plasticity, Implicit integration, Safety factor

Summary. The Hoek-Brown model for near-homogeneous rock masses will, in some cases, overpredict the tensile strength of the material. In some cases this can lead to unsafe design of structures. Therefore, a tension cut-off is introduced and the model is implemented into an elasto-plastic framework for use with the finite element method. The use of the model is illustrated with a computational example calculating the safety of mining tunnel roof.

1 Introduction

For near-homogeneous rock-masses the Hoek-Brown model[1,2], has become the standard when assessing the strength properties of related structures. Examples of such structures include footings resting on rock-masses and underground openings like tunnels and mine shafts. In some cases, though, the Hoek-Brown criterion may overestimate the tensile strength of the rock-mass[3], an aspect shared with the Mohr-Coulomb criterion[4]. In applications where the tensile strength has a significant influence on the overall safety of the structure, the level of safety will be over-estimated. This is relevant for configurations where parts of the domain will experience tensile stresses, as the rock masses surrounding underground openings. A simple method of mitigating this deficiency is to introduce a tension cut-off, also known as the Rankine criterion[4], into the Hoek-Brown yield criterion. The combination of these two models will be referred to as the Modified Hoek-Brown model. The model is implemented in to an elasto-plastic framework for use with the standard displacement finite element method. A fully implicit integration scheme is used for the stress update. A numerical example demonstrating the model is presented in Section 4.

2 The Modified Hoek-Brown model

The modern Hoek-Brown yield criterion is given as[2]

$$f(\boldsymbol{\sigma}) = \sigma_1 - \sigma_3 - \sigma_{ci}\left(s - m_b\frac{\sigma_1}{\sigma_{ci}}\right)^a = 0. \tag{1}$$

Here $\boldsymbol{\sigma}$ is the effective stress vector with tension taken as positive. The largest, i.e. most tensile, principal stress is denoted σ_1 and σ_3 is the smallest principal stress. The parameters of the criterion are the intact rock compressive strength σ_{ci} along with s, m_b and a. The three latter can be found on the basis of the GSI classification system[2].

The tension cut-off, i.e. Rankine, criterion can be expressed as

$$f_t(\boldsymbol{\sigma}) = \sigma_1 - \sigma_t = 0, \tag{2}$$

where σ_t is the maximum allowable tensile stress, which must obey $\sigma_t \leq \sigma_a = \sigma_{ci} s/m_b$, with σ_a being the apex stress in the Hoek-Brown criterion. An illustration of the Modified Hoek-Brown criterion can be seen in Figure 1.

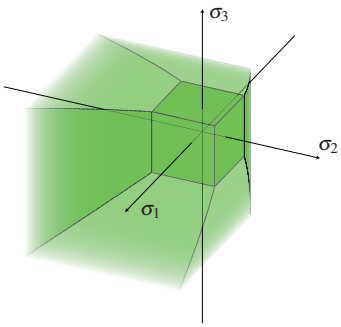

Figure 1: The Modified Hoek-Brown criterion in principal stress space.

As can be seen from the figure the criterion is a combination of surfaces that intersect in curves and points, which must be taken into account in the stress update procedure.

3 Stress update procedure

In each global equilibrium iteration in the elasto-plastic finite element procedure the stresses in each Gauss point need to be updated, see e.g. Neto et al.[5]. In this study the stress update is carried out using return mapping which is a fully implicit integration scheme.[5]. In the return mapping procedure an elastic predictor stress is calculated at each Gauss point, and the the stress state is "returned" to the yield face if it is located outside the elastic region defined by the yield surface. Within this scheme the methods presented in[6,7,8,9] are used here. The idea is to perform the calculations in principal stress space and then transform the updated stress and constitutive matrix back into the general stress space.

One of the main issues is to identify the type of stress return, i.e. to which surface, curve or point should the stress be returned. The yield criterion is divided into a number of updated stress point regions, see figure 2 a).

In this figure the regions S_{HB} and S_{TC} represent stress return to the Hoek-Brown and the Rankine yield surfaces, respectively, C_1, C_2, L_1 and L_2 represent curves arising at the intersection of two surfaces and P_1, P_2 and P_3 are stress points where two or more curves meet.

The way to determine to which region the predictor stress should be returned is by using the so-called boundary planes shown in Figure 2 b), which are defined on the basis of the geometry of the yield plane. Via the equations for these planes the correct return is determined.

4 Numerical example: Safety factor of an underground opening

In longwall mining rectangularly shaped cavities are formed in the rock mass, see e.g.[10]. In the design of these cavities the safety factor is assessed. The definition of the safety factor F is

$$F = \frac{\gamma_f}{\gamma}, \tag{3}$$

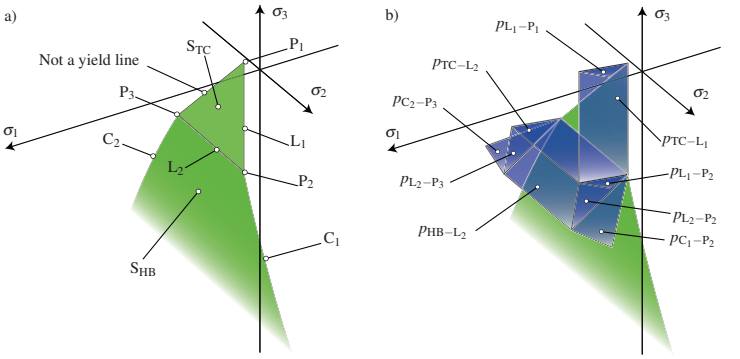

Figure 2: a) Designations of the different surfaces, curves and points of the model. b) Boundary planes. Only the part of the yield criteria corresponding to $\sigma_1 \geq \sigma_2 \geq \sigma_3$ is shown.

where γ_f is the rock mass weight that will cause failure, and γ is the actual weight. The following example serves as an illustration of the influence of the tension cut-off on the safety factor.

The example geometry and boundary conditions can be seen in Figure 3 a). The underground opening has dimensions 40 m $\times$ 3 m. Due to symmetry only half of the domain is modelled. The material parameters are $\sigma_c = 80$ MPa, $m_b = 3.354$, $s = 3.866 \cdot 10^{-3}$ and $a = 0.05057$. The actual weight of the rock mass is $\gamma = 20$ kN/m^3. Plane strain is assumed. The domain is meshed with elements with quadratic shape functions and full integrations using the finite element software Abaqus[11]. The material model is implemented as a user defined material (UMAT). The calculation steps are as follows

1. The initial stress state is established. The cavity is not yet established. This is simulated

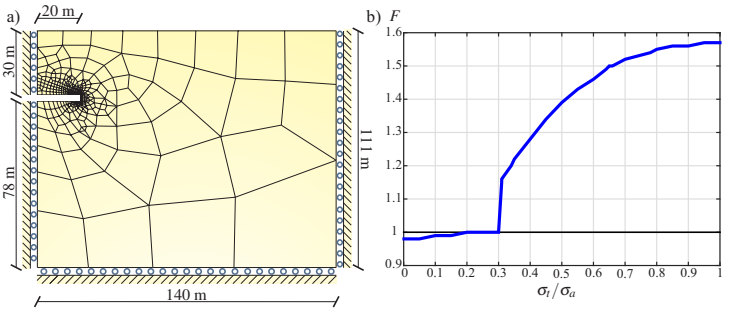

Figure 3: a) Domain size, boundary conditions and finite element mesh. b) Safety factor F depending on the tensile strength.

by loading the cavity edges with pressures equal to those of the in situ loads. An in situ vertical/horizontal pressure coefficient of $k_0 = 1$ is assumed.

2. The cavity is excavated. This is simulated by removing the loads at the cavity edges.

3. The selfweight of the soil is raised from the actual value γ. The value just before equilibrium can no longer be achieved is designated γ_f and the safety factor is then given by Equation 3.

For the original Hoek-Brown criterion a safety factor of $F = 1.57$ is found, which is in agreement with the results from[10]. Consecutive calculations with different values of the tensile cut-off values are carried out and the results are shown in Figure 3 b). It is seen that the safety factor drops sharply to a value below unity around $\sigma_t/\sigma_a = 0.3$.

5 Conclusions

The Modified Hoek-Brown model is implemented into the displacement finite element method using a fully implicit stress update scheme. A numerical example shows that the value of the tensile strength has a great influence of the safety factor of an underground opening.

REFERENCES

[1] Hoek, E. & Brown, E. T. Practical estimates of rock mass strength. *International Journal of Rock Mechanics and Mining Sciences* **34**, 1165–1186 (1997).

[2] Hoek, E., Carranza-Torres, C. & Corkum, B. Hoek-Brown failure criterion – 2002 edition. In *Proceedings of the North American Rock Mechanics Society Meeting in Toronto in July 2002* (2002).

[3] Iwanec, A. M. S. *The Geomechanics of Single-Seam and Multi-Seam Longwall Coal Mining*. Ph.D. thesis, The University of Newcastle, Australia (2014). Http://hdl.handle.net/1959.13/1045347.

[4] Ottosen, N. S. & Ristinmaa, M. *The Mechanics of Constitutive Modelling* (Elsevier, 2005).

[5] de Souza Neto, E. A., Perić, D. & Owen, D. J. R. *Computational Methods for Plasticity – Theory and Applications* (Wiley, 2008).

[6] Clausen, J., Damkilde, L. & Andersen, L. Efficient return algorithms for associated plasticity with multiple yield planes. *International Journal for Numerical Methods in Engineering* **66**, 1036–1059 (2006).

[7] Clausen, J. & Damkilde, L. A simple and efficient FEM-implementation of the Modified Mohr-Coulomb criterion. In Dahlblom, O. *et al.* (eds.) *Proceedings of the 19th Nordic Seminar on Computational Mechanics*, 214–219. Lund University (Lund University, 2006).

[8] Clausen, J. & Damkilde, L. An exact implementation of the Hoek-Brown criterion for elasto-plastic finite element calculations. *International Journal of Rock Mechanics and Mining Sciences* **45**, 831–847 (2008).

[9] Clausen, J. Robust and efficient handling of yield surface discontinuities in elasto-plastic finite element calculations. *Engineering Computations* **32**, 1722–1752 (2015).

[10] Suchowerska, A., Merifield, R., Carter, J. & Clausen, J. Predition of underground cavity roof collapse using the Hoek-Brown failure criterion. *Computers and Geotechnics* **44**, 93–103 (2012).

[11] Dassault Systèmes Simulia Corp. *Abaqus 6.14* (2014).

Paper D

Comparison of numerical formulations for the modeling of the dynamic tensile resistance of suction buckets

E. S. Sørensen, J. Clausen & L. Damkilde

The paper has been submitted to
Computers and Geotechnics

Comparison of numerical formulations for the modeling of the dynamic tensile resistance of suction buckets

E. S. Sørensen[a,*], J. Clausen[a], L. Damkilde[a]

[a]*Department of Civil Engineering, Aalborg University, Sofiendalsvej 11, 9000 Aalborg, Denmark*

Abstract

The dynamic tensile resistance of a suction bucket is investigated using three different numerical formulations. The first formulation utilizes the three-field *u-p-U* formulation accounting for solid and fluid displacements, u and U, as well as the pore-fluid pressure, p. The two other formulations comprise the simpler *u-p* formulation in its dynamic and quasi-static form, accounting only for solid displacement and pore-fluid pressure. As basis for comparison, the tensile resistance of a single suction bucket is investigated using a velocity-driven model for a wide range of velocities. It is found, that the quasi-static *u-p* formulation is sufficient for most relevant velocities.

Keywords: *u-p-U* formulation, *u-p* formulation, dynamic, quasi-static, suction bucket, tensile resistance

1. Introduction

Offshore jacket structures are exposed to overturning moments due to loads of dynamic nature stemming from e.g. wind, waves and currents as well as ice or ship impacts. For relatively light structures, such as wind turbines, the overturning moment can lead to tensile loading of the individual foundations of the structure, and thus the tensile resistance of the foundations has to be accounted for.

*Corresponding author
Email addresses: ess@civil.aau.dk (E. S. Sørensen), jc@civil.aau.dk (J. Clausen), lda@civil.aau.dk (L. Damkilde)

In this regard, a great amount of effort has gone into the determination of the dynamic tensile resistance of the suction bucket foundation concept shown in Figure 1, see e.g. [1, 2, 3, 4, 5, 6]. For a very slow loading rate, the behavior is drained, and the resistance is simply governed by friction along the inside and outside bucket skirt as shown in Figure 2a. During such drained failure, a gap develops between the soil and the bucket lid in accordance with the bucket heave. This gap is filled with water flowing in from the bottom of the bucket.

Under faster tensile loading, a faster fluid flow into the bucket is needed in order to keep up with the gap development. However, the fluid flow is impeded by the water's inability to flow freely through the soil skeleton. Consequently, the gap is to a greater or lesser extent prevented from expanding and a pressure difference develops between the inside and outside of the bucket as shown in Figure 2b. For a high load rate, an undrained behavior is obtained, where the gap is completely closed as shown on Figure 2c. The developed pressure difference can significantly increase the tensile resistance of the suction bucket, however as described, it is highly rate dependent and linked to the strength and deformation characteristics of the soil and its hydraulic properties as well as the properties of the fluid.

Geotechnical problems of such dynamic nature, which are influenced by coupled soil-fluid interaction can be treated using poroelasticity as developed by Biot [7, 8, 9] in combination with elasto-plasticity [10, 11] or equivalent constitutive frameworks accounting for the non-linear behavior of the soil skeleton.

For saturated soils, a variety of numerical formulations for implementation into the finite element method have been presented in [12]. The most general of these formulations is the rather complex u-p-U formulation, which is a three-field formulation accounting for the displacement of the soil skeleton, u, the pore fluid pressure, p, and the pore-fluid displacement, U, as well as all relevant first and second order time derivatives.

By neglecting the relative acceleration of the fluid phase, the governing equations can be cast in a significantly simpler two-field u-p formulation, which only tracks the soil skeleton movement and pore fluid pressure. An in-depth exposi-

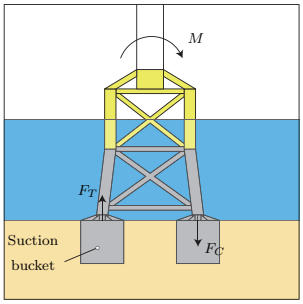

Figure 1: Offshore jacket structure utilizing suction buckets. When the structure is exposed to an overturning moment, M, tensile, F_t, and compressive, F_c, loads develop in the individual foundations.

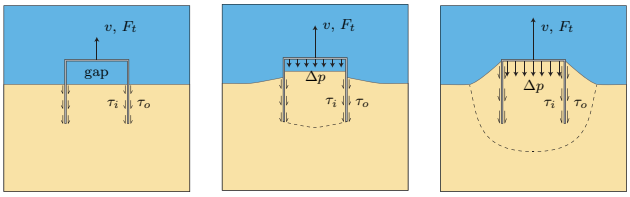

(a) (b) (c)

Figure 2: Different failure mechanisms of bucket foundation under tensile loading, F_t depending on pullout velocity v. (a) Drained behavior governed by friction along inside and outside skirt, τ_i and τ_o respectively. Development of gap between soil and bucket lid. (b) Partially drained behavior with friction along skirt and suction, Δp, beneath bucket lid. Reduced gap development. (c) Undrained behavior with friction along skirt and suction beneath bucket lid. No gap development.

tion of this formulation is given in e.g. [13].

Owing to its simplicity, the *u-p* formulation has been adopted in numerous commercial finite element codes such as e.g. Abaqus [14] and Plaxis [15] in various forms. However, the more elaborate three-field *u-p-U* formulation is starting to gain traction, see e.g. [16, 17]. One reason is that the inertia associated with the fluid acceleration is insignificant for slow phenomena, but might play a role in problems of more rapid nature. In addition to proper incorporation of fluid inertia, the three-field formulation also allows for more detailed modeling of boundary conditions since the displacement of both skeleton and water can be described independent of each other. Further, the formulation incorporates the viscous damping associated with the seepage forces of the fluid. Lastly, the *u-p* formulation restricts the choice of interpolation functions that can be used in order to fulfill the Ladyženskaja-Babuška-Brezzi conditions concerning well-posedness of the discretization, which is not the case for the *u-p-U* formulation [13]. On the downside, the *u-p-U* formulation is still not widely available yet and is computational more expensive due to the additional unknowns of the fluid displacement field.

The tensile resistance of suction bucket foundations has previously been treated numerically, see e.g. [18, 19, 20]. However, common for these models is that they utilize Abaqus, which only incorporates a quasi-static formulation of the *u-p* formulation, thus neglecting all inertial terms.

In this study the dynamic tensile resistance of a suction bucket foundation is investigated using both the *u-p-U* formulation as well as the *u-p* formulation in its dynamic form and under quasi-static conditions in order to investigate the effects of inertia.

2. The *u-p-U* formulation

The governing equations behind the *u-p-U* formulation originate from the equilibrium conditions for each phase of the material, the mass balance of the fluid flow and an appropriate constitutive relationship.

Using index notation, the equilibrium condition for the skeleton is given by

$$\sigma''_{ij,j} - (\alpha - n)\, p_{,i} + (1 - n)\, \rho_s b_i - (1 - n)\, \rho_s \ddot{u}_i + nR_i = 0 \tag{1}$$

where n is the porosity, p is the pore pressure (compression positive), ρ_s is the average density of the solid phase, b_i is the body force, $\ddot{u}_i$ is the solid phase acceleration, R_i is the viscous drag force originating from fluid movement through the skeleton, σ''_{ij} is the effective Biot stress tensor (tension positive) given by

$$\sigma''_{ij} = \sigma_{ij} + \alpha p \tag{2}$$

σ_{ij} is the total stress tensor and α is the Biot coefficient defined by

$$\alpha = 1 - \frac{K}{K_s} \tag{3}$$

where K is the bulk modulus of the soil skeleton and K_s is the average bulk modulus of the constituents of the soil skeleton. Using the Darcy flow law, the viscous drag force, R_i, is given by

$$R_i = k_{ij}^{-1} \dot{w}_j = k_{ij}^{-1} \left(\dot{U}_i - \dot{u}_i \right) n \tag{4}$$

where $\dot{w}$ is the seepage velocity, $\dot{U}$ is the fluid velocity and k_{ij} is the permeability of the soil skeleton related to the hydraulic conductivity $k_{D\,ij}$ through

$$k_{ij} = \frac{k_{D\,ij}}{\rho_f g} \tag{5}$$

where g is the gravitational acceleration.

The equilibrium condition for the fluid is given by

$$-np_{,i} + n\rho_f b_i - n\rho_f \ddot{U}_i - nR_i = 0 \tag{6}$$

where $\ddot{U}$ is the fluid acceleration.

The mass balance of the fluid flow is given by

$$-n\dot{U}_{i,i} - (a - n)\, \dot{\varepsilon}_{ii} - \frac{1}{Q}\dot{p} = 0 \tag{7}$$

where ε is the strain tensor and $1/Q$ is the combined storage capacity of the solid and fluid due to a change in pressure given by

$$\frac{1}{Q} = \frac{n}{K_f} + \frac{\alpha - n}{K_s} \tag{8}$$

where K_f is the bulk modulus of the fluid. Integration of (7) with respect to time yields

$$-nU_{i,i} - (\alpha - n)\,\varepsilon_{ii} - \frac{1}{Q}p - f_{p0} = 0 \tag{9}$$

where f_{p0} is an integration constant.

Finally, the constitutive relationship is stated as

$$\dot{\sigma}''_{ij} = D_{ijkl}\dot{\varepsilon}_{kl} \tag{10}$$

and governed by a suitable material model such as e.g. the Mohr-Coulomb material model.

In the finite element implementation, the u, p and U fields are approximated with

$$\boldsymbol{u} \approx \boldsymbol{N}^u\bar{\boldsymbol{u}} \qquad \boldsymbol{p} \approx \boldsymbol{N}^p\bar{\boldsymbol{p}} \qquad \boldsymbol{U} \approx \boldsymbol{N}^U\bar{\boldsymbol{U}} \tag{11}$$

where $\boldsymbol{N}^u$, $\boldsymbol{N}^p$ and $\boldsymbol{N}^U$ are interpolation functions and $\bar{\boldsymbol{u}}$, $\bar{\boldsymbol{p}}$ and $\bar{\boldsymbol{U}}$ designate the degrees of freedom at each node. Using the weighted residual Galerkin approach, the governing equations can be cast as

$$\boldsymbol{M}\ddot{\bar{\Phi}} + \boldsymbol{C}\dot{\bar{\Phi}} + \boldsymbol{K}\bar{\Phi} + \boldsymbol{L}\left(\bar{\Phi}\right) = \boldsymbol{F} \tag{12}$$

where

$$\boldsymbol{M} = \begin{bmatrix} \boldsymbol{M}_s & \boldsymbol{0} & \boldsymbol{0} \\ \boldsymbol{0} & \boldsymbol{0} & \boldsymbol{0} \\ \boldsymbol{0} & \boldsymbol{0} & \boldsymbol{M}_f \end{bmatrix}, \quad \boldsymbol{C} = \begin{bmatrix} \boldsymbol{C}_1 & \boldsymbol{0} & -\boldsymbol{C}_2 \\ \boldsymbol{0} & \boldsymbol{0} & \boldsymbol{0} \\ -\boldsymbol{C}_2^T & \boldsymbol{0} & \boldsymbol{C}_3 \end{bmatrix}, \quad \boldsymbol{K} = \begin{bmatrix} \boldsymbol{0} & -\boldsymbol{G}_1 & \boldsymbol{0} \\ -\boldsymbol{G}_1^T & -\boldsymbol{P} & -\boldsymbol{G}_2^T \\ \boldsymbol{0} & -\boldsymbol{G}_2 & \boldsymbol{0} \end{bmatrix} \tag{13}$$

and

$$\bar{\boldsymbol{\Phi}} = \begin{bmatrix} \bar{\boldsymbol{u}} \\ \bar{\boldsymbol{p}} \\ \bar{\boldsymbol{U}} \end{bmatrix}, \qquad \boldsymbol{L}\left(\bar{\boldsymbol{\Phi}}\right) = \begin{bmatrix} \int_\Omega \boldsymbol{B}\boldsymbol{\sigma}''\,d\Omega \\ \boldsymbol{0} \\ \boldsymbol{0} \end{bmatrix}, \qquad \boldsymbol{F} = \begin{bmatrix} \bar{\boldsymbol{F}}_s \\ \bar{\boldsymbol{F}}_{p0} \\ \bar{\boldsymbol{F}}_f \end{bmatrix} \tag{14}$$

where the definition of each component is listed in Appendix A.

As can be seen, the formulation incorporates inertia of both solid and fluid phases along with damping of the system associated with fluid flow as given by Darcy's flow law.

3. The *u-p* formulation

Substitution of

$$\ddot{U}_i = \frac{\ddot{w}_i}{n} + \ddot{u}_i \tag{15}$$

c.f. (4), into the fluid equilibrium equation (6), it reduces to

$$-np_{,i} + n\rho_f b_i - n\rho_f \ddot{u}_i - nR_i = 0 \tag{16}$$

when neglecting the fluid acceleration relative to the skeleton, $\ddot{w}$. Adding this equation to (1), the two equilibrium equations can be reduced to a single equilibrium equation for the entire mixture given by

$$\sigma''_{ij,j} - \alpha p_{,i} + \rho b_i - \rho \ddot{u}_i = 0 \tag{17}$$

where

$$\rho = (1-n)\,\rho_s + n\rho_f \tag{18}$$

Further, combining (16) and (4), an expression for $\dot{U}$ can be found and inserted into the continuity equation which can be cast as

$$\left(k\left(-p_{,i} - \rho_f \ddot{u} + \ \rho_f b_i\right)\right)_{,i} + \alpha\dot{\varepsilon}_{ii} + \frac{1}{Q}\dot{p} = 0 \tag{19}$$

However, the term concerning the solid acceleration results in a non-symmetric equation system and is further ignored [13]. Using similar approximation for u and p as stated in (11), the weighted residual Galerkin approach results in a similar equation as (12), where

$$\boldsymbol{M} = \begin{bmatrix} \boldsymbol{M}_m & \boldsymbol{0} \\ \boldsymbol{0} & \boldsymbol{0} \end{bmatrix}, \qquad \boldsymbol{C} = \begin{bmatrix} \boldsymbol{0} & \boldsymbol{0} \\ \boldsymbol{Q} & \boldsymbol{S} \end{bmatrix}, \qquad \boldsymbol{K} = \begin{bmatrix} \boldsymbol{0} & -\boldsymbol{Q}^T \\ \boldsymbol{0} & \boldsymbol{H} \end{bmatrix} \tag{20}$$

and

$$\bar{\boldsymbol{\Phi}} = \begin{bmatrix} \bar{\boldsymbol{u}} \\ \bar{\boldsymbol{p}} \end{bmatrix}, \qquad \boldsymbol{L}\left(\bar{\boldsymbol{\Phi}}\right) = \begin{bmatrix} \int_\Omega \boldsymbol{B}\boldsymbol{\sigma}'' d\Omega \\ \boldsymbol{0} \end{bmatrix}, \qquad \boldsymbol{F} = \begin{bmatrix} \bar{\boldsymbol{F}}_m \\ \bar{\boldsymbol{F}}_p \end{bmatrix} \tag{21}$$

where the definition of each component is listed in Appendix B. In the quasi-static case, the mass matrix of the mixture, $\boldsymbol{M}_m$, is further neglected, and thus no inertia is included.

4. Numerical implementation

Owing to the scarce availability of the *u-p-U* formulation in common finite element codes, a custom code has been developed and applied in the simulations of this study. The code has been verified for a variety of examples given in [16, 17, 21], covering both quasi-static and elasto-dynamic problems. Further, since Abaqus is only capable of treating the quasi-static case, a custom *u-p* implementation has also been developed and employed in the simulations. As a further check of the implementations, the quasi-static case is handled using Abaqus. For simulations in the drained range, all three formulations should produce similar results

5. Basis of comparison

Owing to the complexity of the simulations, the comparison is based on the simulation of a single suction bucket foundation made of steel with a bucket diameter, D, of 10 m, a skirt length, L, of 10 m and a skirt thickness, t, of 30 mm, as summarized in Table 1. A sketch of the model is shown in Figure 3. The seabed is taken as Baskarp sand no. 15. The dynamic tensile resistance is investigated for different pullout velocities, v, in the range from what is believed to be a drained behavior at $1 \cdot 10^{-6}$ $^{\mathrm{m}}/_{\mathrm{s}}$, to a very extreme response of 1 $^{\mathrm{m}}/_{\mathrm{s}}$, in steps of one order of magnitude.

6. Model composition

This section describes the specifics of the numerical simulation of the bucket foundation, which follows the method used in [18, 19]. A summary of all relevant parameters is listed in Table 2 at the end of this section.

6.1. Discretization

The axisymmetric properties of the problem is exploited so that the domain is modeled using 10443 2D axisymmetric 4-node quadrilateral continuum elements with bi-linear interpolation for all fields and for all formulations. Further,

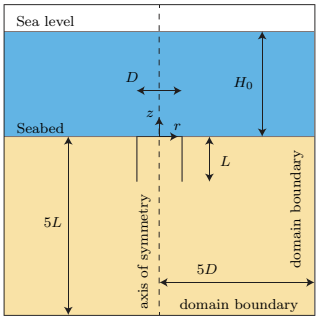

Figure 3: General model parameters and domain extent.

Bucket properties		
Bucket diameter	D	10 m
Skirt length	L	10 m
Skirt thickness	t	30 mm

Table 1: Bucket dimensions used in simulation.

small displacements is assumed. The model domain extends out to $5D$ in the radial direction and covers a depth of $5L$. The mesh can be seen on Figure 4.

The soil domain is modeled as a porous material using the u-p-U and u-p formulation respectively, whereas the bucket domain is modeled as an ordinary continuum material using the standard finite element formulation that accounts only for the displacement u.

Integration is carried out using Gauss quadrature with 3×3 integration points per element. The soil and bucket domain is discretized individually, but nodes along the common boundary are identically placed, so that contact constraints across the boundary can be applied using simple node-to-node contact elements implemented using the Lagrangian multiplier method [22].

In order to model the possible formation of the water-filled gap underneath

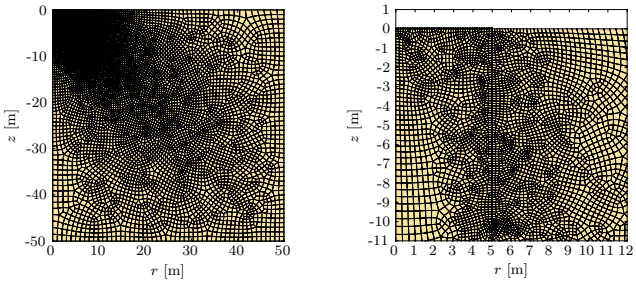

Figure 4: The domain extends out to $r = 50$ m and $z = -50$ m and is meshed using 10443 2D axisymmetric 4-node quadrilaterals. See also Figure 5. (a) Entire domain. (b) Close-up around bucket.

the bucket lid and skirt, c.f. Figure 2, a 10 mm thick layer of elements with special material properties is incorporated between the two domains as shown on Figure 5. This approach is also used for the models in [20, 18, 19]. These elements ensure, that the continuity equation is fulfilled in the gap. In order to mimic water, they are modeled with insignificant Young's modulus and a Poisson's ratio of 0.499. In the Abaqus model, the hybrid element formulation is utilized.

The use of such water elements is necessary even for the *u-p-U* formulation, despite its ability to model the solid and fluid phases separately. This is due to the fact, that the fluid displacement, U, is defined as taking place in the pores of the porous medium. However, once the fluid flows across the seabed and out of the porous medium, there is a drop in velocity corresponding to the porosity as shown on Figure 6. Hence, if the seabed has a porosity of 0.5 and remains stationary while the bucket is lifted, c.f. Figure 2a, the vertical fluid displacement and velocity within the soil, $\dot{U}_z$, would be twice that of the bucket in order to fill the developing gap. If on the other hand, the seabed moves up simultaneously with the bucket, c.f. Figure 2c, the vertical fluid velocity and

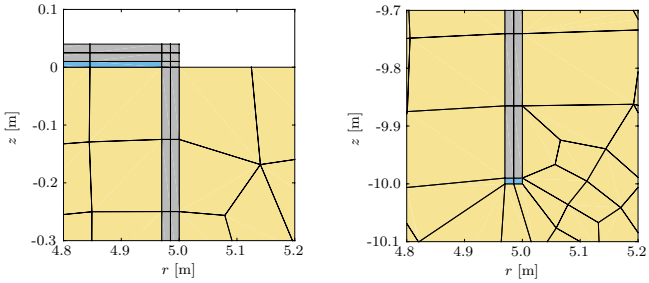

Figure 5: The model utilizes a layer of elements underneath the bucket lid and skirt, which have special material parameters in order to allow for the possible development of water filled gaps. These special elements are shown in blue, while elements belonging to the soil domain are shown in yellow and elements belonging to the bucket are shown in gray. (a) Excerpt of water elements under lid. (b) Water elements under skirt.

displacement in the soil would match that of the bucket. Since the movement of the seabed is unknown, the fluid movement is thus also unknown.

6.2. Material model and parameters

The bucket domain is modeled using a simple linear elastic material model and is assumed to have a unit weight of 7500 $^{\mathrm{kg}}/_{\mathrm{m}^3}$, a Young's modulus of 210 GPa and a Poisson's ratio of 0.25.

As stated, the seabed is taken as Baskarp sand no. 15. The failure and

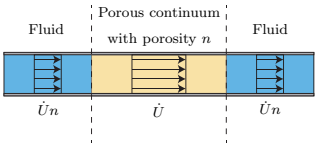

Figure 6: One-dimensional steady-state flow through a porous continuum, showing the drop in fluid velocity when the fluid flows out of the continuum at the right.

deformation of the soil skeleton is modeled using the classical isotropic pressure-dependent Mohr-Coulomb model following the non-associated elastic-perfectly-plastic implementation given in [23, 24], which employ implicit return mapping in principal stress space. Based on the density index, I_D, and confining pressure, the strength and deformation characteristics can be assessed through [25]. In this regard, it is assumed that the sand is relatively dense, such that $I_D = 85\%$ and the confining pressure is estimated at $\sigma_3' = 100$ kPa, resulting in non-associated plasticity c.f. Table 2. Since Baskarp sand no. 15 consists mainly of quartz, the bulk modulus of 36.4 GPa stated in [26] is used as bulk modulus of the solid constituent, K_s. In addition to this, the permeability can be assessed through [27], which shows a dependency on the void ratio. However, this dependency is not incorporated in the implementation, and the initial permeability is used throughout the entire simulation. Further, the earth pressure coefficient at rest, K_0, is assumed to be 0.33. The soil is assumed to be completely saturated with water with a density of 1000 $^{\mathrm{kg}}/_{\mathrm{m}^3}$ and a bulk modulus of 2.05 GPa.

6.3. Solid phase boundary conditions

The radial displacement of the solid skeleton, u_r, is restricted along the axis of symmetry at $r = 0$, and at the outer radial perimeter of the domain at $r = 5D$, as shown on Figure 7. Further, the vertical displacement of the solid skeleton, u_z, is restricted at the bottom of the domain at $z = -5L$. These conditions hold true for both the *u-p* and *u-p-U* models.

6.4. Pore pressure boundary conditions

The implementations do not account for cavitation, where the fluid shifts to a gas phase. This shift occurs when the pore pressure goes below the cavitation pressure, p_c, and highly affects the fluid properties and its ability to flow through the soil. Consequently, the tensile resistance of the bucket is also affected. Owing to this, the models are only valid for pore pressures above the cavitation

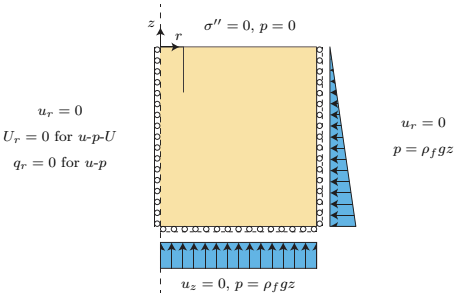

Figure 7: Schematic of model boundary conditions. Boundary conditions listed at the seabed only apply to the boundary outside the bucket.

pressure p_c. For water, the phase shift occurs at a pressure of $p_c \approx -100$ kPa relative to atmospheric pressure.

However, in the absence of cavitation, the effects of pore pressure on the resistance are only related to the pore pressure gradients and the relative pressure difference between the inside and outside of the bucket. Owing to this, the calculated pore pressure is measured relative to the hydrostatic pressure at the seabed, $p_0 = \rho_f g H_0$, where H_0 is the water depth, c.f. Figure 3. Using this approach, the model is representative for any water depth, as long as the calculated pressure, p, satisfies

$$p + p_0 > p_c \tag{22}$$

after which cavitation sets in.

Based on this, the pore pressure at the seabed outside the bucket is prescribed a fixed pore pressure of $p = 0$ kPa. Further, in order to allow water to flow freely into the domain, the pore pressure along the outer radial boundary and at the bottom is prescribed a hydrostatic pore pressure of $p = \rho_f g z$ as shown on Figure 7. These pore pressure boundary conditions hold true for both the u-p and u-p-U models. Further, it should be emphasized, that in the u-p-U formulation, these conditions require the addition of an external load on both

the solid and fluid phase c.f. (A.10) and (A.12).

6.5. Fluid phase boundary conditions

For the *u-p-U* model, an additional boundary condition of $U_r = 0$ on the axis of symmetry is required, while the fluid displacements at the other domain boundaries are left free, in order to allow water to flow into the domain.

6.6. Contact constraints

Along the entire boundary between the soil domain and the bucket domain, including the water elements, contact constraints are applied for the solid phase. As mentioned previously, the contact constraints are enforced by small strain node-to-node contact. The interface comprises a non-associated frictional stick-slip formulation incorporating a Mohr-Coulomb type friction law with the friction coefficient $\tan(\delta)$, $\delta = 26°$, and the adhesion $a = 0$ kPa, except around the water elements, which are modeled frictionless. Slip is assumed to occur without dilation.

For the *u-p* formulation, where only the solid displacements are solved for, separation of the boundaries is prevented in order not to generate any undefined voids between the soil and bucket boundary and to expand the water elements appropriately.

Contrary, for the *u-p-U* formulation, the solid phase of the soil domain is allowed to separate from the bucket. Further, an additional contact constraint is employed for the fluid phase along the entire boundary, which is modeled as frictionless. The fluid contact is not allowed to separate in order to ensure, that the water remains in contact with the bucket.

6.7. Initial conditions

The initial conditions of the model, at time $t = t_0$, are calculated based on hydrostatic conditions in the soil. Thus the initial pore pressure variation, $p(t_0)$, is given by

$$p(t_0) = \rho_f g z \tag{23}$$

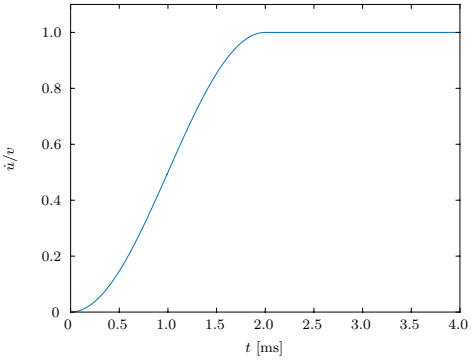

Figure 8: The velocity of the top of the bucket lid is phased in over a time period of 2 ms.

and the initial effective stresses, $\sigma''_{ij}(t_0)$, are given by

$$\sigma''_z(t_0) = -\left((1-n)\,\rho_s + (n-\alpha)\rho_f\right) gz \tag{24}$$

$$\sigma''_r(t_0) = \sigma''_\theta(t_0) = K_0\sigma''_z(t_0) \tag{25}$$

$$\sigma''_{rz}(t_0) = \sigma''_{r\theta}(t_0) = \sigma''_{z\theta}(t_0) = 0 \tag{26}$$

according to (2). Using these initial conditions, the intricate deformations in the soil due to installation of the bucket and appertaining selfweight of the structure is neglected, and the simulations thus start from a state where the resistance equilibrates the bucket weight. However, it is deemed to have little impact on the solution. Based on this stress state, the contact stresses on the interface elements are calculated.

6.8. Loading conditions

The tensile resistance of the bucket is simulated by applying a vertical velocity, v, to all nodes situated at the top of the bucket lid. The nodal velocity

$\dot{u}_z$ is phased in over a time period of 2 ms according to

$$\dot{u}_z(t) = \begin{cases} \left(0.5 - 0.5\cos\left(\frac{\pi t}{2\text{ ms}}\right)\right) v & \text{for } t < 2 \text{ ms} \\ v & \text{for } t \geq 2 \text{ ms} \end{cases} \tag{27}$$

and kept constant until the bucket has been raised 200 mm. The evolution is shown in Figure 8.

6.9. Time integration

For the dynamic models, the time integration is carried out using an ordinary Newmark integration scheme with $\gamma = 0.6$ and $\beta = 0.3025$, which is numerically stable and introduce slight numerical damping. For all pullout velocities, the first 10 ms are integrated using a timestep, Δt, of 0.2 ms after which the timestep is automatically controlled, aiming at approximately 1000 time steps to reach a vertical displacement of 200 mm.

7. Results

In this section, the obtained responses are analyzed and compared.

Initially, the results of the three different formulations is compared for the slowest pull-out velocity of $1 \cdot 10^{-6}$ m/s, which is expected to be fully drained, and should thus yield similar results. As can be seen on Figure 9, this generally seems satisfied, since all models predict a drained pull out capacity in the vicinity of 5 MN, though small differences are apparent. Both the *u-p-U* and the dynamic *u-p* formulation show perfectly plastic behavior, with the *u-p-U* model predicting a slightly lower capacity than the dynamic *u-p* formulation. However for the quasi-static *u-p* formulation, a slight increase in resistance is noticed which can not readily be explained.

A close-up of the initial development of the resistance and its composition is shown in Figure 10, which reveals, that the load displacement curve exhibits two distinct bends, dividing the curve into three almost linear parts. It can be seen, that all formulations predict a faster development of friction along

General parameters		
Gravity	g	$-9.82\ {}^{\mathrm{m}}/_{\mathrm{s}^2}$
Steel parameters		
Steel density	ρ	$7.5 \cdot 10^3\ {}^{\mathrm{kg}}/_{\mathrm{m}^3}$
Young's modulus	E	$210 \cdot 10^9$ Pa
Poisson's ratio	ν	0.25
Soil parameters		
Solid phase density	ρ_s	$2644\ {}^{\mathrm{kg}}/_{\mathrm{m}^3}$
Solid phase bulk modulus	K_s	$3.64 \cdot 10^{10}$ Pa
Fluid phase density	ρ_f	$1000\ {}^{\mathrm{kg}}/_{\mathrm{m}^3}$
Fluid phase bulk modulus	K_f	$2.05 \cdot 10^9$ Pa
Porosity	n	0.373
Permeability	k	$6.77 \cdot 10^{-9}\ {}^{\mathrm{m}^3\mathrm{s}}/_{\mathrm{kg}}$
Young's modulus	E	$5.44 \cdot 10^7$ Pa
Poisson's ratio	ν	0.25
Friction angle	φ	41.65°
Cohesion	c	$6.24 \cdot 10^3$ Pa
Dilation angle	ψ	16.14°
Earth pressure coefficient at rest	K_0	0.33
Interface parameters		
Adhesion	a	0 Pa
Friction angle	δ	26°
Newmark integration		
Parameter	γ	0.6
Parameter	β	0.3025

Table 2: Summary of all relevant parameters used in simulation.

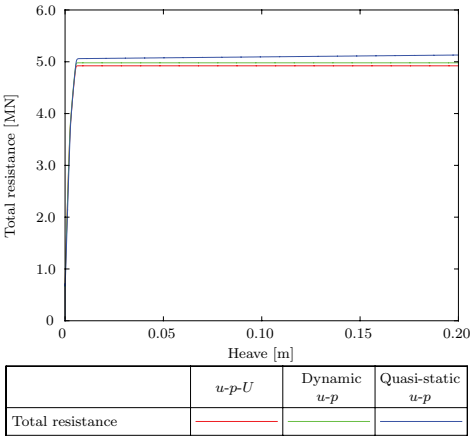

Figure 9: Total resistance for a pullout velocity of $v = 1 \cdot 10^{-6}$ $^{\mathrm{m}}/_{\mathrm{s}}$.

the outside of the skirt than on the inside. Thus, the first bend corresponds to the outside interface reaching its capacity and slips, which gives rise to a faster development of the inside friction. Once this interface also slips, a small rise in suction is observed and a perfectly plastic behavior takes place. It is further seen, that a negligible portion of the resistance stems from suction, indicating drained behavior. The inside friction is marginally larger than the outside friction, which can be attributed to this slight reduction in pore pressure inside the bucket.

The slipping of the interfaces at a relatively early stage indicates an unplugged failure c.f. Figure 2, which is further verified by a plot of the displacements given in Figure 11, which shows, that the displacements are concentrated in the bucket domain and water elements, denoting an expansion of the gap between bucket and seabed.

For a faster pullout velocity of $v = 1 \cdot 10^{-3}$ $^{\mathrm{m}}/_{\mathrm{s}}$, the total resistance is shown in Figure 12 for all three formulations. Again, it is seen, that there is generally

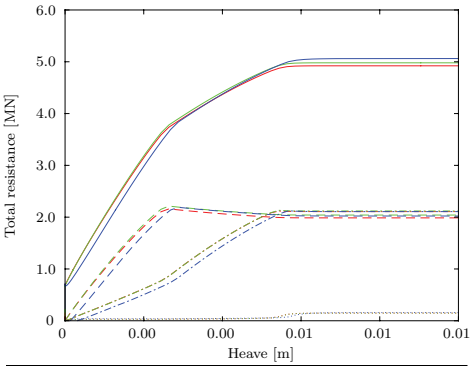

Figure 10: Initial part of Figure 9 showing the two bends in the curve as well as the different contributions to the resistance. Notice that the total resistance starts from a non-zero value due to the selfweight of the bucket as discussed in section 6.7.

good agreement between the models, suggesting that the dynamic terms do not affect the solution in any considerable way at this velocity. However, the general behavior of the bucket is entirely different than for the slow loading, as indicated by the change in appearance of the response and the major increase in pullout resistance, which has not reached a steady level even after 200 mm of vertical displacement.

A breakdown of the individual contributions to the resistance shows that a major part of the resistance originates from a reduction in pore pressure underneath the bucket lid as well as a significant amount of friction on the outside skirt. The outside friction reaches a peak, followed by a slight decrease after which a further increase is obtained, such that the outer friction greatly

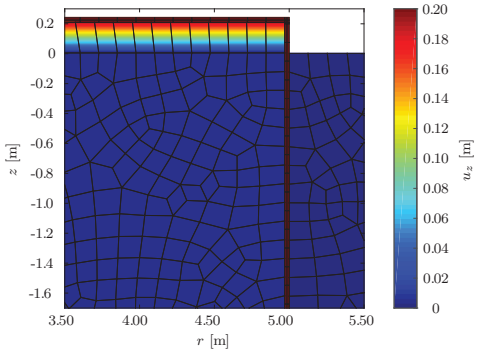

Figure 11: Excerpt of deformed mesh showing the vertical displacement u_z, for a pullout velocity of $v = 1 \cdot 10^{-6}$ m/s. The expansion of the water elements beneath the bucket lid(See Figure 5a) indicate a drained behavior with a development of a gap.

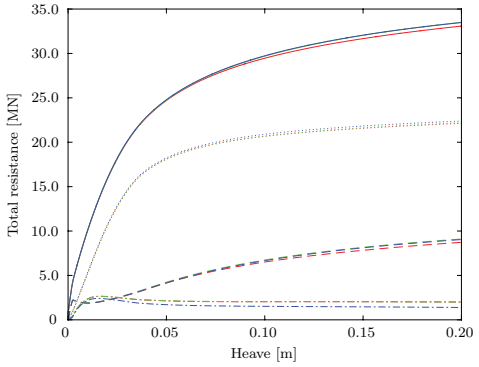

Figure 12: Total resistance and individual contributions for a pullout velocity of $v = 1 \cdot 10^{-3}$ m/s. Legend shown in Figure 10.

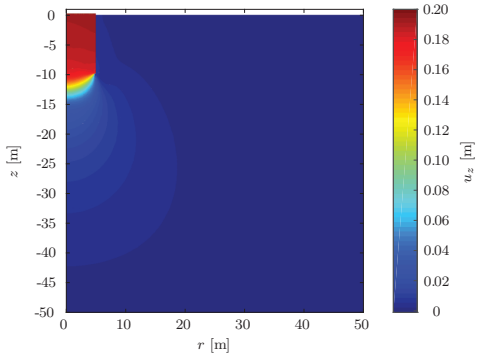

Figure 13: Vertical displacement, u_z, for a pullout velocity of $v = 1 \cdot 10^{-3}$ $^{\mathrm{m}}/_{\mathrm{s}}$. The behavior is seen to be plugged.

surpasses that of the drained scenario. This increase in shear capacity of the interface originates from the downwards directed seepage, which causes an increase in the compressive effective stresses on the outside of the bucket. On the inside of the bucket, a peak is also reached. However, the peak is followed by continuous decrease in friction, owing to the upwards directed seepage. Similar behavior is also reported in [18].

The vertical displacements of the solid phase at the end of the simulation are drawn in Figure 13, which shows, that the bucket exhibits a plugged behavior.

The fastest pullout velocity simulated is $v = 1$ $^{\mathrm{m}}/_{\mathrm{s}}$, and the development of the resistance is shown in Figure 14, which shows clear differences between the quasi-static and the dynamic formulations. The most noticeable different is the precipitous increase in resistance at the onset of loading predicted by both the *u-p-U* and *u-p* simulations. This peak can be attributed to the rapid acceleration of the bucket and appertaining acceleration of soil and fluid. Once the desired bucket velocity has been obtained, the acceleration stops. The consequence is a wave of negative pore pressure originating from the bucket lid

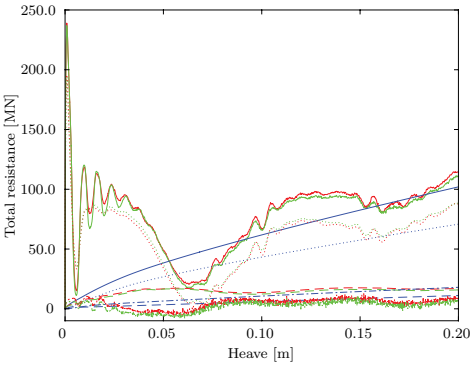

Figure 14: Total resistance and individual contributions for a pullout velocity of $v = 1$ $^{\mathrm{m}}/_{\mathrm{s}}$. Legend shown in Figure 10.

traveling downwards out of the bottom of the bucket and dispersed into the soil domain, causing a series of oscillations in the pore pressure due to reflection and refraction at the bucket skirt as well as the domain boundaries as can be seen in Figure 15. Naturally, such effects are not captured by the quasi-static *u-p* formulation, which shows a similar behavior as observed for the slower pullout velocities. Further, it is seen, that as the oscillations damps out, the dynamic models approach the quasi-static solution as expected.

It should be kept in mind, that cavitation is not accounted for in the models and that the suction reaches a level beyond 3 MPa, which according to (22) would require a water depth greater than 300 m to avoid cavitation, which is well beyond the intended installation depth of the suction bucket for use in jacket structures. Further, the applied velocity of 1 $^{\mathrm{m}}/_{\mathrm{s}}$ is extremely rapid and would not arise in reality. Nonetheless, the simulation shows, that even for such a high velocity, the difference between the *u-p-U* formulation and the much simpler *u-p* formulation is negligible.

A plot of the total resistance for all simulations is plotted in Figure 16, which

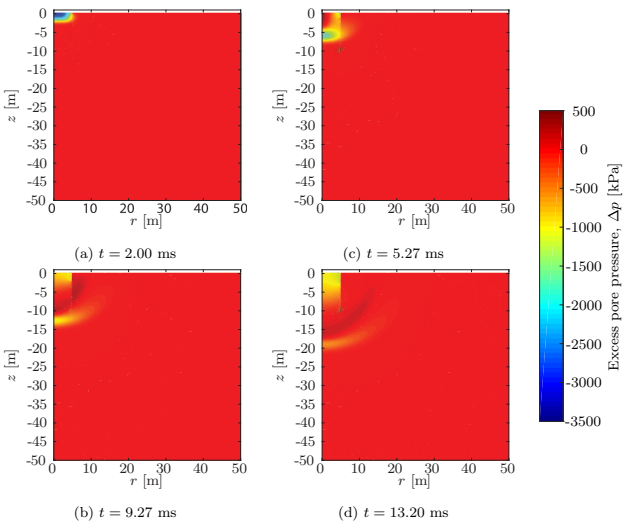

Figure 15: Excess pore pressure at four time stations as predicted by the *u-p-U* formulation.

generally shows the expected behavior of increasing resistance for increasing pullout velocity for all numerical implementations.

From this figure, it is evident, that the increase in resistance for the quasi-static model is most sensitive to the pullout velocity in the middle of the investigated range and indicates, that the resistance of the faster simulations approaches the upper limit of the completely undrained case. However, such statements can not be made for the dynamic models due to the effects of inertia, which becomes more and more pronounced for higher velocities.

8. Discussion of results

The use of a velocity driven model to simulate the loading of the bucket might be somewhat artificial for real world scenarios, where the actual loading is

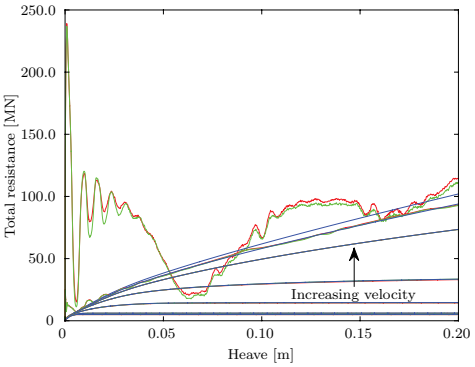

Figure 16: Total resistance for all velocities and formulations. Some curves not visible due to overlapping. Legend shown in Figure 9.

caused by time-varying external forces of cyclic or impact-like nature stemming from interaction with e.g. waves or ice floes with a certain momentum. Thus, the time dependent eventually-constant velocity applied to the suction bucket in the simulations is not directly applicable for a known external load. Owing to this, it would be reasonable to also investigate the tensile response under a known load scenario. However, this is outside the scope of this initial study.

9. Conclusion

In order to investigate the effects of inertia of solid and fluid phases on the dynamic tensile resistance of a suction bucket, the *u-p-U* and *u-p* coupled soil-fluid formulations has been implemented in a custom FEM code, which has been verified thoroughly. As basis for comparison, a full-scale suction bucket situated in Baskarp sand no. 15 has been simulated for a range of pullout velocities covering both drained and undrained behavior. The dynamic solutions have been held up against a quasi-static *u-p* solution using the commercial finite element program Abaqus.

Generally, it is found, that the response of all three formulations are in good agreement with each other, and that the inertial effects are negligible for most pullout velocities. For slow velocities close to drained behavior, the resistance stems from frictional resistance along the bucket skirt, while the resistance for fast pullout velocities is governed by the suction occurring underneath the bucket lid, which is only slightly influenced by inertia for most practical scenarios. Thus, the quasi-static formulation of Abaqus is found to be sufficient for the simulation of the tensile resistance of the investigated suction bucket during monotonic loading.

Appendix A. *u-p-U* components

The components of the *u-p-U* formulation are defined according to

$$\boldsymbol{M}_s = \int_\Omega (1-n)\,\rho_s \left(\boldsymbol{N}^u\right)^T \boldsymbol{N}^u d\Omega \tag{A.1}$$

$$\boldsymbol{M}_f = \int_\Omega n\rho_f \left(\boldsymbol{N}^U\right)^T \boldsymbol{N}^U d\Omega \tag{A.2}$$

$$\boldsymbol{C}_1 = \int_\Omega n^2 \left(\boldsymbol{N}^u\right)^T \boldsymbol{k}^{-1} \boldsymbol{N}^u d\Omega \tag{A.3}$$

$$\boldsymbol{C}_2 = \int_\Omega n^2 \left(\boldsymbol{N}^u\right)^T \boldsymbol{k}^{-1} \boldsymbol{N}^U d\Omega \tag{A.4}$$

$$\boldsymbol{C}_3 = \int_\Omega n^2 \left(\boldsymbol{N}^U\right)^T \boldsymbol{k}^{-1} \boldsymbol{N}^U d\Omega \tag{A.5}$$

$$\boldsymbol{G}_1 = \int_\Omega (\alpha - n)\, \boldsymbol{B}^T \boldsymbol{m} \boldsymbol{N}^p d\Omega \tag{A.6}$$

$$\boldsymbol{G}_2 = \int_\Omega n \left(\tilde{\boldsymbol{\nabla}} \boldsymbol{N}^U\right)^T \boldsymbol{m} \boldsymbol{N}^p d\Omega \tag{A.7}$$

$$\boldsymbol{P} = \int_\Omega \frac{1}{Q} \left(\boldsymbol{N}^p\right)^T \boldsymbol{N}^p d\Omega \tag{A.8}$$

$$\boldsymbol{B} = \tilde{\boldsymbol{\nabla}} \boldsymbol{N}^u \tag{A.9}$$

$$\bar{\boldsymbol{F}}_s = \int_\Omega (1-n)\,\rho_s \left(\boldsymbol{N}^u\right)^T \boldsymbol{b} d\Omega - \int_\Gamma (\alpha - n)\, p \left(\boldsymbol{N}^u\right)^T \boldsymbol{n} d\Gamma_p + \int_\Gamma \left(\boldsymbol{N}^u\right)^T \boldsymbol{t}'' d\Gamma_t \tag{A.10}$$

$$\bar{\boldsymbol{F}}_{p0} = -\boldsymbol{G}_1^T\, \bar{\boldsymbol{u}}\,(t_0) - \boldsymbol{P}\, \bar{\boldsymbol{p}}\,(t_0) - \boldsymbol{G}_2^T\, \bar{\boldsymbol{U}}\,(t_0) \tag{A.11}$$

$$\bar{\boldsymbol{F}}_f = \int_\Omega n\rho_f \left(\boldsymbol{N}^u\right)^T \boldsymbol{b} d\Omega - \int_\Gamma np \left(\boldsymbol{N}^u\right)^T \boldsymbol{n} d\Gamma_p \tag{A.12}$$

where Ω is the domain, Γ is the domain boundary, $\boldsymbol{n}$ is the boundary normal and $\boldsymbol{t}''$ is the effective traction on the domain boundary. $\boldsymbol{k}$ is a matrix accounting for anisotropic permeability, which can be replaced by a scalar k in the isotropic case. $\boldsymbol{m}$ and $\tilde{\boldsymbol{\nabla}}$ is defined by

$$\boldsymbol{m} = \begin{bmatrix} 1 & 1 & 1 & 0 & 0 & 0 \end{bmatrix} \tag{A.13}$$

$$\tilde{\boldsymbol{\nabla}}^T = \begin{bmatrix} \frac{\partial}{\partial x} & 0 & 0 & \frac{\partial}{\partial y} & \frac{\partial}{\partial z} & 0 \\ 0 & \frac{\partial}{\partial y} & 0 & \frac{\partial}{\partial x} & 0 & \frac{\partial}{\partial z} \\ 0 & 0 & \frac{\partial}{\partial z} & 0 & \frac{\partial}{\partial x} & \frac{\partial}{\partial y} \end{bmatrix} \tag{A.14}$$

Usually in the literature, $\bar{\boldsymbol{F}}_{p0} = \boldsymbol{0}$ is stated, however the definition above ensures that the integrated mass balance is fulfilled at the onset of the simulation where usually $\bar{\boldsymbol{u}}\,(t_0) = \bar{\boldsymbol{U}}\,(t_0) = \boldsymbol{0}$ while $\bar{\boldsymbol{p}}\,(t_0) \neq \boldsymbol{0}$. For further details of the *u-p-U* formulation, see [12, 17, 16, 21]

Appendix B. *u-p* components

The components of the *u-p* formulation are defined according to

$$\boldsymbol{M}_m = \int_\Omega \rho \left(\boldsymbol{N}^u\right)^T \boldsymbol{N}^u d\Omega \tag{B.1}$$

$$\boldsymbol{Q} = \int_\Omega \alpha \boldsymbol{N}^p \boldsymbol{m} \boldsymbol{B} d\Omega \tag{B.2}$$

$$\boldsymbol{S} = \int_\Omega \frac{1}{Q} \left(N^p\right)^T N^p d\Omega \tag{B.3}$$

$$\boldsymbol{H} = \int_\Omega \left(\boldsymbol{\nabla} \boldsymbol{N}^p\right)^T \boldsymbol{k} \boldsymbol{\nabla} \boldsymbol{N}^p d\Omega \tag{B.4}$$

$$\bar{\boldsymbol{F}}_m = \int_\Omega \rho \left(\boldsymbol{N}^u\right)^T \boldsymbol{b} d\Omega + \int_\Gamma \left(\boldsymbol{N}^u\right)^T \boldsymbol{t} d\Gamma \tag{B.5}$$

$$\bar{\boldsymbol{F}}_p = -\int_\Omega \left(\boldsymbol{N}^p\right)^T \boldsymbol{\nabla}^T \left(\boldsymbol{k} \rho_f \boldsymbol{b}\right) d\Omega + \int_\Gamma \left(\boldsymbol{N}^p\right)^T \boldsymbol{q} d\Gamma \tag{B.6}$$

where $\boldsymbol{t}$ is the total traction vector on the domain boundary and $\boldsymbol{q}$ is the flow across the domain boundary given as

$$\boldsymbol{q} = \int_{\Gamma} \boldsymbol{k} \left(-\boldsymbol{\nabla} \boldsymbol{N}^{p} + \rho_{f} \boldsymbol{n}^{T} \boldsymbol{b} \right) d\Gamma \tag{B.7}$$

and $\boldsymbol{\nabla}$ is the gradient operator given by

$$\boldsymbol{\nabla} = \begin{bmatrix} \frac{\partial}{\partial x} & \frac{\partial}{\partial y} & \frac{\partial}{\partial z} \end{bmatrix}^{T} \tag{B.8}$$

For further details of the u-p formulation, see [12, 13].

References

[1] M. G. Iskander, R. E. Olson, R. W. Pavlicek, Behavior of suction piles in sand, in: Design and performance of deep foundations: Piles and piers in soil and soft rock, Dallas, Texas, United States, 1993, pp. 157–171.

[2] T. Feld, Suction buckets, a new innovative foundation concept applied to offshore wind turbines, Ph.D. thesis, Geotechnical Engineering Group, Aalborg University (2001).

[3] G. T. Houlsby, R. B. Kelly, B. W. Byrne, The tensile capacity of suction caissons in sand under rapid loading, in: Proceedings of the International Symposium on Frontiers in Offshore Geotechnics (IS-FOG 2005), Perth, WA. Australia, 2005.

[4] R. B. Kelly, G. T. Houlsby, B. W. Byrne, Transient vertical loading of model suction caissons in a pressure chamber, Géotechnique 56 (10) (2006) 665–675.

[5] M. Senders, Suction caissons in sand as tripod foundations for offshore wind turbines, Ph.D. thesis, School of Civil and Resource Engineering, University of Western Australia (2008).

[6] E. Vaitkunaite, L. B. Ibsen, B. N. Nielsen, New medium-scale laboratory testing of a bucket foundation capacity in sand, in: Proceedings of the

Twenty-fourth (2014) International Ocean and Polar Engineering Conference, Vol. 2, Busan, South Korea, 2014, pp. 514–520.

[7] M. A. Biot, General theory of three-dimensional consolidation, Journal of Applied Physics 12 (2) (1941) 155–164.

[8] M. A. Biot, Theory of elasticity and consolidation for a porous anisotropic solid, Journal of Applied Physics 26 (2) (1955) 182–185.

[9] M. A. Biot, D. G. Willis, The elastic coefficients of the theory of consolidation, Journal of Applied Mechanics 24 (1957) 594–601.

[10] E. A. de Souza Neto, D. Perić, D. R. J. Owen, Computational Methods for Plasticity, Wiley, London, 2008.

[11] N. S. Ottosen, M. Ristinmaa, The Mechanics of Constitutive Modeling, Elsevier, London, 2005.

[12] O. C. Zienkiewicz, T. Shiomi, Dynamic behavior of saturated porous media; the generalized biot formulation and its numerical solution, International journal for numerical and analytical methods in geomechanics 8 (1984) 71–96.

[13] O. C. Zienkiewicz, A. H. C. Chan, M. Pastor, B. A. Schrefler, T. Shiomi, Computational geomechanics with special reference to earthquake egnineering, John Wiley & Sons, 1999.

[14] Dassault Systèmes Simulia Corp, Abaqus 6.14, http://www.3ds.com/products-services/simulia/products/abaqus/ (2014).

[15] Plaxis, PLAXIS 3D, www.plaxis.nl (2015).

[16] A. Gajo, A. Saetta, R. Vitaliani, Evaluation of three- and two-field finite element methods for the dynamic response of saturated soil, International journal for numerical methods in engineering 37 (1994) 1231–1247.

[17] B. Jeremić, Z. Cheng, M. Taiebat, Y. Dafalias, Numerical simulation of fully saturated porous materials, International journal for numerical and analytical methods in geomechanics 32 (2008) 1635–1660.

[18] K. Thieken, M. Achmus, C. Schröder, On the behavior of suction buckets in sand under tensile loads, Computers and Geotechnics 60 (2014) 88–100.

[19] M. Achmus, K. Thieken, Numerical simulation of the tensile resistance of suction buckets in sand, Journal of Ocean and Wind Energy 1 (4) (2014) 231–239.

[20] J. Cao, R. Phillips, R. Popescu, J. M. E. Audibert, Z. Al-Khafaji, Numerical analysis of the behavior of suction caissons in clay, in: Proceedings of The Twelfth (2002) International Offshore and Polar Engineering Conference, Kitakyushu, Japan, 2002.

[21] P. Tasiopoulou, M. Taiebat, N. Tafazzoli, B. Jeremić, Solution verification procedures for modeling and simulation of fully coupled porous media: static and dynamic behavior, Coupled systems mechanics 4 (1) (2015) 67–98.

[22] P. Wriggers, Computational Contact Mechanics, Springer, 2006.

[23] J. Clausen, Efficient non-linear finite element implementation of elasto-plasticity for geotechnical problems, Ph.D. thesis, Computational Mechanics, Esbjerg Institute of Technology, Aalborg University Esbjerg, http://vbn.aau.dk/files/14058639/JCthesis.pdf (2007).

[24] J. Clausen, L. Damkilde, L. Andersen, An efficient return algorithm for non-associated plasticity with linear yield criteria in principal stress space, Computers and Structures 85 (2007) 1795–1807.

[25] L. B. Ibsen, M. Hanson, T. Hjort, M. Thaarup, MC-parameter calibration of baskarp sand no. 15, Tech. rep., Department of Civil Engineering, Aalborg University, DCE Technical Reports; No 62 (2009).

[26] A. W. Skempton, Effective stress in soils, concrete and rocks, Pore Pressure and Suction in Soils (1961) 4–16.

[27] Å. Sjelmo, Soil - structure interaction in cohesionless soils due to monotonic loading, Master's thesis, Department of Civil Engineering, Aalborg University (2012).

SUMMARY

Geotechnical problems are often characterized by the non-linear behavior of soils and rock which are strongly linked to the inherent properties of the porous structure of the material as well as the presence and possible flow of any surrounding fluids. Dynamic problems involving such soil-fluid interaction can be treated numerically using a finite element formulation based on the theory of poro-elasto-plasticity.

However, due to the complex nature of the governing differential equations, commercial finite element codes often rely on a simplified formulation, which neglects the inertia of the fluid. In this thesis, a finite element code has been developed, which incorporates the full equation set. The code is used to evaluate the difference between the full and simplified formulations for the simulation of the dynamic tensile resistance of a suction bucket.

Further, the thesis deals with the development and implementation of constitutive models for use in the finite element method with particular focus on rock materials where the empirical Hoek-Brown material model is commonly used. In particular, the thesis deals with numerical implementations that is capable of simulating crucial aspects of the strength characteristics observed in rock materials such as strength softening and limited tensile strength.

ISSN (online): 2246-1248
ISBN (online): 978-87-7112-701-0

AALBORG **UNIVERSITY PRESS**